NEDO-24822
80NED049
Class I
June 1980

MARK II IMPROVED CHUGGING METHODOLOGY

Reviewed:
R. J. Muzzy, Manager
Mark II Containment Design

Reviewed:
H. E. Townsend, Manager
Containment Methods

Approved:
P. W. Ianni, Manager
Containment Design

Approved:
A. E. Rogers, Manager
Containment Technology

This document was prepared for the Mark II Utility Owners' Group by Bechtel Power Company under contract with the General Electric Company.

NUCLEAR POWER SYSTEMS DIVISION • GENERAL ELECTRIC COMPANY
SAN JOSE, CALIFORNIA 95125

GENERAL ELECTRIC

DISCLAIMER OF RESPONSIBILITY

The only undertakings of the General Electric Company respecting information in this document are contained in the contracts for Mark II Containment Consulting Services between the General Electric Company and each of the members of the U. S. Mark II Owner Group, effective variously June 9, 1975, June 13, 1975 and July 29, 1975, and nothing contained in this document shall be construed as changing the contracts. The use of this information by anyone other than the members of the U.S. Mark II Owners Group either themselves or through technical consultants, or for any purpose other than that for which it is intended under the contracts, is not authorized; and with respect to any unauthorized use, the General Electric Company makes no representation or warranty, express or implied, and assumes no liability of any kind as to the completeness, accuracy, usefulness or non-infringing nature of the information contained in this document.

CONTENTS

FIGURES

TABLES

SUMMARY

This report was prepared to document work done on Task A.16 Phase II of the Mark II Owners Group Long-Term Program. The purpose of Task A.16 is to provide an improved chugging load definition methodology and to answer NRC concerns about fluid-structure interaction which were raised in NUREG-0487.

This report demonstrates that chugging is an acoustic phenomenon. Pressures on the boundary of the suppression pool may be calculated by applying an appropriate source at the downcomer exit and propagating its effects to the rigid or flexible boundary of the suppression pool using an acoustical transfer function.

The effects of fluid-structure interaction are seen to be (1) a reduction in the effective sonic velocity of the tank/water system and (2) damping of the pressure signals felt on the tank boundary. The sonic velocities in the vent and in the tank/water system control the frequency content of the chugging pressures and damping controls the duration of the chugging signal.

The amplitude of the chugging pressure is controlled by the collapsing steam bubble source at the vent exit. The design source was generated from 4T experimental data. A conservative chugging data base was chosen from the 4T tests and the design source was developed to represent the data base in an appropriately conservative manner.

The accuracy and utility of the improved chugging methodology is confirmed by comparing predicted results with 4T experimental data and with results calculated by the NASTRAN computer program. Using this methodology, sample calculations made for a typical Mark II containment confirm that calculated responses are below those generated using the lead plant bounding loads specification.

Note that the acoustical chugging methodology and the procedure used to define the design chugging source from experimental data are independent of the actual data base considered. Although the methods could be applied equally well to any available detailed data base, the 4T data base was used. It is anticipated that the current design chugging source will be compared with other recently available data. If necessary, the design chugging source may be modified to maintain an appropriate degree of conservatism when considering all applicable data.

1. INTRODUCTION

In October 1975, a series of pressure suppression tests was performed by General Electric in its 4T facility to investigate pool dynamic phenomena (poolswell) in the Mark II containment[1] (Figs. 1-1 and 1-2). During these Phase I tests, a pulsating condensation phenomenon termed "chugging" was observed. Further investigation of chugging in 4T was made in the Phase II and III tests.

1.1 The Chugging Phenomenon

Chugging, or unsteady condensation, is a design consideration in all pressure suppression containment systems, using either vertical or horizontal vents, and has been observed in many experiments. The mechanism behind chugging involves the collapse of the vapor-liquid interface at the vent exit. Two mechanisms involved are excessive steam condensation rate and surface instabilities at the vapor-liquid interface. The excessive condensation occurs because the supply from the vent system is exceeded by the available surface area for condensation, causing the interface surface to contract. The surface instabilities are probably bubble-size dependent and tend to cause an increase in interface surface area.

The steam condensation pressure oscillation begins in the vent pipe before it occurs in the drywell and the magnitude of the oscillation is greater there. The sharp underpressures measured at the vent exit are due to the collapse of the vapor-liquid interface and condensation of the vapor in the vent pipe. This underpressure causes the pool water to enter the vent pipe. Once the water enters the vent pipe, only the cross-sectional area of the vent is available for condensation and, as the water in the vent heats, its condensation rate drops. When the steam flow into the drywell exceeds the condensation rate, the pressure in the drywell and vent system increases and a new vent clearing transient starts.

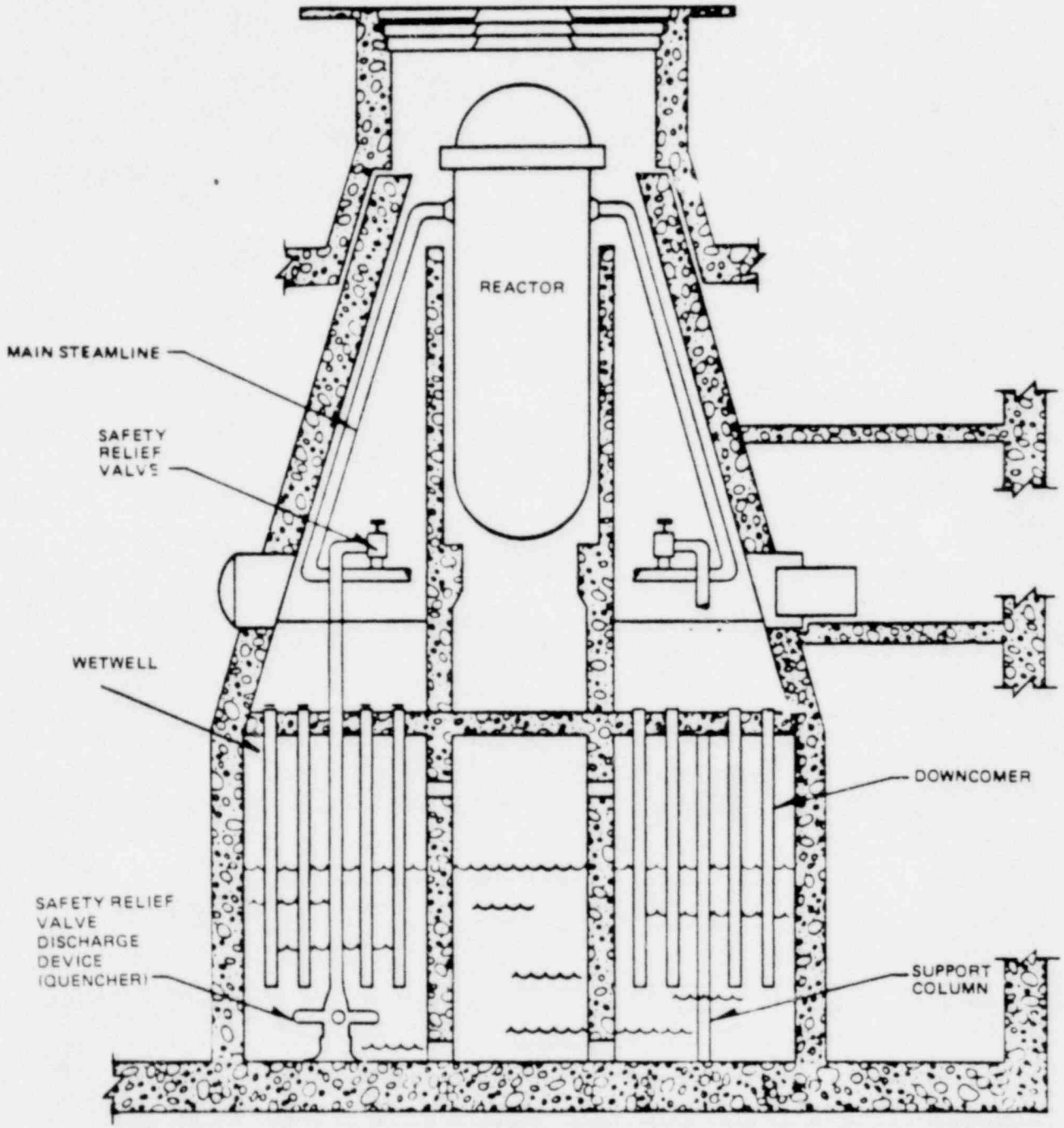

Figure 1-1. Mark II Pressure Suppression Containment

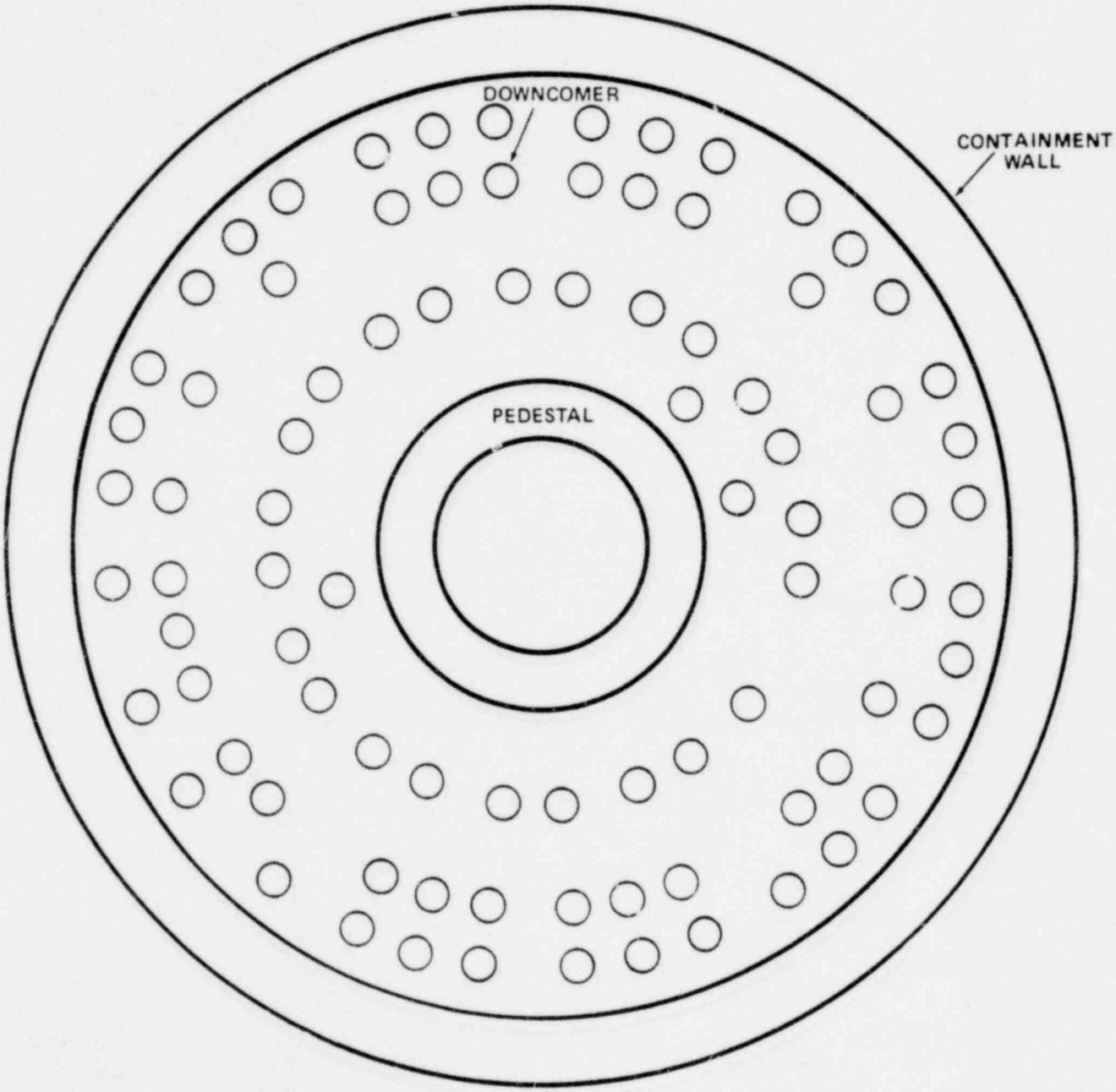

Figure 1-2. Typical Mark II Wetwell

The vent flow rate follows from the previous chronology of a chug. As the vapor bubble collapses and the low pressure in the vent is generated, a large pressure difference exists across the vent system, causing a large increase in the flow rate. The large flow from the drywell to the pool in turn causes the drywell pressure to drop, lowering the pressure difference across the vent system and thus decreasing the flow rate. At the same time, the pool water has surged back into the vent system, lowering the condensation rate and thus raising the pressure there. The vent system pressure difference and hence the vent flow rate thus drop to near zero before the vent is recleared and another chugging cycle begins.

Once chugging has been initiated, individual chugs occur in a more or less periodic manner. Chug starts do not have a single frequency, however, but vary from run to run and even within a single blowdown.

1.2 The Mark II Chugging Load Definition

In February 1977, an Application Memorandum[2] was issued by General Electric specifying the symmetric chugging load at the containment boundary to be +37.9/-34.5 kPa (+5.5/-5.0 psi) at a 95% confidence level (mean values: +33.1/-27.6 kPa; +4.8/-4.0 psid) with a frequency range of 20 to 30 Hz. The asymmetric load was specified to be +137.9/-96.5 kPa (+20/-14 psid) with a frequency range of 20 to 30 Hz. These loads were believed to be very conservative and, in 1977, General Electric issued a bounding loads report[3] justifying the conservatism of these loads. A key argument for the conservatism of the Application Memorandum was based on the results of the Multivent Hydrodynamical Model[4] which exploits the random nature of chugging. An additional argument was that the Application Memorandum utilized 4T chugging responses which contained additional 4T-unique frequencies and fluid-structure interaction.

To obtain an understanding of the structural characteristics of 4T, a fluid-structure interaction study[5] was undertaken. The study concluded that the chug source is impulsive and the 4T response to the impulsive source is a sinusoidal-like "ringout" whose frequency is system related.

The Nuclear Regulatory Commission issued comments[6] dated August 10, 1977, which questioned the adequacy of the Application Memorandum, in essence, because the frequency range over which the load was to be applied is 4T- and not Mark II-unique and the pressure amplitudes would likely be larger for a more rigid Mark II containment.

A.16 of the Mark II program was initiated to develop an improved chugging load definition which would provide for more realistic loads and resolve fluid-structure interaction concerns. The results of Phase II of Task A.16 yielded an approach to chugging consisting of the following key elements:

(1) Investigation of the 4T chugging data to develop an understanding of the data base and clues to the nature of the chug source (Chapter 2).

(2) A numerical simulation of the response of a tank-water-vent system to a pressure impulse which represents the chug source. From such a simulation and the governing equations of motion, we learn the 4T system response is essentially acoustic in nature (Chapter 3).

(3) Development of an acoustic three-dimensional analytical model for the 4T and Mark II geometries using the assumptions verified by the numerical simulation and analysis (Chapter 4).

(4) Treatment of fluid-structure interaction (FSI) effects by (a) application of a rigid wall pressure to a NASTRAN flexible wall model and (b) solution of the acoustic wave equation with flexible wall boundaries; verification of this method of FSI in 4T with a NASTRAN model (Chapter 5).

(5) Verification of the adequacy of the acoustic model by comparison with several types of 4T chugging data (Chapter 6).

(6) Creation of a procedure to develop a design source from an experimental data base and the use of the 4T data to determine a design source (Chapter 7).

(7) Application of the chugging methodology and the design source to a Mark II multivent geometry to develop structural responses using an ANSYS structural model (Chapter 8).

2. UNDERSTANDING THE 4T CHUGGING DATA

Prior to this study, the entire pressure history from the bottom-center sensor and the combined acceleration history from the vent-exit accelerometers for each 4T blowdown were scanned to identify chugs. The bottom-center sensor recorded the highest pressure amplitudes and the vent exit accelerometers were responsive to the impulsive chug events. A pressure excursion greater than 27.6 kPa or less than -27.6 kPa (± 4 psi) or a vent tip acceleration greater than 2g or less than -2g, following trend removal, was regarded as signifying a chug start. A 3/4-second interval was required before such a departure was accepted as another chug. Approximately 600 chugs were identified in this way from the 27 usable runs, which spanned all anticipated operating conditions.

Chug peak overpressure (POP) values were studied to identify any systematic effects of such parameters as time into test, vent-pipe diameter, initial pool temperature, submergence, and liquid versus steam break. No trend of POP with time into test was noted. Cumulative histograms of POP for each combination of pipe diameter and initial pool temperature, however, indicated that two test conditions yielded higher pressures at the upper probability points than the other conditions and there was a corresponding slight increase in mean POP for those two conditions (see Appendix A). It was not possible from physical considerations to identify a cause of the higher pressures. Accordingly, the view was taken that there may be some conditions in which high POP values could occur in the higher proportions noted, and the chugs in the data base were restricted to conditions giving the unfavorable distributions. This provided 137 chugs from nine runs for the two conditions of 610 mm (24 inch) pipe, 21°C (70°F) initial pool temperature (Phase I tests, runs 27 to 31 and 34), and 508 mm (20 inch) pipe, 66°C (151°F) initial pool temperature (Phase III tests, runs 42, 44, and 46); these were steam breaks, with 63.5 mm (2.5 inch) and 76.2 mm (3.0 inch) venturi data taken together as indistinguishable. A moderate effect due to submergence was averaged to 3.35 m (11 feet) to be used in modeling

the 4T. In each chug, the POP was placed midway in a 0.768-second signal, which was found to consistently encompass the high-signal strength portion of each chug. Accordingly, a data base of 137 chug signals from the bottom-center of the 4T each 0.768 seconds in duration with the POP at the midpoint, was used in this study.

A spectral analysis was performed on each chug in the data base to reveal patterns of power by frequency. Other runs, including liquid breaks, have also been analyzed spectrally, although on a continuous rather than chug by chug basis (see Appendix A). The consistency of the frequency patterns in both studies indicates that the 137-chug data base is fully representative of frequencies which occur in any 4T run.

2.1 Classification of the 4T Chugs

Even a casual perusal of the 4T chug library shows that not all chugging events are created equal. Thus, a careful review of the 4T chug library has been made with the intent of classifying the various types of chugging events. The review of the 4T chug library was performed by comparing:

(1) Plots of the pressure time-history,

(2) Plots of the power spectral density (PSD), and

(3) Tables of the PSD (amplitude vs frequency)

for the 137 chugs. The chug library was classified into four categories with the following characteristics:

Category I Chugs Classical

Shape: damped sinusoidal
Predominant Frequencies: 5, 13, 21 and 18 to 31 Hz
Peak Pressure Amplitude: 34 to 138 kPa positive (5 to 20 psi)
28 to 96 kPa negative (-4 to -14 psi)

Category II Chugs Sinusoidal

Shape: sinusoidal
Predominant Frequencies: 5, 13, 21, 29 Hz
Peak Pressure Amplitude: 34 kPa positive and 34 kPa negative (±5 psi)

Category III Chugs Mixed Sinusoidal and Classical

Shape: damped and undamped sinusoidal
Predominant Frequencies: 5, 13, 21 and 18 to 31 Hz
Peak Pressure Amplitude: 103 kPa positive and 103 kPa negative (±15 psi)

Category IV Chugs Other Events

Shape: irregular
Predominant Frequencies: mixture of 5, 13, 21, 30, 35 to 40, 45 to 50 Hz
Peak Pressure Amplitude: <34 kPa (<5 psi) or very low amplitude

Figs. 2-1 through 2-4 show four examples each of the four chugging categories from the 4T chug library. Note here that the sinusoidal event is called a Category II type of chug. It is important to note that although the sinusoidal events and chugging are related by the fact that they are steam condensation phenomena, their characteristic frequency and amplitude are markedly different.

The relative fractions of occurrence of the various types of chugging categories have been calculated and the results are shown in Table 2-1. A list of chug numbers, their categories, and the 4T run numbers from which they came is shown in Table 2-2.

The following Figures are GENERAL ELECTRIC COMPANY PROPRIETARY and have been removed from this document in their entirety.

2-1 Examples of Category I Chug

2-2 Examples of Category II Chugs

2-3 Examples of Category III Chugs

2-4 Examples of Categroy IV Chugs

Table 2-1

CATEGORIES OF 4T CHUGGING DATA

Category	A Number of Events	B Fraction of Total Events	C Predominant Frequencies	D Normalization Constant (kPa^2/psi^2)	E Fraction of Total Power	F Power/Event (kPa^2/psi^2)
I. Classical						
II. Sinusoidal						
III. Mixed						
IV Other						
TOTAL						

*This bar indicates information that is considered proprietary to the General Electric Company

Table 2-2

CLASSIFICATION OF 4T CHUGS

Chug No.	Category	4T Run No.	Chug No.	Category	4T Run No.
1	II		36	II	
2	III		37	III	
3	I		38	III	
4	IV		39	II	
5	II	27	40	III	
6	II		41	II	29
7	I		42	III	
8	III		43	III	
9	II		44	II	
10	II		45	III	
11	II		46	IV	
12	II		47	II	
13	II		48	II	
14	I		49	II	
15	II		50	II	
16	II		51	I	30
17	I		52	I	
18	II		53	III	
19	II		54	III	
20	II		55	IV	
21	III		56	II	
22	I		57	II	
23	II	28	58	II	
24	III		59	II	
25	I		60	II	
26	IV		61	II	
27	III		62	II	
28	I		63	I	31
29	II		64	II	
30	I		65	IV	
31	I		66	II	
32	II		67	III	
33	II		68	IV	
34	IV		69	II	
35	II		70	II	
			71	I	

Table 2-2

CLASSIFICATION OF 4T CHUGS (Cont'd)

Chug No.	Category	4T Run No.	Chug No.	Category	4T Run No.
72	III		105	III	
73	II		106	II	
74	II		107	IV	
75	III		108	II	
76	III	34	109	II	
77	II		110	III	
78	IV		111	IV	44
79	II		112	IV	
80	II		113	IV	
81	II		114	IV	
82	III		115	IV	
83	II		116	IV	
84	II		117	IV	
85	II		118	II	
86	II		119	II	
87	II	42	120	II	
88	II		121	II	
89	II		122	III	
90	I		123	IV	
91	III		124	II	
92	IV		125	II	
93	IV		126	III	
94	II		127	II	46
95	II		128	IV	
96	II		129	IV	
97	III		130	II	
98	III		131	IV	
99	II		132	II	
100	II	44	133	IV	
101	II		134	II	
102	II		135	IV	
103	II		136	IV	
104	IV		137	IV	

2.2 Principal Frequencies for the Chug Categories

Each chug from the 4T library of 137 chugs was placed into a category according to its shape and frequency characteristics. In order to find the dominant frequency characteristics, we can average the PSDs for each category. This averaging will tend to accentuate those frequencies which occur most often. Figs. 2-5 through 2-8 show normalized PSDs for chug Categories I through IV. The normalization procedure is explained in the following paragraphs. Column C of Table 2-1 shows the principal frequencies in each chug category. The patterns of these frequencies and their origin will be discussed in the next section.

Column D of Table 2-1 shows the sum of the normalization constants (the total area under all the unnormalized PSDs) for each category. When the sum of unnormalized PSD values is divided by this normalization constant, the area under the resultant PSD is unity and we call the PSD "normalized." Thus, the normalization constant for each category represents the total power (energy density) contained in the chugs of that category.

Notice that the Category II chugs contain a majority of the total chugging power (Column E, Table 2-1). One of the reasons for this is that they are at least twice as numerous as any other category of events. On a "per event" basis (Column F, Table 2-1), it is clear that the Category I chugs contain more power per event than Category III chugs and roughly twice as much power per event as the Category II chugs.

Fig. 2-9 shows the normalized PSD for all 137 chugs (all categories combined). Fig. 2-10 shows a composite normalized PSD for all 137 chugs (solid line) and contributions to the total PSD from the four chug categories (dashed lines). The PSD of each category has been multiplied by the ratio of the total power of that category to the total power of all categories. Notice that:

The following Figures are GENERAL ELECTRIC COMPANY PROPRIETARY and have been removed from this document in their entirety.

2-5 Normalized PSD for Category I Chugs

2-6 Normalized PSD for Category II Chugs

2-7 Normalized PSD for Category III Chugs

2-8 Normalized PSD for Category IV Chugs

2-9 Normalized PSD for 137 Chugs in the Chug Library

2-10 Composite Normalized PSD for Category I, II, III, and IV Chugs

(1) All categories contribute to the frequency peaks at 5, 13, and 21 Hz;

(2) The Category IV events make a negligible contribution to the total power.

2.3 Analysis of Frequency Patterns in the 4T Chugging Data

In order to develop an analytical model of the chugging phenomenon, it is necessary to understand the causes of the dominant frequencies seen in the 4T data. Once the patterns in the 4T data are well understood, the application to the Mark II geometry can be accomplished.

It is reasonable to believe that the dominant frequencies seen in the 4T data result from excitation of various acoustic modes of oscillation in the tank and in the vent of the 4T facility. Consequently, we will look for frequency patterns in the 4T data which result from the vent pipe and pool natural frequencies and their harmonics.

We picture the vent as a one-dimensional pipe closed at one end by water and open to the drywell at the other end. For this geometry, the natural acoustic frequencies are

$$f_n = \frac{(2n + 1)c}{4L} \quad , n = 0, 1, 2, 3, \ldots \tag{2.1}$$

Using the speed of sound in pure steam*, c = 488.6 m/s (1603 fps), and the length L_v of the 4T vent of 28.65 m (94 ft), we can calculate the vent fundamental frequency f_o to be

$$f_o = \frac{c}{4L_v} = 4.26 \text{ Hz} . \tag{2.2}$$

The higher odd harmonics are shown in Table 2-3 where they are compared with the observed frequencies from the Category II chugs. Noting the similarity between the predicted and observed frequencies leads to the conclusion that the 4T vent plays an important role in

*Assuming saturated steam at 275.79 kPa (40 psi).

determining the frequency of the wall pressure traces for the sinusoidal events. Since the frequencies 5, 13, and 21 Hz appear in the data for all chug categories, it appears that the vent pipe frequencies defined by Eq. (2.1) are important components of the wall pressure loads.

Table 2-3

VENT PIPE FREQUENCIES IN 4T

n
0
1
2
3
4
5
6
7
8
9
10
11

We can perform a similar type of analysis for the pool to explain the additional dominant frequencies seen in Category I and III chugs. The pool can be pictured as a vessel filled with water and open at one end. For this geometry, the frequencies of oscillation are again

$$f_n = \frac{(2n + 1)c}{4L_p} \quad , n = 0, 1, 2, 3, \ldots \tag{2.3}$$

where c is the acoustic velocity in the 4T suppression pool and L_p is the depth of the pool. Adjustments must be made to the sonic velocity in the 4T pool to account for flexibility of the tank wall and base plate and the presence of small amounts of air in the water. These adjustments will have a substantial effect on c, which will be demonstrated below. Adjustment of sonic velocity due to flexibility of the 4T tank wall and base plate can be made according to the formula (see Appendix B)

$$c' = c/\sqrt{1 + \rho c^2 \delta} \quad , \tag{2.4}$$

where c is the sonic speed in pure water* and δ is the distensibility of 4T.

In Appendix B, this formula is shown to yield an effective value of $c' = 878$ m/s (2834 fps). Thus, the expected ringout frequency (fundamental) in the air-free 4T pool is given by

$$f_o = \frac{c'}{4L_p} = 30.8 \text{ Hz} \tag{2.5}$$

where $L_p = 7.01$m (23 ft).

The difference between this value and the observed average ringout frequency in the 4T pool (21.7 Hz) is believed to be the result of air entrained in the water. It is shown in Appendix B that an air content of 0.04% by volume would account for this difference. The amount of air was not measured during the 4T tests, but a value of 0.04% is regarded as reasonable. The fact that ringout frequency tends to increase with time into test further supports the hypothesis that the sonic velocity is being reduced by air in the water.

*Taken to be 1524 m/s (5000 fps) for the average pool temperature and pressure in the 4T data base tests.

The average amount of sonic velocity reduction due to air derived from the 4T tests is 29.5%. This compares well with the value of 31% as determined from independent tests in the Pressure Suppression Test Facility (PSTF)[7]. Using these values in the 4T yields a frequency which agrees well with the frequency in the 4T chugging tests.

Thus, we conclude that:

(1) The predominant Category II chug frequencies are the vent fundamental acoustic frequency and its harmonics.

(2) The predominant Category I (classical chug) frequency is the pool fundamental acoustic frequency based on c/4L (where L is the pool depth) with c reduced from its pure water, rigid tank value by tank flexibility and entrained air.

3. GOVERNING EQUATIONS FOR CHUGGING

In Chapter 2 it was shown that the 4T data can be described in terms of vent and pool acoustics. We now proceed to support this assertion with a more detailed theoretical understanding of the 4T system response to chugging. This theoretical understanding in the form of a mathematical model will help us to specify the chugging load, i.e., the forces due to chugging, on the suppression pool boundary of any Mark II containment.

Chugging is viewed as a three-part phenomenon composed of a source, a transfer function, and a fluid-structure interaction. The chug source is the result of an acceleration of the steam-water interface at or in the vicinity of a vent exit. This acceleration of the interface is due to the pulsating condensation and is either impulsive resulting in a Category I type chug, periodic which results in a Category II chug, or both resulting in a Category III chug. The effects of the chug source are propagated to the pool boundary. This propagation is described by what we term a transfer function which results from the equations of motion for the fluid. Finally, we come to the interaction between the fluid and the containment structure. In our description of chugging, the transfer function which represents the propagation of the effects of the source to a rigid containment can be separated from the fluid-structure interaction which describes the response of a flexible containment to the rigid containment pressure. Our treatment of the fluid-structure interaction, including the proof that such a separation of the fluid and structural motions is possible, is treated in Chapter 5. Here we will deal with the chug source and the transfer function.

3.1 Semiempirical Chug Source

The pressure excursions called chugging observed in the 4T are the result of intermittent steam condensation occurring at the vent exit[1,3,7,8,9]. This condensation is controlled principally by the vent steam mass flux, the air content in that flux, and the

temperature difference across the steam-water interface. When conditions at the vent exit are such that stable condensation is no longer possible, the sequence of chugging as shown in Fig. 3-1 begins:

(1) The water in the vent is isolated which allows a layer of saturated water to form at the interface reducing the rate of condensation.

(2) The reduced condensation rate allows the drywell pressure to increase; the interface is thus pushed out of the vent back into the pool. The layer of saturated water protects the interface while it is inside the vent.

(3) As the steam-water interface emerges into the pool, local turbulence destroys the protective boundary layer of saturated water and the interface comes in contact with the colder pool. A "burst" of condensation follows.

(4) The steam flow through the vent is not sufficient to supply the rapid condensation. The drywell is depressurized and water again reenters the vent to repeat the cycle.

Thus, a condensation event is responsible for initiating the chug and is the chug source. This source is dependent on several factors, some of which are highly random. As a result, the nature of the source is also random. For example, if local conditions permit the steam-water interface to extend sufficiently far into the pool, the resulting condensation event can impulsively excite the pool acoustic vibrational modes. Or the chug source may include multiple condensation events which will not always excite the pool acoustics. These multiple condensation events appear to be driven by the acoustic vibrational modes of the vent.

To be able to develop a completely analytical description of chugging, it is obvious that we need an analytic model of the condensation and interface collapse. A model of steam bubble collapse is given by

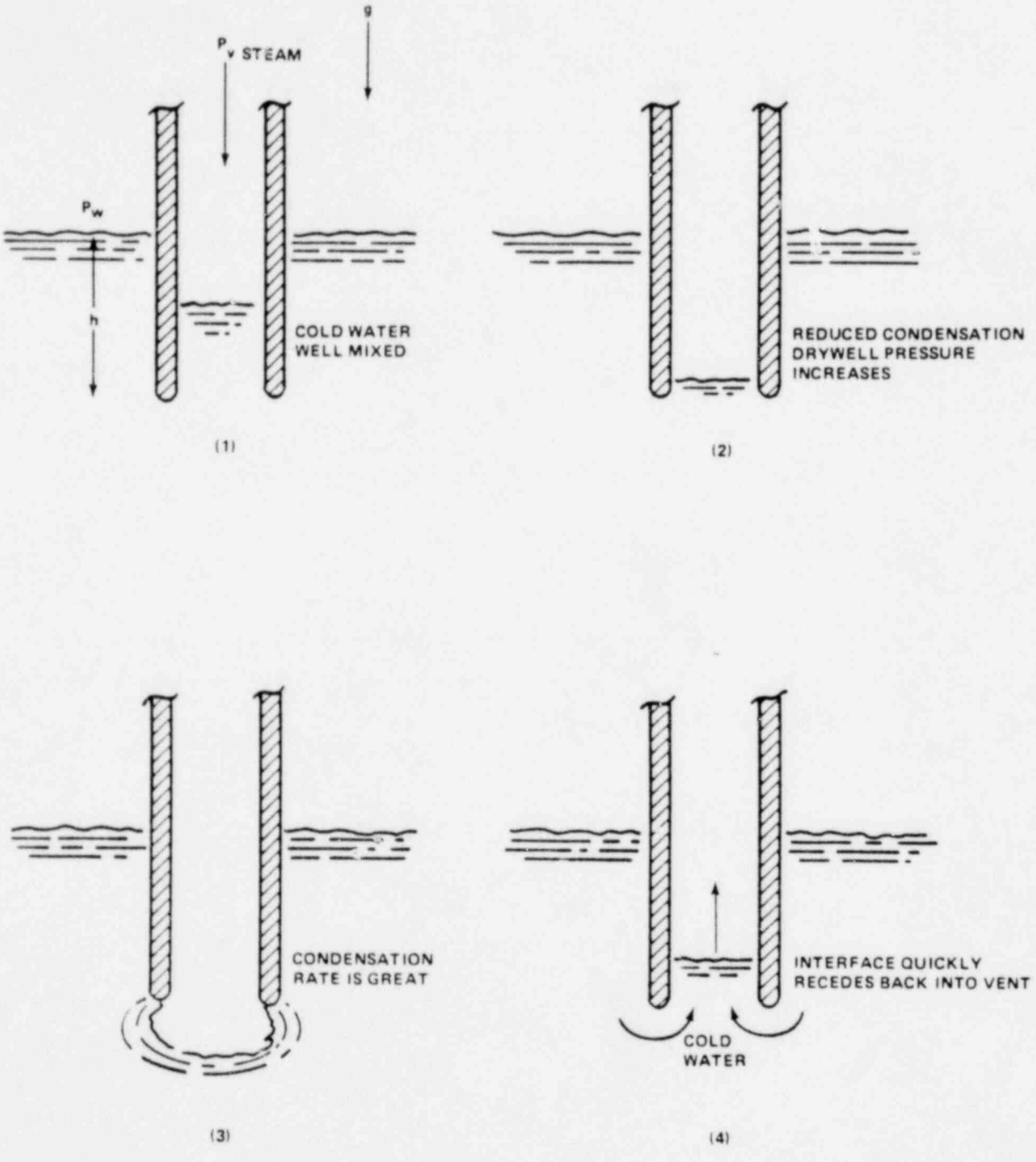

Figure 3-1 The Observed Sequence of Events During Chugging

Florscheutz and Chao[10]. This model treats the mechanics of the collapse under spherically symmetrical conditions to ascertain the relative importance of the dominant mechanisms controlling the collapse: liquid inertia and heat transfer. Florscheutz and Chao conclude that when the collapse is inertia controlled, collapse rates are high and increase as the collapse proceeds. In contrast, when the collapse is heat-transfer controlled, the collapse rates are low and decrease as the collapse proceeds. An integral component of the Florscheutz and Chao model is the use of a calculational result obtained by Plesset and Zwick[11]. In their article on bubble dynamics and cavitation, Plesset and Prosperetti[12] express doubts as to the applicability of this result to collapsing steam bubbles. In their opinion, no entirely satisfactory theoretical results are available for the modeling of steam bubble collapse under conditions in which thermal effects play a significant role.

Because of this disagreement between notable workers in this field and also because the conditions at the vent exit which effect the chug source are random, we will not rely entirely on any theoretical model for an analytical description of the chug source. Instead, we will develop a semiempirical chug source. Wherever possible, the 4T data will be used to develop the source. Where the data cannot be used, theory will be employed. Since it is necessary to have a transfer function in order to relate wall pressure data to source behavior, we will only be able to describe the source in terms of unknown constants in this chapter. Following the derivation of the transfer function, these constants will be evaluated.

From the examination of the 4T data in Chapter 2, we saw that there are essentially two kinds of chugs: Category I and Category II. A Category III chug can be treated as a Category II chug terminated by a Category I chug. Thus, two different chug sources are necessary.

An analysis of the Category I chugs in Chapter 2 reveals the pressure response to be that of the acoustic ringout of the 4T tank-water system. This type of response would be generated by an inertia

controlled steam-bubble collapse. To simulate a chug, Anamet Laboratories, during an experimental study of the 4T fluid-structure interaction[5], imploded an evacuated bell jar placed at the 4T vent exit. The pressure time-history at the tank bottom-center during one of those tests is shown in Fig. 3-2. The similarity between the pressure response of the simulated chug and actual Category I chugs is apparent.

Since the collapse of the void created by crushing the bell jar is inertia controlled, we can roughly estimate the general shape or time dependence of a Category I source from Rayleigh's treatment of bubble collapse[13]. This yields an acoustic source whose strength may be written[14]

$$S(t) = \frac{4}{3}\pi \frac{p_o}{\rho} \left[\frac{R_o^3}{R(t)^2} - 4R(t)\right]. \tag{3.1}$$

Here $R(t)$ is the radius of the cavity at time t, R_o is its initial value, and p_o is the static fluid pressure. Note that at extremely small values of $R(t)/R_o$, for which this expression for the source tends to $+\infty$, the classical Rayleigh solution is not applicable because it neglects the opposing internal pressure due to compression of the vapor inevitably present and the presence of the vent into which the void collapses. Guided by Eq. (3.1), we will approximate the impulse delivered to the pool by an inertia controlled bubble collapse by a single impulse. We defer until Chapter 6 the demonstration that this approximation will generate a pressure response similar to that shown in Fig. 3-2. The inertia controlled collapse also excites an acoustic vent response which serves as a source of long-term acoustic energy for the pool. Therefore, we could approximate the total 4T Category I source empirically by

$$S_I(t) = -A_o \Lambda\left(\frac{2t}{\tau} - 1\right) + \sum_{n=1}^{N} A_n e^{-\alpha\omega_n t} \sin \omega_n t, \tag{3.2}$$

Figure 3-2 4T Bell Jar Test

(GENERAL ELECTRIC COMPANY PROPRIETARY)

where

$$\Lambda(\ldots) \equiv \begin{cases} 1 - |x| & |x| < 1 \\ 0 & |x| > 1 \end{cases} . \tag{3.3}$$

The impulse amplitude A_o and duration τ as well as the amplitudes A_n, damping constant α, and frequencies ω_n of the vent response will be determined empirically from the 4T data in Chapter 6.

An examination of the Category II chugs shows that the pool is not responding in its transient acoustic modes but rather at the acoustic frequencies of the vent. Each Category II chug has a time duration that is consistent with the opinion that a Category II chug is a succession of condensation events the frequency of which function is being driven in a steady state fashion, it is transparent to the Category II source. Thus, the general time dependence of the source is given by the Category II chugs themselves, and we therefore could approximate the Category II source empirically by

$$S_{II}(t) = u(T-t) \sum_{n=0}^{N} B_n \sin(\omega_n t), \tag{3.4}$$

where $u(x)$ is the Heaviside step function.

3.2 Fluid Equations of Motion

The state of a fluid is completely determined once we specify the fluid velocity $\vec{u}$ and any two of the thermodynamic properties pertaining to the fluid as functions of space and time. Hence, the motions of a fluid medium are governed by four equations. The first equation is a continuity equation expressing the conservation of mass

$$\frac{\partial \rho}{\partial t} + \vec{\nabla} \cdot (\rho \vec{u}) = 0 . \tag{3.5}$$

The second equation is a force equation expressing the conservation of momentum

$$\rho \frac{\partial \vec{u}}{\partial t} = - \rho (\vec{u} \cdot \nabla) \vec{u} - \nabla [P + \rho\Phi - (\eta + \frac{4}{3} \mu) \nabla \cdot \vec{u}] - \mu \nabla \times \nabla \times \vec{u}, \qquad (3.6)$$

where μ and η are the coefficients of shear and bulk viscosity and Φ is a potential energy caused by a force per unit mass. The third equation is a heat exchange equation expressing the conservation of energy

$$\rho T \frac{\partial s}{\partial t} = - \rho T \vec{u} \cdot \nabla s + \nabla \cdot (\kappa \nabla T) + \vec{\tau} : \nabla \vec{u}, \qquad (3.7)$$

where $\vec{\tau}$ is the viscous-stress tensor, κ the thermal conductivity, and s the specific entropy. The last equation can be one of several equations expressing the constitutive relations that characterize the fluid and its response to thermal or mechanical stress

$$\begin{aligned} P &= P(\rho, s) \\ T &= T(\rho, s) \quad . \end{aligned} \qquad (3.8)$$

The above four equations form the governing set of equations for the fluid. We have made the implicit assumption that the fluid properties (bulk modulus, viscosity, thermal conductivity) are everywhere constant. To obtain a unique solution for a particular fluid geometry, we need to impose some boundary conditions. Normally we require that the fluid pressure equal its equilibrium value at a free surface and that the fluid cannot penetrate a solid surface. Since these solid surfaces are formed by structures that are seldom perfectly rigid, a fluid-structure interaction (FSI) must be considered. This is accomplished by simply requiring the normal component of fluid velocity to equal the structure velocity at the fluid-structure interface. Thus, we must augment the governing set of fluid equations with the equation of motion for the structure represented symbolically as

$$M \frac{\partial^2 w}{\partial t^2} + L^N(w) = p, \tag{3.9}$$

where w is the boundary displacement, M is the local mass per unit area, and L^N is a space operator of order N describing the local structural restraining force per unit area.

Upon inspection, it is readily apparent that analytical solutions to the above set of coupled nonlinear partial differential equations would be such a formidable task that such solutions would be rare. Therefore, in general we rely on numerical techniques in the form of finite-difference or finite-element computer programs. Numerical solutions are in principle quite adequate. However, in practice they do not contain all the physical insight to which one is accustomed from analytical solutions. It will be shown that if certain assumptions are made this set of equations will collapse to a single equation of acoustic fluid motion which will have a straightforward analytic solution for Mark II and 4T suppression pool geometries. If these assumptions can be justified, we will obtain the physical insight and at the same time maintain an adequate representation of chugging.

3.3 Assumptions and their Justification

The theory of sound deals with systematic motions of a fluid relative to an equilibrium state. Such perturbations of state can be described by incremental or acoustic variables and approximate equations governing them can be obtained by linearizing the general equations of motion given above. These results, as well as higher order approximations, can be derived in an orderly way by invoking a modified perturbation analysis[15,16]. This consists of replacing the dependent variables appearing in Eqs. (3.5) through (3.9) with the sum of their equilibrium or zero-order values and their first- and second-order variational components and then forming the separate equations that must be satisfied by the variables of each order. The resulting first-order equations, with the assumption of isentropic behavior of

the fluid, yield the scalar wave equation of classical acoustics which has analytic solutions. The second-order equations, however, have no general solution but are useful for making approximations and investigating some second-order phenomena that cannot be predicted by the first-order equations alone. If an analytic solution is sought, some rationale must be given to show that the second-order effects can safely be neglected.

Thus, we proceed in the same spirit as the modified perturbation analysis except we explicitly make three a priori assumptions: (1) the fluid motion is isentropic, (2) the change in the fluid pressure is proportional to the change in the fluid density, and (3) the velocity of the fluid particles is small compared with the velocity of sound. In addition, we also implicitly assume average values for the fluid properties and that the fluid is at rest. To justify these assumptions, we first separate the fluid pressure and density into an equilibrium value plus a small acoustic part

$$P = p_o + p \qquad \rho = \rho_o + \delta, \tag{3.10}$$

and then proceed as follows:

(1) Isentropic Fluid Motion $(\frac{ds}{dt} = 0)$

We write the general equation of heat transfer expressing the conservation of energy (Eq. (3.7)) in the following form:

$$\rho T \frac{ds}{dt} = \rho T \left(\frac{\partial s}{\partial t} + \vec{u} \cdot \nabla s\right) = \nabla \cdot (\kappa \nabla T) + \vec{\tau} : \nabla \vec{u} \quad . \tag{3.11}$$

For reversible adiabatic or isentropic fluid motion, the above equation vanishes. To be able to approximate the fluid as an isentropic fluid, we must show that thermal conductivity and viscosity are unimportant, i.e., the fluid is ideal. The left-hand side of Eq. (3.11) is the quantity of heat gained per unit volume per unit time at the expense of the mechanical energy of a sound wave. Therefore, the

sound wave is damped out in time. This subject is treated extensively in the literature[17-20] whereby one can calculate the rate of acoustic energy loss to be so slight as to warrant the neglect of viscosity and thermal conduction.

Therefore, to a good approximation, the fluid may be considered as ideal, i.e., the effects of viscosity and thermal conductivity can be neglected. Therefore,, $ds/dt = 0$ and the fluid is said to be isentropic.

(2) First-Order Equation of State, $[p = (\frac{\partial P}{\partial \rho}_s) \delta]$

Since the fluid is isentropic, the equation of state is a function of the fluid density only and can obviously be expanded in a Taylor series in the term δ/ρ_o (called the "condensation")

$$P = p_o + A (\frac{\delta}{\rho_o}) + \frac{B}{2!} (\frac{\delta}{\rho_o})^2 + \frac{C}{3!} (\frac{\delta}{\rho_o})^3 + \ldots , \qquad (3.12)$$

where $A = \rho_o c^2$ since $(dP/d\rho)_s \equiv c^2$. By application of thermodynamic formulae for the isentropic derivatives of the pressure with respect to density, the ratios B/A and C/A can be computed[21]. For water, the numerical values for these ratios are $B/A < 6$ and $C/A < 39$ where $p_o <$ 24.5 MPa (3553 psia) and T = 30°C (86°F). Keeping only the linear term in Eq. (3.12), we write

$$p = A (\frac{\delta}{\rho_o}) = c^2 \delta \quad . \qquad (3.13)$$

If this first-order equation of state is used instead of the Taylor series expansion, it can be quickly shown that we are in error by no more than 1% when the condensation δ/ρ_o is less than 0.0032. A condensation this large would produce an acoustic pressure p in excess of 73 atm (7.4 MPa or 1073 psi) -- far larger than any chug possible in a Mark II boiling water reactor (BWR).

(3) Linear Equation of Motion ($u << c$)

Since the assumption of isentropic fluid motion is tantamount to neglecting fluid viscosity and thermal conductivity, the equation of motion (Eq. (3.6)) reduces to Euler's equation

$$\frac{\partial \vec{u}}{\partial t} + (\vec{u} \cdot \nabla)\,\vec{u} = -\frac{1}{\rho}\nabla P \quad . \qquad (3.14)$$

We now explore under what conditions it is justified to omit the nonlinear term $(\vec{u} \cdot \nabla)\vec{u}$ compared with the other two terms. We are interested in the relative order of magnitude of the terms of Eq. (3.14) in connection with the propagation of sound waves. Therefore, we introduce for the characteristic time and length over which the sound wave changes appreciably the period T and the length λ of the wave, so that $\partial/\partial t \sim 1/T$ and $\nabla \sim 1/\lambda$. Then, to obtain the relative orders of magnitude of the different terms, we use the property of plane waves that $p = \rho c u$. Thus, the relative orders of magnitude of the terms in Eq. (3.14) are: 1, u/c, 1. The condition, then, that the fluid equation of motion be linear is $u << c$.

To establish the validity of this assumption (and the previous one concerning the condensation δ/ρ_o), we resort to a numerical solution of the conservation equations for mass, momentum, and energy in a rigid circular tank similar to the 4T facility. We use a nationally available computer code K-FIX[22] to solve the above system of equations subject to the specified boundary conditions. The K-FIX computer code uses a two-fluid model to simulate transient, two-dimensional, two-phase flow. The two phases have different densities, velocities, and temperatures determined by separate mass, momentum, and energy equations. The conservation equations are written in finite difference form for their numerical solution. The nonlinear finite difference equations are solved iteratively using a point relaxation technique. The geometric region of interest is divided into many finite-size, space-fixed cells that collectively form the computing

mesh. In cylindrical geometry, the cells are toroids with rectangular cross section. The pressure, density, and internal energy are computed at the cell center while the components of the velocity are computed at the cell boundary. The K-FIX model of a tank-vent system is shown in Fig. 3-3. This is an axisymmetric model. Only the water in the tank and the steam in the vent are modeled; the air above the water is neglected.

The problem is now sufficiently specified to obtain a solution using K-FIX. All that remains is a description of the chug source as input to K-FIX. We choose to simulate a Category I chug because this type of chug has the largest pressure excursions and will be the most severe test of our assumptions. We will assume the collapse of an isolated steam bubble for conservatism. In principle, the source could be specified with K-FIX by modeling the collapse of a cavity. This is not practical, however, because of the large number of computational cells required to track the collapse. Instead, we specify the pressure time-history in the cells immediately adjacent to the steam-water interface at the vent exit. Using the Florscheutz and Chao model with increased heat transfer rates due to the turbulent conditions at the vent exit yields the bubble pressure time-histories shown in Fig. 3-4. The Florscheutz and Chao model treats the collapse of a spherically symmetric steam bubble in an infinite sea. The calculated flow field, therefore, will not conform to the actual flow field in 4T. Thus, the pressure time-history in Fig. 3-4 serves only to obtain a plausible time-history shape. Other choices such as an impulse yield the same conclusions. Since the collapse time relative to the acoustic ringout is short, the precise shape is not vital and we shall idealize the pressure source given in Fig. 3-4 with

$$p(t) = p_1 \Lambda(2t/\tau_1 - 1) + p_2 \Lambda \left(\frac{2t - 2\tau_1}{\tau_2} - 1\right) \qquad (3.15)$$

where $\Lambda(x)$ is given by Eq. (3.3). This pressure source has the time dependence shown in Fig. 3-5.

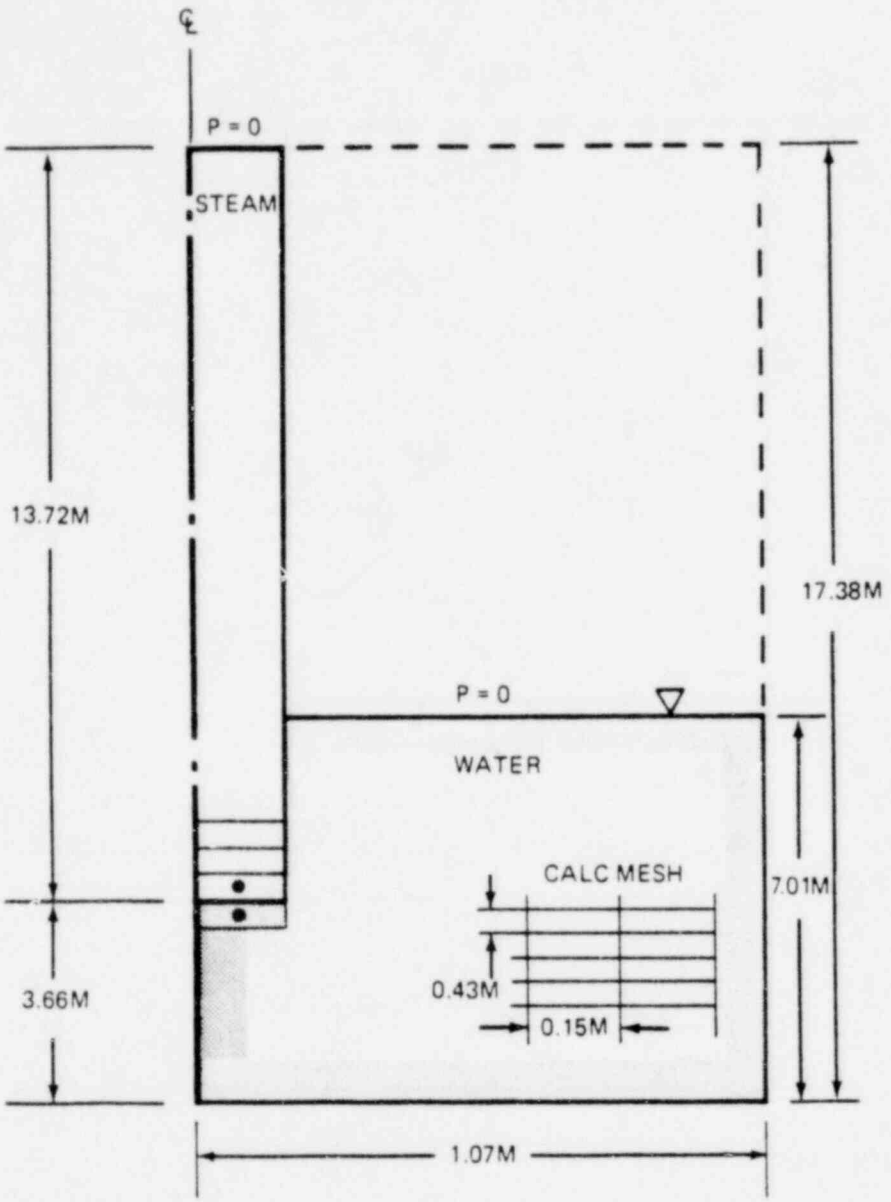

Figure 3-3 K-FIX Model

G1002820-12-01

	T_s °C/°F	T_{c_0} SEC	P_∞ kPa/PSI
1	110/230	0.012	138/20
2	138/280	0.061	298/43
3	138/280	0.036	298/43

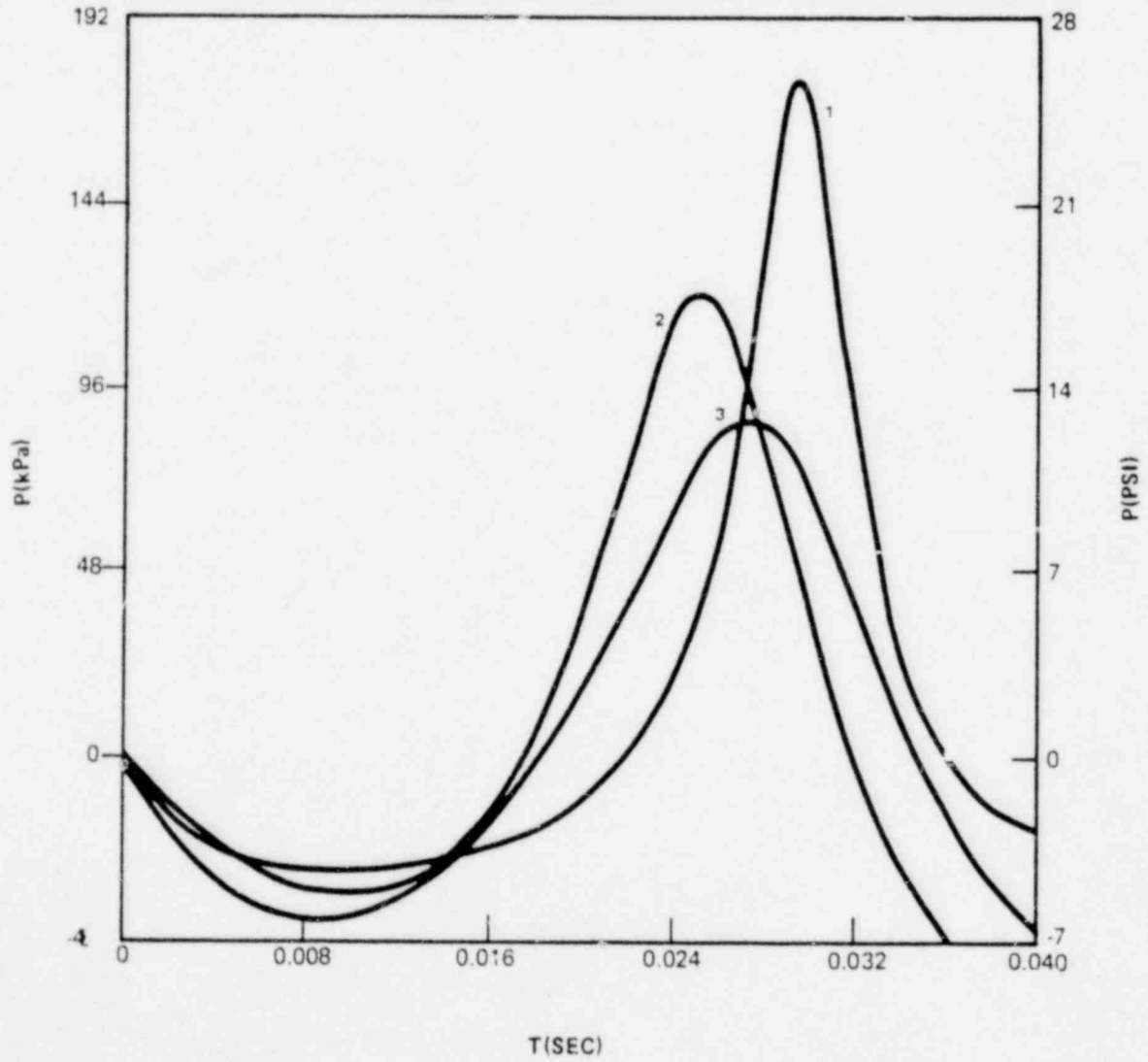

Figure 3-4 Bubble Pressure Time-Histories During Collapse[9]

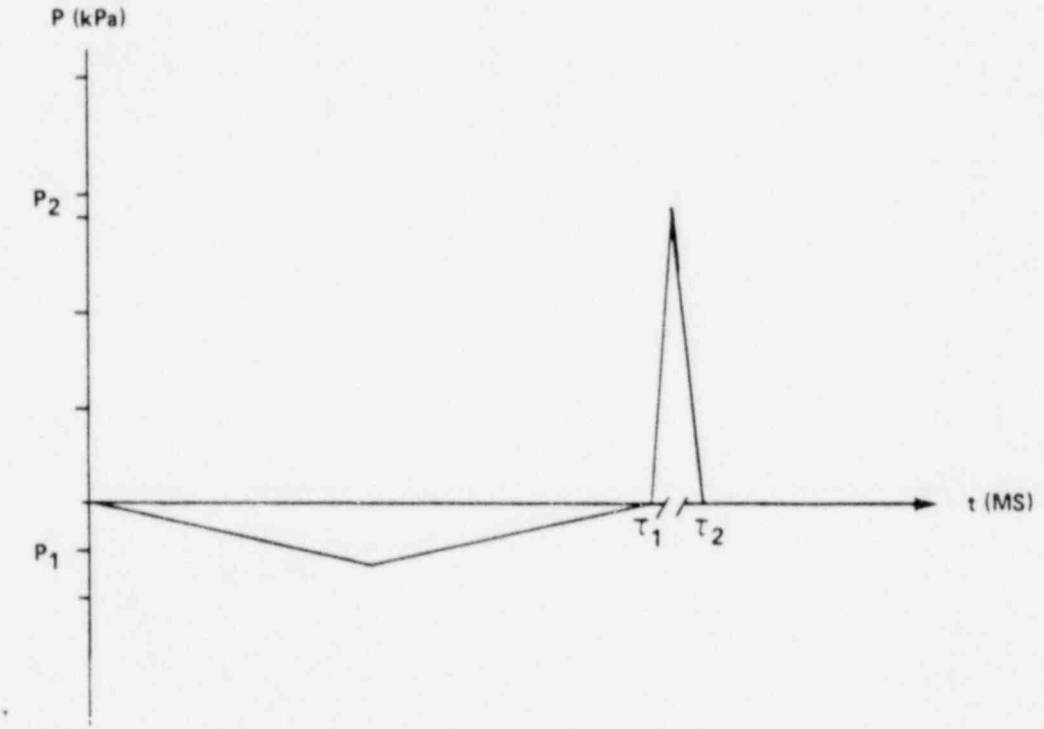

Figure 3-5 Semiempirical K-FIX Pressure Source

By reviewing the pressure transients in the vicinity of the vent observed during the Anamet bell jar tests[5], values for the constants P_1, P_2, τ_1, τ_2, in Equation (3.15) can be obtained. A collapse time for the bell jar was observed when the air space above the water was vented to the atmosphere. Following the collapse, a pressure transducer in the vent recorded a transient. When the air space has the same pressure as that during the 4T Phase I, II, and III tests the collapse time would be less. In the absence of an experimental measurement, we can crudely estimate the collapse time corresponding to a pressurized air space as follows. We learn from the collapse of a spherical void in an infinite sea that the collapse time is proportional to the inverse of the square root of the ambient pressure[13]. For an overpressure of 275.79 kPa (40 psia), the collapse time should be roughly 50 ms. Thus, we choose τ_1 = 50 ms and τ_2 = 56 ms. These values compare favorably with Fig. 3-4 when one considers that it can be shown that collapse in a confined geometry takes longer than in an infinite sea. We choose p_1 = -5.24 kPa (-0.76 psid) and p_2 = 32.82 kPa (4.76 psid) to simulate tank bottom-center and vent pressure amplitudes.

We apply Eq. (3.15) to the cell located in the water at the vent exit. Since the source also excites the vent, Eq. (3.15) is also applied simultaneously to the first cell in the vent adjacent to the steam-water interface. These two cells are indicated in Fig. 3-3 with a black dot. The tank bottom-center pressure and the vent midpoint pressure computed by K-FIX are shown in Fig. 3-6 and their respective power spectral densities (PSDs) in Fig. 3-7. The computation mesh was examined to find that $|\delta| \lesssim 0.01$ kg m^{-3} (6.24×10^{-4} lbm/ft^3) and $|u| \lesssim 0.02$ m/s (0.8 in/s). The damping exhibited in Fig. 3-6 has no physical basis because the boundary conditions in this calculation are rigid wall boundary conditions and viscosity and heat conduction have been neglected. Rather, the damping is due to "numerical diffusion" arising from the solution method chosen in K-FIX. Since we are not drawing conclusions related to damping, it is of no consequence.

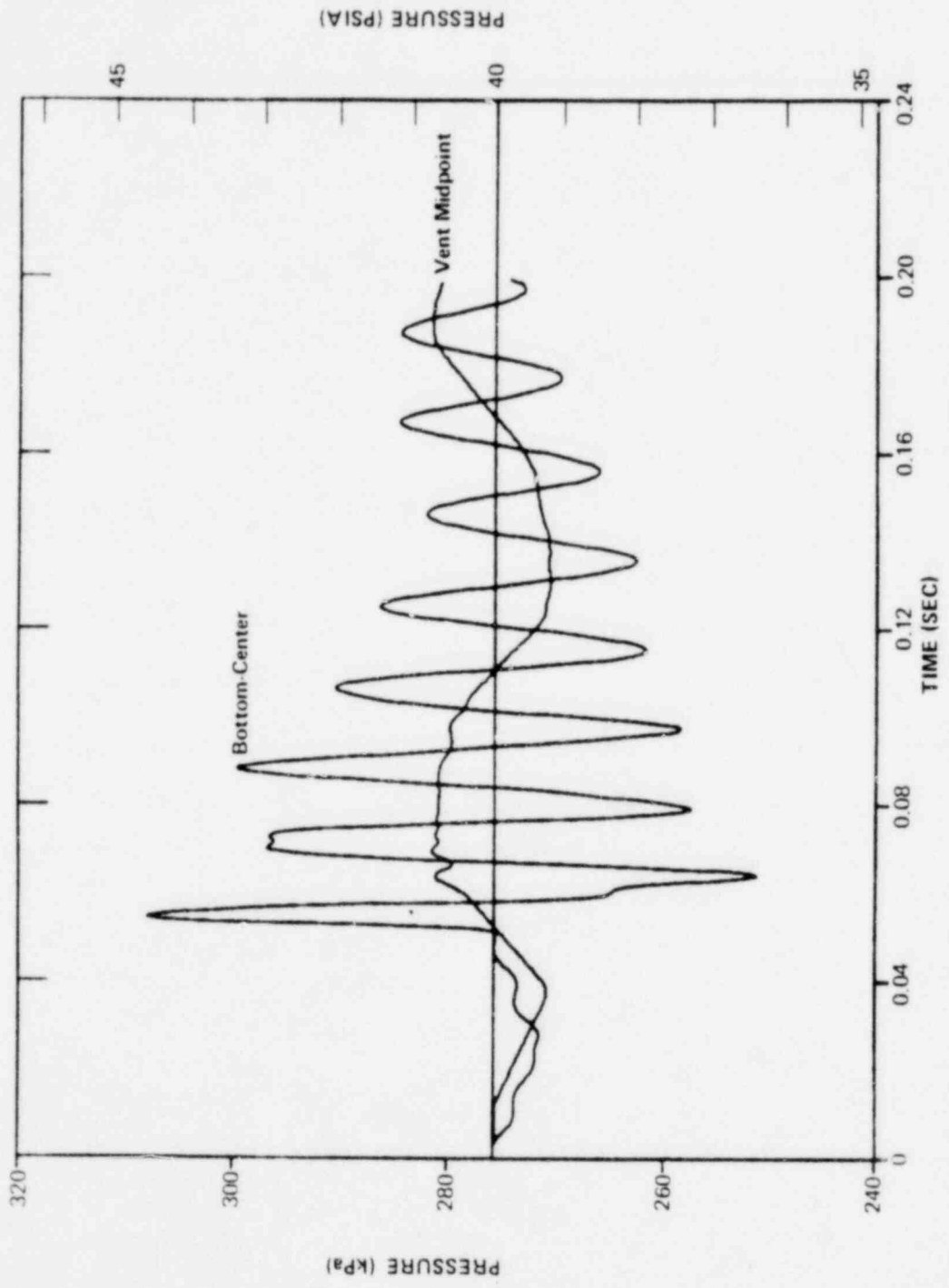

Figure 3-6 K-FIX Chug Simulation

G1002820 45

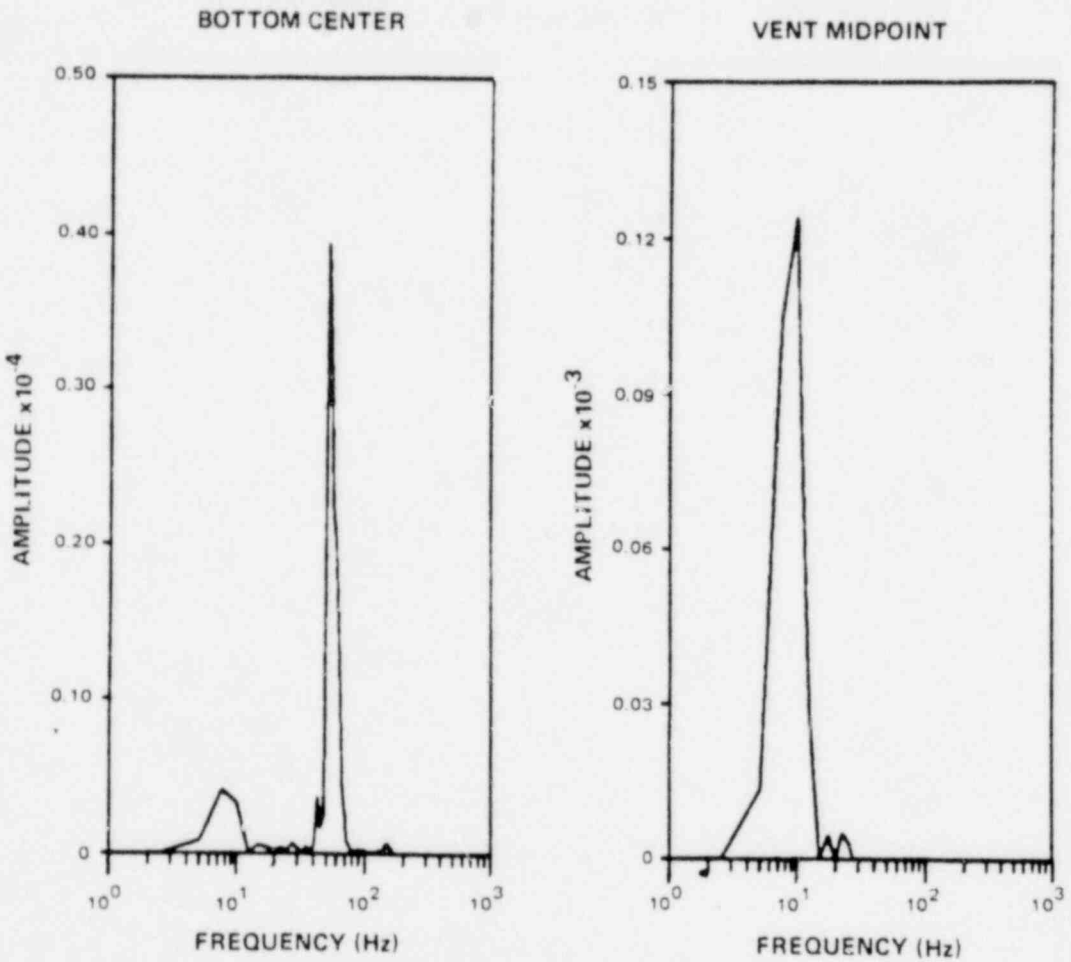

Figure 3-7 K-FIX Power Spectral Densities

Thus, we conclude from the K-FIX calculation:

(1) The linear fluid equations of motion are an excellent approximation because $u \ll c$ and $\delta \ll \rho_o$.

(2) The vent and tank are not strongly acoustically coupled, i.e., each responds at its own eigenfrequency.

(3) The vent serves as an acoustic source to the tank in addition to the chug impulse.

We have now verified our three assumptions; thus, the conservation equations reduce to the acoustic wave equation. To show this, we rewrite the conservation equations subject to our assumptions

$$\frac{\partial \delta}{\partial t} + \rho_o \nabla \cdot \vec{u} = 0 \tag{3.16a}$$

$$\rho_o \frac{\partial \vec{u}}{\partial t} = - \nabla p \tag{3.16b}$$

where the energy conservation equation vanishes since $ds/dt = 0$, and we have implicitly assumed that $\nabla \times \vec{u} = 0$.

This reduces to the acoustic wave equation

$$\Box^2 p = \nabla^2 p - \frac{1}{c^2} \frac{\partial^2 p}{\partial t^2} = 0 \tag{3.17}$$

For the case where sources of acoustic energy are present, such as impulsive steam bubble collapse and the vent response to that collapse, the wave equation becomes

$$\Box^2 p(\vec{r},t) = -4\pi q(\vec{r},t), \tag{3.18}$$

where $q(\vec{r},t)$ represents the acoustic sources.

4. ACOUSTIC MODEL OF CHUGGING

Having demonstrated the acoustic nature of chugging in Chapters 2 and 3, we must now develop a theoretical model that accounts for the observed phenomena in the 4T tests. Numerical codes (such as K-FIX and NASTRAN) are very costly, and an analytical solution would result in more reasonable computer costs. Additionally, analytical solutions permit a better understanding of the physics of the problem. Thus, using the results of the numerical code K-FIX and the bell jar tests, simplifying assumptions can be made which reduce the complexity of the problem and permit an analytical solution. The code IWEGS (Inhomogeneous Wave Equation Green's function Solution) was developed to obtain the numerical results of the analytical solution. The form of the analytical solution is such that extension from the simple cylindrical geometry of the 4T to the more complicated annular geometry of the Mark II is straightforward, as will be seen later in Section 4.2.

4.1 Wave Equation Solution in 4T Geometry

The development of the acoustic chugging model is based on two assumptions substantiated by the results of the previous chapter:

(1) The linear wave equation applies and
(2) The vent is not acoustically coupled to the pool.

The results of the previous section indicate that the linearized equations of motion which lead to the wave equation may be employed. Nonlinear effects, such as wave shape steepening or shock waves, were not observed in the Anamet or K-FIX results. This is consistent with another large amplitude phenomenon, water hammer, the analysis of which has been successfully accomplished by the wave equation.

The results of K-FIX calculations of pressure in the vent show these oscillations to be at the vent natural frequencies and independent of the natural frequency of the pool pressure oscillations. Hence, the vent may be considered to be acoustically decoupled from the pool and its effect included in the source.

Forced wave motion in compressible fluids is described by the inhomogeneous wave equation

$$\Box^2 p(\vec{r},t) = -4\pi q(\vec{r},t) \tag{4.1}$$

where

p = acoustic pressure

$\Box^2 = \nabla^2 - \frac{1}{c^2}\frac{\partial^2}{\partial t^2}$ D'Alembertian operator

$q(\vec{r},t)$ = source density distribution function describing spatial and temporal distribution of the driving force.

The solution of Eq. (4.1) is obtained in a straightforward manner by the Green's function method[23,24] as represented by the following volume and surface integrals

$$p(\vec{r},t) = \int_o^{t^+} dt_o \int_V dV_o \; G(\vec{r},t|\vec{r}_o,t_o) q(\vec{r}_o,t_o)$$

$$+ \frac{1}{4\pi}\int_o^{t^+} dt_o \oint_S d\vec{S}_o \cdot [G(\vec{r},t|\vec{r}_o,t_o)\nabla_o p(\vec{r}_o,t_o) - p(\vec{r}_o,t_o)\nabla_o G(\vec{r},t|\vec{r}_o,t_o)] \tag{4.2}$$

for a fluid which is initially at rest. By the symbol t^+ we mean $t + \varepsilon$ where ε is arbitrarily small. This limit is employed in order to avoid terminating the integration at the apex of a delta function.

The time-dependent Green's function $G \equiv G(\vec{r},t|\vec{r}_o,t_o)$ is the solution of

$$\Box^2 G(\vec{r},t|\vec{r}_o,t_o) = -4\pi\delta(\vec{r} - \vec{r}_o)\,\delta(t - t_o) \quad . \tag{4.3}$$

We see that the source in Eq. (4.3) is an impulse at $t = t_o$ located at $\vec{r} = \vec{r}_o$. $G(\vec{r},t|\vec{r}_o,t_o)$ then gives the description of the effect of this impulse as it propagates away from $\vec{r} = \vec{r}_o$ during the course of time.

The first integral on the right of Eq. (4.2) represents the effect of the sources; the second represents the effect of the boundary conditions on the space boundaries. We wish to use Eq. (4.2) to describe the pressure field in the fluid region of a perfectly rigid 4T. The solution for flexible wall geometries will be given in Chapter 5. For the collapse of a steam bubble attached to the 4T vent, we could, in principle, apply Eq. (4.2) with $q(\vec{r},t) \equiv 0$. The bubble surface is a complicated part of the boundary enclosing the fluid region. Only that part of the surface integral of Eq. (4.2) at the bubble-water interface will contribute to $p(\vec{r},t)$ in our idealized rigid 4T. Thus, a description of the interface motion is required -- something we have been trying to avoid. Also, the solution of Eq. (4.3) in the 4T geometry will require the joining of the two solutions in the regions above and below the vent exit. Such a solution for G is not tractable[25]. For these reasons, we will approximate the 4T geometry in the fluid region of Fig. 4-1 with the simpler geometry shown in Fig. 4-2. We neglect the presence of the 4T vent and treat the collapsing steam bubble as a point source:

$$q(\vec{r},t) = \rho\delta(\vec{r} - \vec{r}_o)\,S(t) \quad . \tag{4.4}$$

This is an excellent approximation because both the vent and bubble are small compared to the tank diameter and the wave length of the resulting pressure wave. This is evident from a simple calculation. The maximum bubble diameter is believed to be equal to one vent diameter, 508 or 610 mm (20 or 24 in.). The tank diameter is 2.13 m

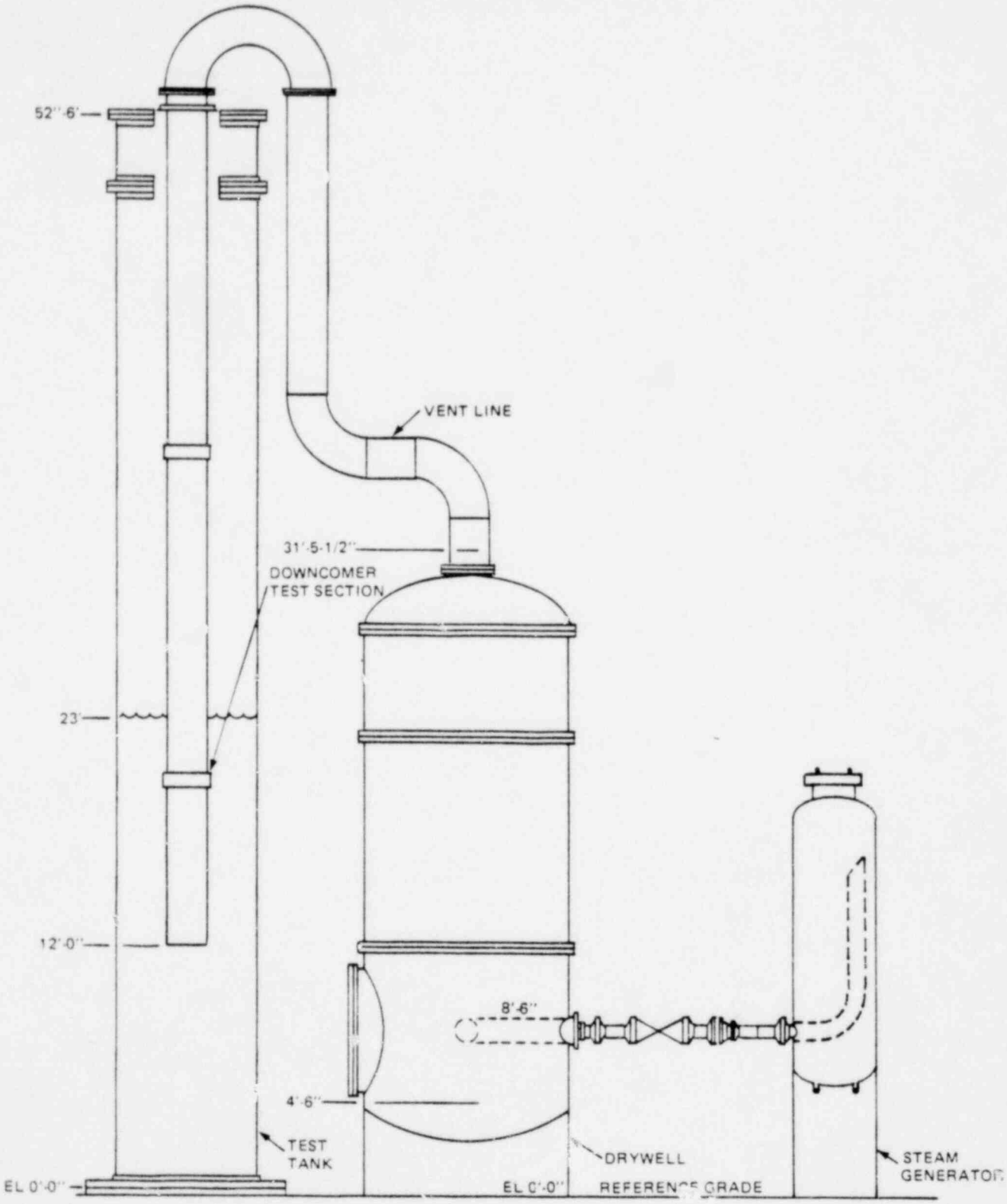

Figure 4-1 4T Test Facility Schematic

G1002820 11

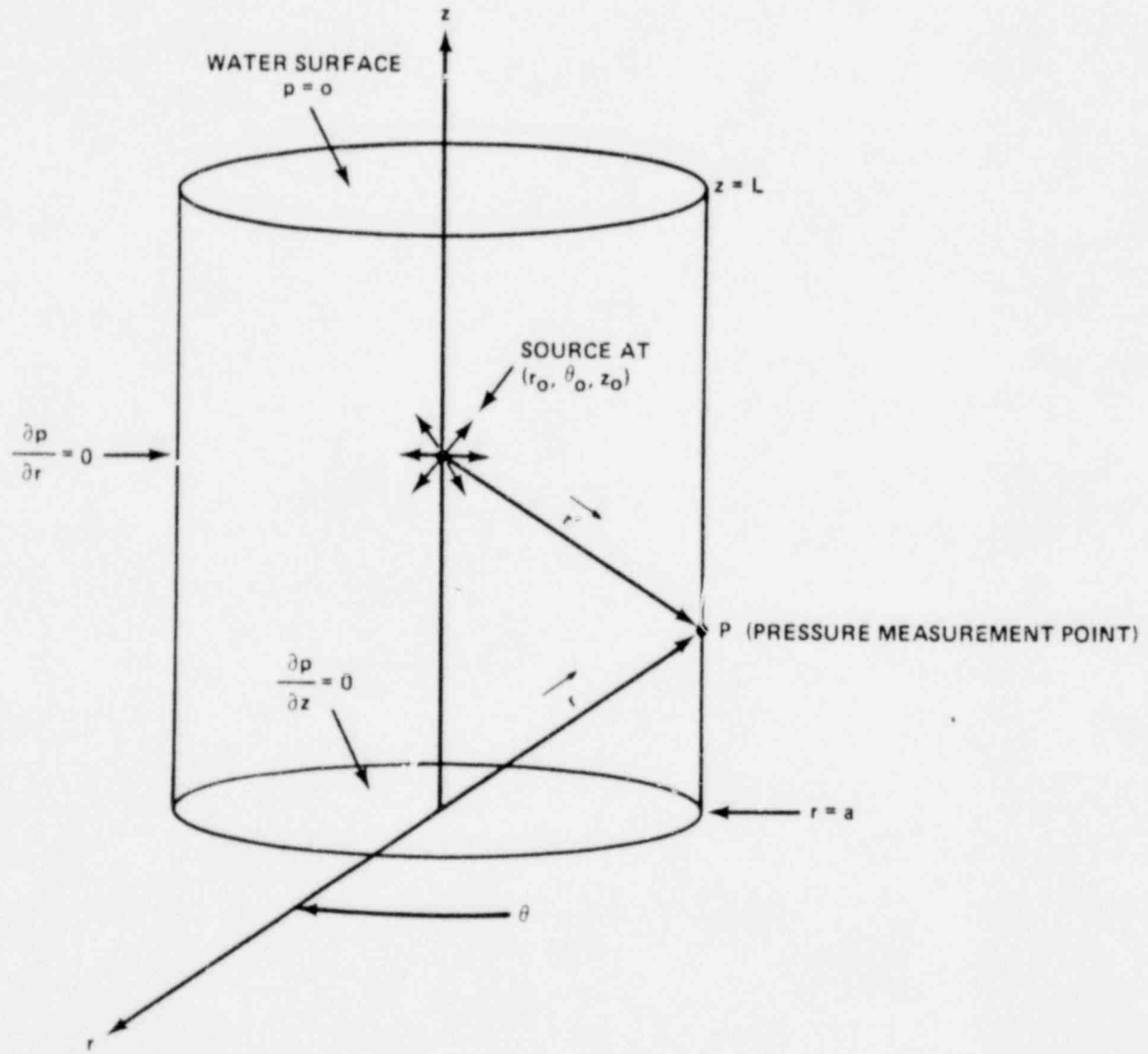

Figure 4-2 4T Acoustic Model Geometry

G1002820 01-01

(7 ft) or at least 3.5 times larger than the bubble or vent. The wave length of a 25 Hz standing pressure wave is 28 m (92 ft) (using c = 701 m/s or 2300 fps), or 46 times larger than the bubble. Thus, we add a third assumption to those previously enumerated:

(3) The source can be represented by a point source.

Under these approximations, the solution of Eq. (4.1) is given by

$$p(\vec{r},t) = \int_0^{t+} dt_o \int_V dV_o G(\vec{r},t|\vec{r}_o,t_o) q(\vec{r}_o,t_o) \quad . \tag{4.5}$$

If we define the Fourier transform (in time) of the time dependent Green's function via[26]

$$G(\vec{r},t|\vec{r}_o,t_o) = \frac{1}{2\pi} \int_{-\infty}^{\infty} G_k(\vec{r},\vec{r}_o)\, e^{-i\omega(t-t_o)}\, d\omega \ , \tag{4.6}$$

expanding G_k in a series of normal modes for the 4T geometry results in

$$G_k(\vec{r},\vec{r}_o) = 4\pi \sum_n \frac{\phi_n(\vec{r}_o)\, \phi_n(\vec{r})}{V\Lambda_n \left[k_n^2 - \left(\frac{\omega}{c}\right)^2\right]} \ , \tag{4.7}$$

where the ϕ_n are the eigenfunctions of the Helmholtz equation,

$$\nabla^2 \phi_n + k_n^2 \phi_n = 0 \ . \tag{4.8}$$

The boundary conditions for the rigid wall cylinder are:

$$\text{At } r = a \qquad \frac{\partial \phi_n}{\partial r} = 0 \qquad \text{(rigid wall)} \tag{4.9}$$

$$\text{At } z = 0 \qquad \frac{\partial \phi_n}{\partial z} = 0 \qquad \text{(rigid bottom)} \tag{4.10}$$

$$\text{At } z = L \qquad \phi_n = 0 \qquad \text{(water surface).} \tag{4.11}$$

Eq. (4.8) is solved in cylindrical coordinates with boundary conditions, Eqs. (4.9), (4.10), and (4.11), resulting in

$$\phi_n(\vec{r}) = J_m\left(\frac{\pi\alpha_{mn}}{a} r\right) \begin{matrix}\sin\\ \cos\end{matrix} (m\theta) \cos\left[\left(\ell + \frac{1}{2}\right)\frac{\pi}{L} z\right] \tag{4.12}$$

where n represents the quantum number trio n,m,ℓ which has integer values equal to 0,1,2, ... The eigenfunctions ϕ_n satisfy the orthonormal condition

$$\int \phi_m(\vec{r})\ \phi_n(\vec{r})\ dV = V\Lambda_n\ \delta_{mn} \tag{4.13}$$

where δ_{mn} is the Kronecker delta. The normalization constant Λ_n is given by

$$V\Lambda_n \equiv V\Lambda_{n,m} = \frac{\pi a\ L}{2\varepsilon_m}\left[1-\left(\frac{m}{\pi\alpha_{mn}}\right)^2\right]J_m^2(\pi\alpha_{mn}), \tag{4.14}$$

where $\varepsilon_m = 2(1+\delta_{om})^{-1}$. The eigenvalue α_{mn} is defined by

$$J_m'(\pi\alpha_{mn}) = 0, \tag{4.15}$$

where J_m' is the derivative of J_m with respect to its argument. A few values of α_{mn} are

$$\begin{aligned}
&\alpha_{00} = 0.0000 \quad \alpha_{01} = 1.2197 \quad \alpha_{02} = 2.2331 \quad \cdots\\
&\alpha_{10} = 0.5861 \quad \alpha_{11} = 1.6970 \quad \alpha_{12} = 2.7140 \quad \cdots\\
&\alpha_{20} = 0.9722 \quad \alpha_{21} = 2.1346 \quad \alpha_{22} = 3.1734 \quad \cdots\\
&\alpha_{mn} \to n + \tfrac{1}{2}m - \tfrac{3}{4} \qquad m < n >> 1.
\end{aligned} \tag{4.16}$$

Eq. (4.5), together with Eqs. (4.4) and (4.7), yield

$$p(\vec{r},t) = \frac{8\rho c^2}{a^2 L} \sum_n \frac{\varepsilon_m \, \Omega_N(\vec{r}_o) \, \Omega_N(\vec{r})}{\omega_n \left[1-\left(\frac{m}{\pi\alpha_{mn}}\right)^2\right] J_m^2(\pi\alpha_{mn})} \int_o^{t^+} S(t_o) \sin[\omega_n(t-t_o)]dt_o, \tag{4.17}$$

where

$$\Omega_n(\vec{r}) = J_m\left(\frac{\pi\alpha_{mn}}{a} r\right) \cos\left[\left(\ell + \tfrac{1}{2}\right) \frac{\pi}{L} z\right] \tag{4.18}$$

$$\Omega_n(\vec{r}_o) = J_m\left(\frac{\pi\alpha_{mn}}{a} r_o\right) \cos[m(\theta-\theta_o)] \cos\left[\left(\ell + \tfrac{1}{2}\right) \frac{\pi}{L} z_o\right] \tag{4.19}$$

$$(\omega_n/c)^2 = (\pi\alpha_{mn}/a)^2 + \left(\ell + \tfrac{1}{2}\right)^2 (\pi/L)^2 \quad . \tag{4.20}$$

Applying Eq. (4.17) to the 4T with a single source on the tank centerline, $r_o = 0$, $\theta_o = 0$, the acoustic pressure field is given by

$$p(\vec{r},t) = \frac{8\rho c^2}{a^2 L} \sum_n \sum_\ell \frac{J_o(\pi\alpha_{on} \frac{r}{a}) \cos\left[\left(\ell+\frac{1}{2}\right) \frac{\pi}{L} z\right] \cos\left[\left(\ell+\frac{1}{2}\right) \frac{\pi}{L} z_o\right]}{\omega_n \, J_o^2(\pi\alpha_{on})}$$

$$\cdot \int_o^{t^+} S(t_o) \sin[\omega_n(t-t_o)]dt_o. \tag{4.21}$$

This equation presents no computational difficulties providing the integral and sum are evaluated accurately. Tables of the roots of $J_o(x)$ are available in the literature[27]. A note of caution, however, is in order. When evaluating the sum over ℓ in Eq. (4.21), enough terms must be included to ensure convergence to a desired level of

accuracy. Eq. (4.7) is a "retarded" Green's function. That is, for values of t such that $ct < |\vec{r} - \vec{r}_o|$, the double sum in Eq. (4.21) is zero. This expresses the fact of a finite propagation time from source to observation point. For times on the order of $\frac{1}{c}|\vec{r} - \vec{r}_o|$, many terms in the sum over ℓ are necessary to demonstrate this effect. As t increases such that $ct > |\vec{r} - \vec{r}_o|$, the number of terms in the ℓ-sum to obtain a reasonable estimate of the unbounded sum is on the order of ten.

4.2 Wave Equation Solution in Mark II Geometry

This section will describe how the theoretical acoustic model developed in Section 4.1 is extended to the multivent annular geometry of the Mark II containment. The code developed to perform the Mark II computations is called IWEGS/MARS (Multivent, Annular System).

As in the cylindrical acoustic model described in Section 4.1, the Mark II acoustic model rests on the same three basic assumptions:

(1) The linear wave equation applies,
(2) The vent is not acoustically coupled to the pool, and
(3) The sources can be represented by a point source.

The Mark II acoustic model is also used for the solution of the inhomogeneous wave equation, Eq. (4.1). Only the geometry and number of sources are changed (see Fig. 4-3). The point of departure is the solution of the Helmholtz equation, Eq. (4.8), for the annular geometry,

$$\nabla^2 \phi_n + k_n^2 \phi_n = 0 \quad . \tag{4.22}$$

The boundary conditions specified by the annular problem are:

$$\text{At } r = a \qquad \frac{\partial \phi_n}{\partial r} = 0 \qquad \text{(rigid outer wall)} \tag{4.23}$$

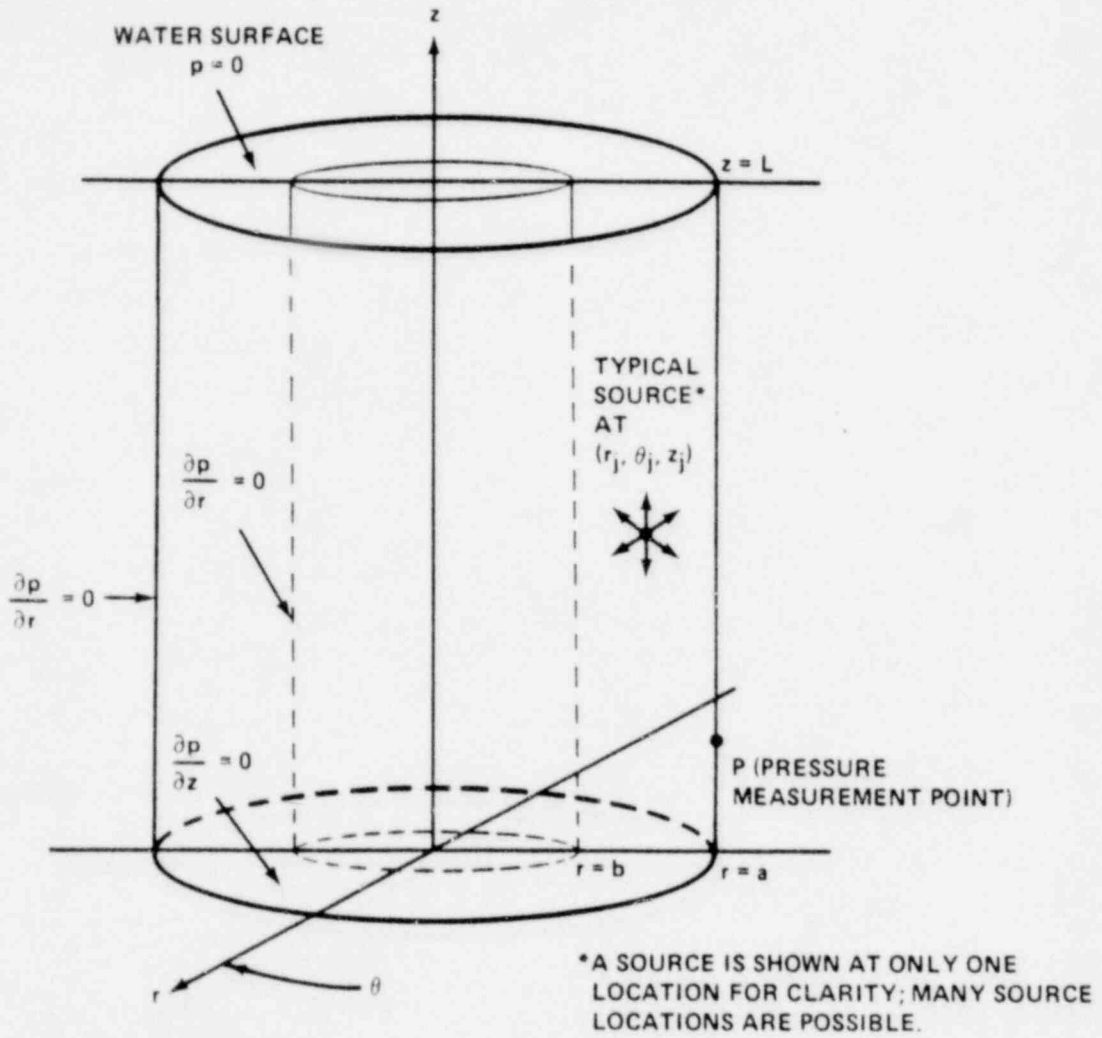

Figure 4-3 Mark II Acoustic Model Geometry

G1002820 56-01

$$\text{At } r = b \qquad \frac{\partial \phi_n}{\partial r} = 0 \qquad \text{(rigid inner wall)} \tag{4.24}$$

$$\text{At } z = 0 \qquad \frac{\partial \phi_n}{\partial z} = 0 \qquad \text{(rigid bottom)} \tag{4.25}$$

$$\text{At } z = L \qquad \phi_n = 0 \qquad \text{(water surface).} \tag{4.26}$$

Equation (4.22) is solved in cylindrical coordinates with boundary conditions, Eqs. (4.23), (4.24), (4.25), and (4.26), resulting in

$$\phi_n(\vec{r}) = \zeta_{mn}(r) \begin{matrix} \sin \\ \cos \end{matrix} (m\theta) \cos[(\ell+\tfrac{1}{2}) \tfrac{\pi}{L} z] \tag{4.27}$$

where, as before, n represents the quantum number trio n,m,ℓ which has integer values equal to 0,1,2, ... The eigenfunctions ϕ_n satisfy Eq. (4.13) which determines the normalization constant $V\Lambda_n$ (see Eq. (4.13)). The radial function $\zeta_{mn}(r)$ is

$$\zeta_{mn}(r) = J_m(\frac{\pi\gamma_{mn} r}{a}) - \frac{J'_m(\pi\gamma_{mn} b/a)}{N'_m(\pi\gamma_{mn} b/a)} N_m(\frac{\pi\gamma_{mn} r}{a}), \tag{4.28}$$

where the eigenvalues $\pi\gamma_{mn}$ are defined by the roots of

$$J'_m(\pi\gamma_{mn})\, N'_m(\pi\gamma_{mn} b/a) - J'_m(\pi\gamma_{mn} b/a)\, N'_m(\pi\gamma_{mn}) = 0 \quad , \tag{4.29}$$

J'_m and N'_m being the derivatives of J_m and N_m with respect to their arguments. The roots of Eq. (4.29) are also available in the literature[28].

For multiple sources of strength $S_j(t_o)$ located at coordinates (r_j, θ_j, z_j), the source distribution function becomes

$$q(\vec{r}_o, t_o) = \rho \sum_j S_j(t_o) \frac{1}{r} \delta(r_o - r_j)\, \delta(\theta_o - \theta_j)\, \delta(z_o - z_j), \tag{4.30}$$

where

$$S_j(t_o) = S_o(t_o - t_j)\, u(t_o - t_j) \quad , \tag{4.31}$$

$u(t)$ is the unit step function, and t_j is the initiation time of the j^{th} source. The source function $S_o(t)$ is the Mark II chugging source derived from the 4T chugging source and assumed to occur at each vent exit.

Eq. (4.30), together with the Fourier transform of Eq. (4.7), are inserted into Eq. (4.5), resulting in

$$p(\vec{r},t) = 2\pi\rho c^2 \sum_n \frac{\Omega_n(\vec{r})}{\omega_n V\Lambda_n} \sum_j \Omega_n(\vec{r}_j) \int_o^{t^+} S_j(t_o) \sin[\omega_n(t-t_o)]\, dt_o, \tag{4.32}$$

where

$$\Omega_n(\vec{r}) = \zeta_{mn}(\vec{r}) \cos[(\ell + \tfrac{1}{2}) \tfrac{\pi}{L} z] \tag{4.33}$$

$$\Omega_n(\vec{r}_j) = \zeta_{mn}(r_j) \cos[m(\theta - \theta_j)] \cos[(\ell + \tfrac{1}{2}) \tfrac{\pi}{L} z_j] \tag{4.34}$$

$$V\Lambda_n = \frac{\pi a^2 L}{2\varepsilon_m} [\zeta_{mn}^2(a) - (\frac{b}{a})^2 \zeta_{mn}^2(b) - (\frac{m}{\pi\gamma_{mn}})^2 \{\zeta_{mn}^2(a) - \zeta_{mn}^2(b)\}] \; . \tag{4.35}$$

$$(\frac{\omega_n}{c})^2 = (\frac{\pi\gamma_{mn}}{a})^2 + (\ell + \tfrac{1}{2})^2 (\tfrac{\pi}{L})^2 . \tag{4.36}$$

Eq. (4.32) is evaluated numerically by the code IWEGS/MARS. Note that the roots of Eq. (4.29) are dependent on the containment diameter ratio b/a. Thus, the natural frequencies predicted by Eq. (4.36) will be different for each of the Mark II containments. Table 4-1 lists the five lowest frequencies for the Susquehanna containment. Notice that the first transverse mode has a frequency only 7 Hz greater than the fundamental.

Table 4-1

SUSQUEHANNA SUPPRESSION POOL NATURAL FREQUENCIES

m	n	ℓ[2]	Transverse Root, ($\pi\gamma_{mn}$)	Frequency, Hz[1] ($f_{mn\ell}$)	Mode
0	0	0	0.	54.35	fundamental
1	0	0	1.54512	61.12	1st tangential
2	0	0	2.93655	76.02	2nd tangential
3	0	0	4.16609	92.96	3rd tangential
0	1	0	4.88471	103.79	1st radial

Note (1): Solving Equation (4.29) with the following parameters:

c = 1524 m/s (5000 ft/s)

a = 13.4 m (43.96 ft)

b = 4.42 m (14.5 ft)

L = 7.01 m (23.0 ft)

Note (2): m index corresponds to azimuthal direction

n index corresponds to radial direction

ℓ index corresponds to axial direction

5. TREATMENT OF FLUID-STRUCTURE INTERACTION

In the previous two chapters, we have dealt with two of the three chugging elements: the chug source and the transfer function from that source through the fluid to the boundary. We now treat the remaining element of chugging: the fluid-structure interaction. In the exact technical sense, there will be an interaction between the fluid and the structure whenever the fluid is disturbed regardless of structure rigidity. This is a consequence of Newton's third law of motion. However, the term "fluid-structure interaction" (FSI) has come to mean the alteration of a rigid boundary pressure field by the response of the structure to that field. Thus, when we say there is no FSI we mean the structure is sufficiently rigid so that the pressure field is unaltered. This condition is seldom realized in practice and therefore the effects of FSI must be included in the structural assessment of chugging.

5.1 Separability of the Fluid-Structure Interaction Problem

We have explicitly assumed that the solution of the set of equations governing the behavior of the fluid and the structure could be obtained in two steps. First, the fluid equations would be solved for the case of rigid boundaries. We define rigid boundaries to be those where the normal component of fluid velocity (or equivalently pressure gradient) is zero. Next, the resulting rigid wall pressure p_1 would be input to the set of coupled equations which govern the structure and the fluid

$$L^N(w) + \rho_s \ddot{w} = p_1 + p_2 \tag{5.1}$$

$$\Box^2 p_2 = 0 \tag{5.2}$$

where L^N is a spatial differential operator of order N, ρ_s is the structural mass per unit area, and w is the boundary displacement. These equations are coupled by way of $(\partial p_2)/(\partial n)|_s = \rho\ddot{w}$ evaluated at the fluid-structure interface; p_2 is the pressure field generated by

the motion of that interface. Equations (5.1) and (5.2) are usually extensive and are solved by a fluid-structure computer program such as NASTRAN[29-32]. This method of solution of a coupled fluid-structure problem is illustrated in Fig. 5-1.

In work sponsored by the Nuclear Regulatory Commission, Sonin[33] has established the validity of this method of solution of the coupled fluid-structure problem subject to assumptions of small amplitudes and linearity. Because of the importance of the method of separability in obtaining Mark II chugging responses which include fluid-structure interaction effects, we include his paper in Appendix C.

To demonstrate the application of this method of separability, we performed the following calculation using NASTRAN. A triangular impulse of strength 25.4 m/s^2 (1000 in/s^2) and duration 36 ms was placed at the vent exit in the 4T NASTRAN FSI model shown in Fig. 5-2. The spectral density of the resulting acceleration at the bottom-center of the flexible tank is shown in Fig. 5-3a. This corresponds to the lefthand illustration at the top of Fig. 5-1. Next, the same impulse was input to the 4T NASTRAN model where the walls were constrained to be rigid. This yielded the rigid wall pressure field p_i at the boundary, represented by the middle illustration in Fig. 5-1. This rigid wall pressure field was input to the same NASTRAN model without a source to obtain the flexible wall acceleration response as pictured in the righthand illustration in Fig. 5-1. The resulting spectral density of this acceleration is shown in Fig. 5-3b. The acceleration response spectra in Fig. 5-3 are identical, verifying the methodology and demonstrating its applicability to source strengths representative of any of the largest chugs in the 4T data base.

5.2 Solution of the Acoustic Equation with Flexible Boundaries

We have now established that the descriptions of fluid and structure motions are indeed separable. The description of fluid motion in either a cylindrical or annular geometry is given by the rigid wall solution of the acoustic equation in Chapter 4. To obtain the

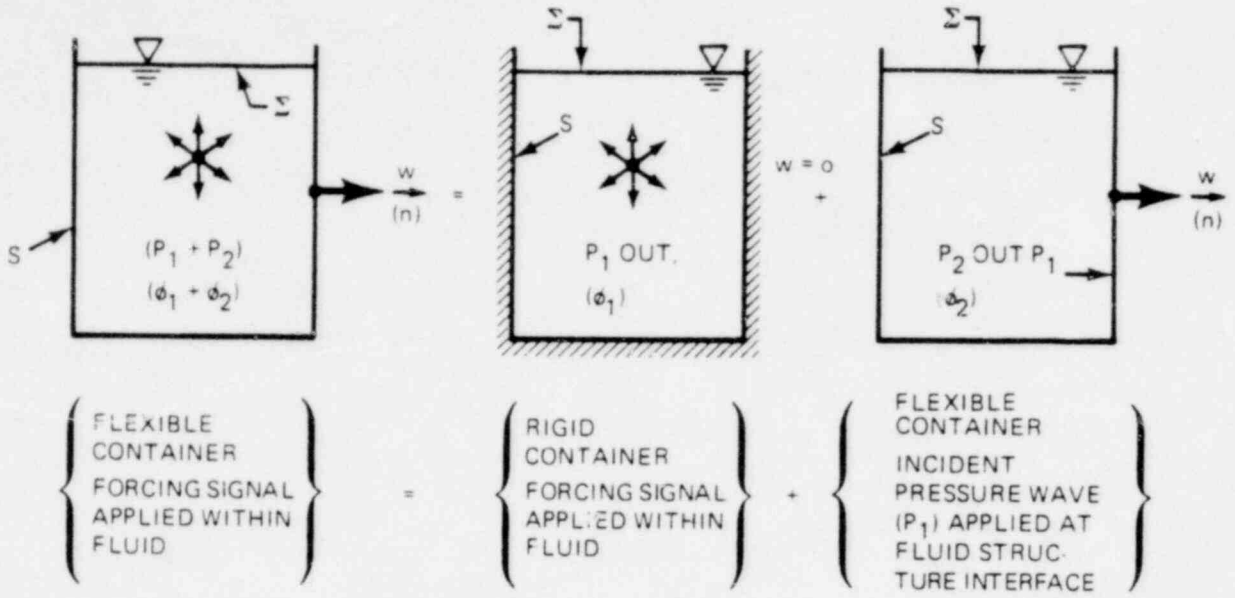

$$L^N(w) + M\ddot{w} = p_1 + p_2; \qquad w = 0; \qquad L^N(w) + M\ddot{w} = p_1 + p_2;$$

$$\nabla^2(\phi_1 + \phi_2) = \frac{1}{c^2}(\ddot{\phi}_1 + \ddot{\phi}_2); \qquad \nabla^2\phi_1 = \frac{1}{c^2}\ddot{\phi}_1; \qquad \nabla^2\phi_2 = \frac{1}{c^2}\ddot{\phi}_2;$$

$$(p_1 + p_2) = \rho(\dot{\phi}_1 + \dot{\phi}_2); \qquad p_1 = \rho\dot{\phi}_1; \qquad p_2 = \rho\dot{\phi}_2;$$

$$\frac{\partial}{\partial n}(\phi_1 + \phi_2)\Big]_S = \dot{w}; \qquad \frac{\partial\phi_1}{\partial n}\Big]_S = 0; \qquad \frac{\partial\phi_2}{\partial n}\Big]_S = \dot{w};$$

$$(p_1 + p_2)\Big]_\Sigma = 0; \qquad p_1\Big]_\Sigma = 0; \qquad p_2\Big]_\Sigma = 0.$$

Figure 5-1 Separability of Acoustic and Fluid Structure Interaction

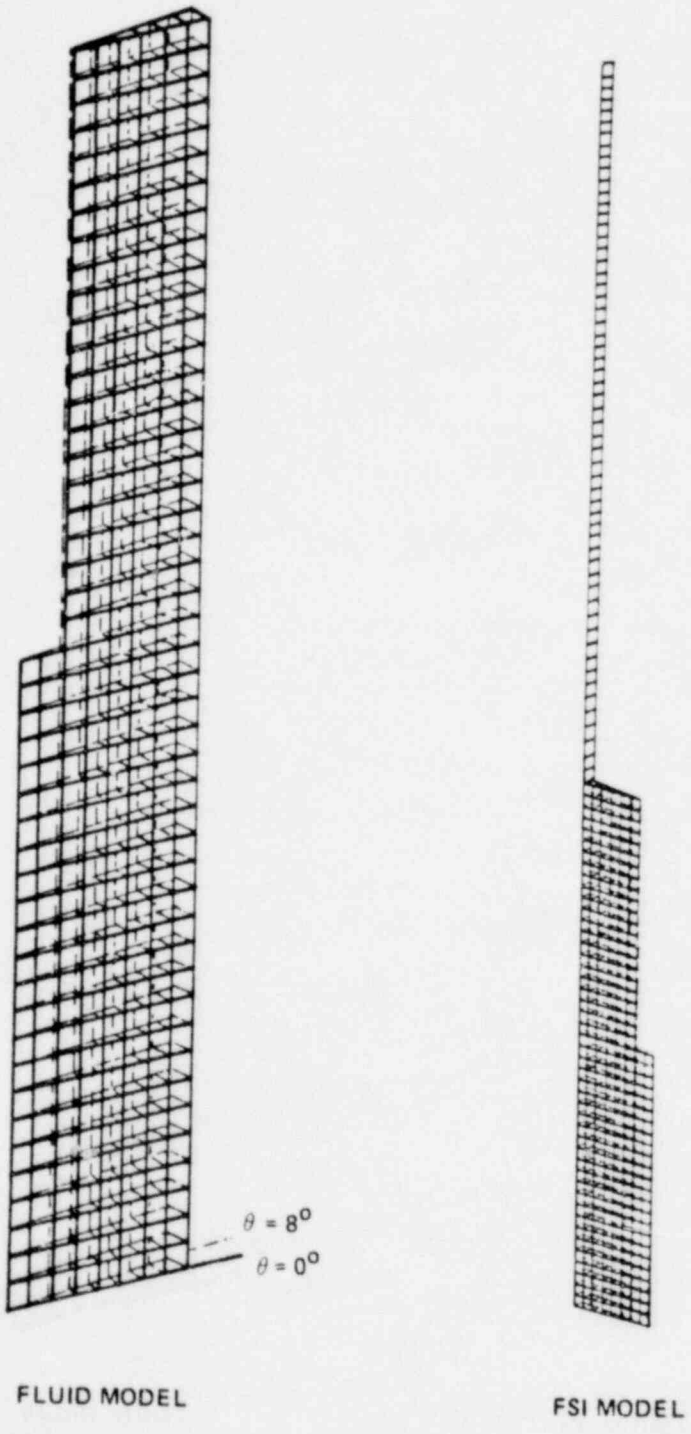

Figure 5-2 Nastran 4T FSI Model

G1002820-98

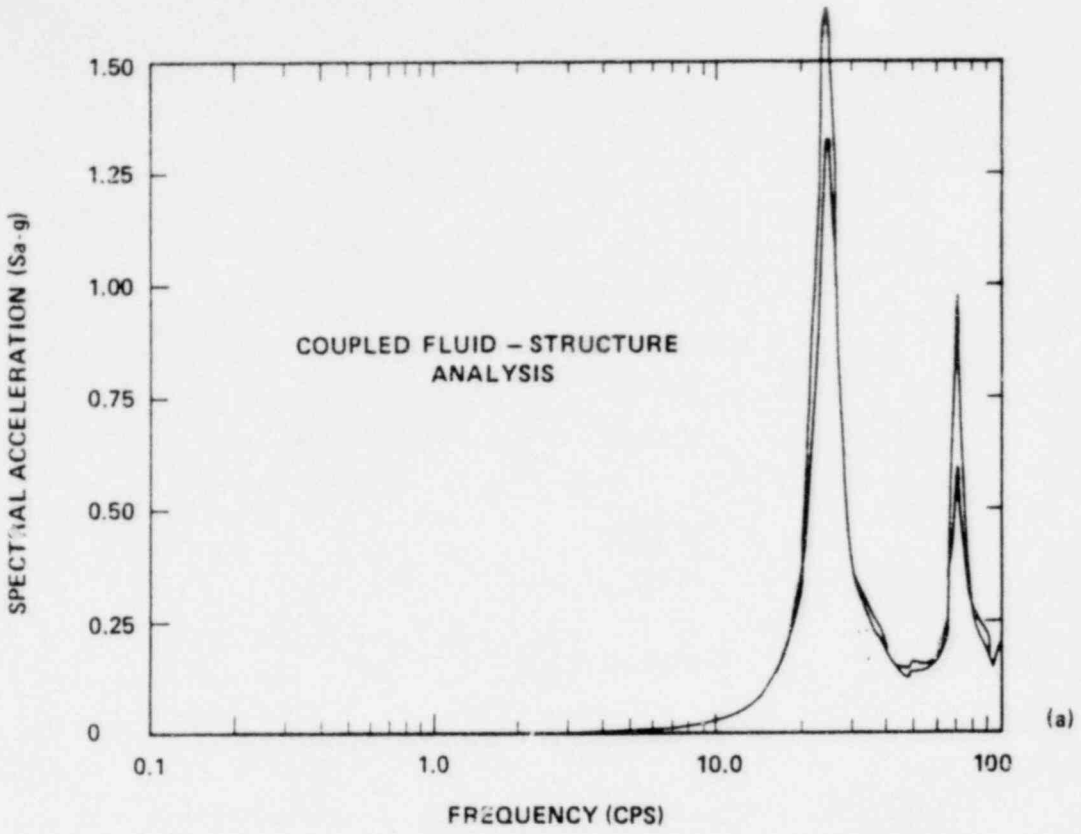

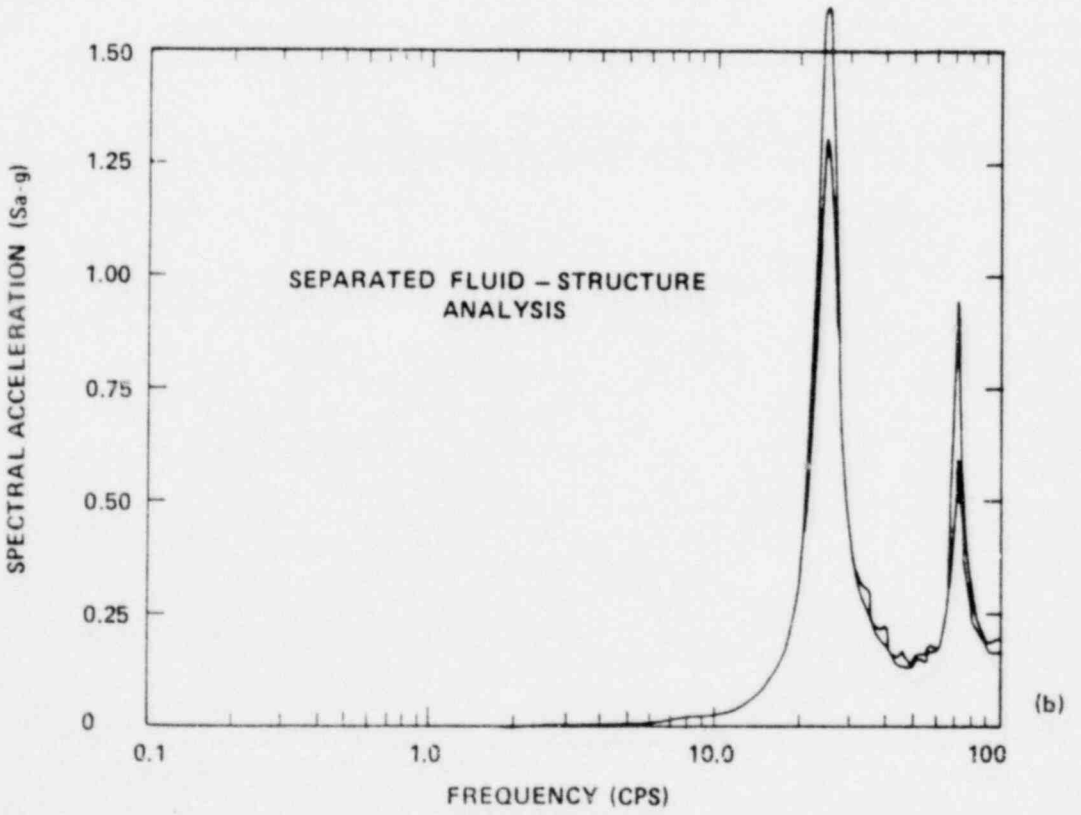

Figure 5-3 Acceleration Response Spectra at Bottom Dead Center

structural response, we must utilize a structural computer program with compressible fluid elements. Such computer programs are both complex and expensive to execute even though we have introduced a simplification via separability which makes the chugging problem tractable. We will now explore the feasibility of obtaining a flexible wall solution of the acoustic equation. Such a solution, if obtainable, would yield no small savings since it would then be possible to use a much simpler structural computer program such as ANSYS[34-36], without fluid, to determine containment response to chugging. Thus, for the same computer cost we could obtain a more extensive containment analysis.

Suppose the containment walls are locally reacting* so that to a good approximation we can assign a specific acoustic admittance $\beta(\omega,\vec{r}_s) = \xi - i\sigma = \rho c(u_n/p)$, where u_n is the normal velocity at the boundary, to each point $\vec{r}_s$ on the wall surface for each frequency $\omega/2\pi$. ξ and σ are the specific acoustic conductance and susceptance respectively. The acoustic response to a source can be expressed in terms of the normal modes of the fluid $\Psi(\omega,\vec{r})$ where, as before, Ψ_n are the eigenfunctions of the Helmholtz equation

$$\nabla^2 \Psi_n + K_n^2 \Psi_n = 0 \tag{5.3}$$

$$\int_V \Psi_n(\omega,\vec{r})\, \Psi_m(\omega,\vec{r})dV = V\Lambda_n(\omega)\delta_{mn} \,. \tag{5.4}$$

---

*The acoustic pressure acts on the surface of the structure and tends to make it move. If any fluid motion normal to the surface is possible, there will be wave motion in the material forming the surface. The motion of the surface at one point will be related to motion at another point of the surface by the wave motion inside the material as well as by the incident and reflected pressure waves. If the various parts of the surface are not strongly coupled together and we can consider that the motion, normal to the surface, of one portion of the surface is dependent only on the acoustic pressure incident on that portion and independent of the motion of any other part of the area, then we say that the surface is one of local reaction.

Ψ_n must satisfy the boundary condition that, for each point $\vec{r}_s$ on the boundary, the normal component of the gradient of Ψ_n in the outward-pointing direction is equal to $i(\omega/c)\beta(\omega,\vec{r}_s)$ times the value of Ψ_n at that point

$$\frac{\partial}{\partial n_s}\Psi_n(\omega,\vec{r}_s) = i(\frac{\omega}{c})\beta(\omega,\vec{r}_s)\,\Psi_n(\omega,\vec{r}_s) \quad . \tag{5.5}$$

The index n stands for a trio of quantum numbers, as required for a three-dimensional standing wave. If any portion of the boundary has a nonzero conductance ξ, the eigenvalues $K_n(\omega)$ will be complex with negative-imaginary parts. Suppose a root of the equation $cK_n(\omega) = \omega$ is $\omega_n - i\lambda_n$, with ω_n and λ_n positive quantities. Because of the symmetry of the admittance function $\beta(\omega,\vec{r}_s)$ about the imaginary ω axis, there will be another root at $-\omega_n - i\lambda_n$ so that the two roots of the equation $cK_n(\omega) = \omega$ are

$$\omega = \pm\omega_n - i\lambda_n = cK_n(\pm\omega_n - i\lambda_n), \tag{5.6}$$

with λ_n usually much smaller than ω_n.

As usual, the first task is to calculate the Green's function $G_\omega(\vec{r}|\vec{r}_o)$ representing the spatial distribution of the radiation from a point source of frequency $\omega/2\pi$ at a point $\vec{r}_o$. The Green's function satisfies

$$[\nabla^2 + (\frac{\omega}{c})^2]\,G_\omega(\vec{r}|\vec{r}_o) = -4\pi\delta(\vec{r}-\vec{r}_o) \quad . \tag{5.7}$$

Expanding G_ω in a series of the normal modes or eigenfunctions of the flexible wall, we can solve for the coefficients and obtain

$$G_\omega(\vec{r}|\vec{r}_o) = 4\pi \sum_n \frac{\Psi_n(\omega,\vec{r}_o)\Psi_n(\omega,\vec{r})}{V\Lambda_n[K_n^2(\omega)-(\frac{\omega}{c})^2]} \quad . \tag{5.8}$$

This then is the flexible wall Green's function.

Very close to the source, this series approaches the free-space Green's function $g_\omega = e^{ikR}/R$ where $R = |\vec{r}-\vec{r}_o|$; farther away, it differs from g_ω because of the waves reflected from the boundaries[37]. There will be a resonance when ω/c is equal to the real part of one of the eigenvalues $K_n(\omega)$. At the nth resonance the Ψ_n term predominates, having an amplitude inversely proportional to the imaginary part of $K_n(\omega)$ for that frequency.

The Fourier transform of Eq. (4.2) is

$$p_\omega(\vec{r}) = \int_V dV_o\, G_k(\vec{r}|\vec{r}_o) q_\omega(\vec{r}_o) + \frac{1}{4\pi} \oint_S d\vec{S}_o \cdot [G_k(\vec{r}|\vec{r}_o)\nabla_o p_\omega(\vec{r}_o) - p_\omega(\vec{r}_o)\nabla_o G_k(\vec{r}|\vec{r}_o)], \tag{5.9}$$

where p_ω and q_ω are the Fourier transforms of the pressure field and source distribution respectively and G_k is given by Eq. (4.6). Note that G_k is the Fourier transform of the Green's function defined by the wave equation (see Eq. (4.3)). Until subject to specific boundary conditions, G_k and thus Eq. (5.9) are completely general. If we specify flexible wall boundary conditions to be satisfied by the Green's function, then $G_k \equiv G_\omega$ and, using the definition of the specific acoustic admittance $\beta = \rho c(u_n/p)$ and Eq. (5.5), the Fourier transform of the flexible wall pressure field given by Eq. (5.9) becomes

$$p_\omega(\vec{r}) = \int_V dV_o G_\omega(\vec{r}|\vec{r}_o) q_\omega(\vec{r}_o). \tag{5.10}$$

Inspection of Eqs. (5.8) and (5.10) reveal that $p_\omega(\vec{r})$ is simply an expansion of the pressure field in terms of the flexible wall eigenfunctions $\Psi_n(\omega,\vec{r})$,

$$p_\omega(\vec{r}) = \sum_n a_n \Psi_n(\omega,\vec{r}) \tag{5.11}$$

where

$$a_n = \frac{4\pi}{V\Lambda_n[K_n^2(\omega)-(\frac{\omega}{c})^2]} \int \Psi_n(\omega,\vec{r}_o) q_\omega(\vec{r}_o) dV_o .$$

To compute $p_\omega(\vec{r})$, we must first determine the $\Psi_n(\omega,\vec{r})$. This we shall do using the eigenfunction $\phi_n(\vec{r})$ for the rigid wall containment. These eigenfunctions were obtained in Chapter 4 from the following equations:

$$(\nabla^2 + \eta_n^2)\ \phi_n(\vec{r}) = 0, \tag{5.12}$$

$$\frac{\partial}{\partial n}\ \phi_n(\vec{r}_s) = 0, \tag{5.13}$$

where $\vec{r}_s$ is a point on the rigid wall and $c\eta_n \equiv \omega_n^o$ the rigid wall eigenfrequency. Note the slight change in notation for the rigid wall eigenvalue η_n. The rigid wall eigenfunctions were normalized according to

$$\int \phi_m(\vec{r})\phi_n(\vec{r})dV = V\Lambda_n^o\ \delta_{mn}. \tag{5.14}$$

The most direct way of determining changes in the eigenfunctions and eigenvalues produced when the boundary surface S is no longer rigid is by use of a Green's function of the general form of Eq. (5.8) but for rigid walls. We wish to use this Green's function to obtain a set of solutions of Eqs. (5.3) and (5.4) for a frequency $\omega/2\pi \equiv ck/2\pi \equiv cK_N/2\pi$ where K_N is a flexible wall eigenvalue. The defining equation for the Green's function is therefore

$$(\nabla^2 + K_N^2)G_K(\vec{r}|\vec{r}_o) = -\ 4\pi\delta(\vec{r}-\vec{r}_o) \tag{5.15}$$

subject to the boundary condition

$$\frac{\partial}{\partial n}\ G_K(\vec{r}_s|\vec{r}_o) = 0\ . \tag{5.16}$$

Expressing this Green's function in terms of the eigenfunctions $\phi_n(\vec{r})$, we find that

$$G_K(\vec{r}|\vec{r}_o) = 4\pi \sum_n \frac{\Phi_n(\vec{r}_o)\Phi_n(\vec{r})}{V\Lambda_n^o(\eta_n^2 - K_N^2)} \quad . \tag{5.17}$$

The equation for the flexible wall pressure field p_ω in terms of this rigid wall Greens function G_K is obtained from Eq. (5.9) by setting $G_k = G_K$ and utilizing Eq. (5.16).

$$p_\omega(\vec{r}) = \int_V dV_o \; G_K(\vec{r}|\vec{r}_o) q_\omega(\vec{r}_o) + \frac{1}{4\pi} \oint_S d\vec{S}_o \cdot G_K(\vec{r}|\vec{r}_o) \nabla_o p_\omega(\vec{r}_o). \tag{5.18}$$

The first term on the right is the rigid wall pressure response to a source q_ω and designated p_1 in Fig. 5-1 and Appendix C. The second term is the pressure field due to fluid-structure interaction and designated p_2. Since we are primarily interested in the fluid-structure interaction pressure field p_2, we shall omit the source q_ω in the following development. Once the flexible wall eigenfunctions Ψ_n have been determined, the effects of the source q_ω can be determined via Eq. (5.10). Thus, for the present the volume integral does not occur and Eq. (5.18) reduces to

$$p_\omega(\vec{r}) = \frac{1}{4\pi} \oint G_K(\vec{r}|\vec{r}_o) \frac{\partial p_\omega}{\partial n_o} dS_o = \frac{ik}{4\pi} \oint G_K(\vec{r}|\vec{r}_o) \beta(\omega,\vec{r}_o) p_\omega(\vec{r}_o) dS_o, \tag{5.19}$$

where the boundary conditions which p_ω must satisfy have been introduced. Since in Eq. (5.11) $p_\omega(\vec{r})$ is expressible in a series of flexible wall eigenfunctions $\Psi_n(\omega,\vec{r})$, Eq. (5.19) can be transformed into

$$\Psi_N(\omega,\vec{r}) = \frac{ik}{4\pi} \oint G_K(\vec{r}|\vec{r}_o) \beta(\omega,\vec{r}_o) \Psi_N(\omega,\vec{r}_o) dS_o \tag{5.20}$$

for a particular vibrational mode N. This is a homogeneous integral equation, which includes both the differential equation and the boundary conditions which Ψ_N must satisfy. Its exact solution yields the correct form for the eigenfunction Ψ_N and also the correct value of the corresponding eigenvalue K_N. Unless K_N has this value, the only possible solution of Eq. (5.20) is $\Psi_N = 0$ everywhere.

The general properties of this equation and its solution can be more clearly demonstrated by a modification of its form. We separate out the term n = N in the series for G_K and write Eq. (5.20) as

$$\Psi_N(\omega,\vec{r}) = ik\left[\frac{\oint \phi_N(\vec{r}_s)\beta(\omega,\vec{r}_s)\Psi_N(\omega,\vec{r}_s)dS}{V\Lambda_N^o(\eta_N^2 - K_N^2)} \right] \phi_N(\vec{r}) + \frac{ik}{4\pi} \oint G_N(\vec{r}|\vec{r}_s)\beta(\omega,\vec{r}_s)\Psi_N(\omega,\vec{r}_s)dS, \tag{5.21}$$

where

$$G_N(\vec{r}|\vec{r}_o) = 4\pi \sum_{n\neq N} \frac{\phi_n(\vec{r}_o)\phi_n(\vec{r})}{V\Lambda_N^o(\eta_n^2 - K_N^2)} \tag{5.22}$$

and, as before, $\vec{r}_s$ is a point on the boundary.

The equation is homogeneous so Ψ_N can be multiplied by any constant factor and still be a solution. For convenience, we choose that factor which allows the expression in square brackets to be equal to 1/ik. Thus,

$$\oint \phi_N(\vec{r}_s)\beta(\omega,\vec{r}_s)\Psi_N(\omega,\vec{r}_s)dS = \frac{V\Lambda_N^o}{ik}(\eta_N^2 - K_N^2) \tag{5.23}$$

and

$$\Psi_N(\omega,\vec{r}) = \phi_N(\vec{r}) + \frac{ik}{4\pi} \oint G_N(\vec{r}|\vec{r}_s)\beta(\omega,\vec{r}_s)\Psi_N(\omega,\vec{r}_s)dS. \tag{5.24}$$

If β is small, Eq. (5.24) can be solved approximately by expansion in a perturbation series[38,39] to any order desired. A first-order approximation solution yields

$$\Psi_N(\omega,\vec{r}) \cong \phi_N(\vec{r}) + \frac{ik}{4\pi} \oint G_N(\vec{r}|\vec{r}_s)\beta(\omega,\vec{r}_s)\phi_N(\vec{r}_s)dS \tag{5.25}$$

and

$$K_N^2(\omega) \cong \eta_N^2 - \frac{ik}{V\Lambda_N^o} \oint \phi_N^2(\vec{r}_s)\beta(\omega,\vec{r}_s)dS\,. \tag{5.26}$$

The resonance frequency ω_N and damping λ_N for free vibration of the Nth standing wave are obtained by solving Eq. (5.6) using the $K_N(\omega)$ of Eq. (5.26). To first order, therefore

$$\omega_N^2 - \lambda_N^2 \cong (\omega_N^o)^2 - \frac{c}{V\Lambda_N^o} \oint \phi_N^2(\vec{r}_s)[\omega_N\sigma(\omega,\vec{r}_s) + \lambda_N\xi(\omega,\vec{r}_s)]dS \tag{5.27}$$

$$\lambda_N \cong \frac{c}{2V\Lambda_N^o} \oint \phi_N^2[\xi(\omega,\vec{r}_s) - \frac{\lambda_N}{\omega_N}\sigma(\omega,\vec{r}_s)]dS \tag{5.28}$$

if we assume that the locally reactive boundary (see footnote, page 5-6) behaves as a simple-harmonic oscillator. The acoustic impedance $z(\omega)$ for a simple-harmonic oscillator is given by[40]

$$z(\omega) = \rho c/\beta(\omega) = R + iM(\frac{\omega_s^2}{\omega} - \omega) \tag{5.29}$$

where $M = \rho_s h$ is the effective mass per unit area and h is the boundary thickness, $R = 2\zeta_s M\omega_s$ is the mechanical resistance of the boundary, and $M\omega_s^2$ is the effective boundary stiffness. We define a spatial average acoustic admittance $\bar{\beta}(\omega)$ via

$$\bar{\beta}(\omega) \oint \phi_N^2(\vec{r}_s)dS \equiv \oint \phi_N^2(\vec{r}_s)\beta(\omega,\vec{r}_s)\,dS. \tag{5.30}$$

Since $\bar{\beta}(\omega) \equiv \bar{\xi}(\omega) - i\bar{\sigma}(\omega)$, the spatial average conductance $\bar{\xi}(\omega)$ and susceptance $\bar{\sigma}(\omega)$ also have identical definitions. We can obtain the spatial average admittance for locally reactive boundaries from Eq. (5.29) by replacing ω which is complex with $\omega_N - i\lambda_N$. For stiff walls where

$$\omega_s^2 >> \omega_N^2 >> \lambda_N^2 , \tag{5.31}$$

$\bar{\beta}(\omega)$ reduces to

$$\beta(\omega) \cong (\frac{\rho c}{\rho_s h})[2\zeta_s \frac{\omega_N^2}{\omega_s^3} - \frac{\lambda_N}{\omega_s^2} - i \frac{\omega_N}{\omega_s^2}]. \tag{5.32}$$

The conductance and susceptance are then equal to

$$\bar{\xi}(\omega) \cong (\frac{\rho c}{\rho_s h})[2\zeta_s \frac{\omega_N^2}{\omega_s^3} - \frac{\lambda_N}{\omega_s^2}] \tag{5.33}$$

and

$$\bar{\sigma}(\omega) \cong (\frac{\rho c}{\rho_s h}) \frac{\omega_N}{\omega_s^2} . \tag{5.34}$$

Hence, to first order, the eigenfrequency ω_N and damping factor λ_N become

$$\omega_N \cong \omega_N^o [1 + 2 \frac{\rho c^2 I}{\rho_s h \omega_s^2}]^{-1/2} \tag{5.35}$$

and

$$\lambda_N \cong 2\zeta_s (\frac{\rho c^2 I}{\rho_s h \omega_s^2})(\frac{\omega_N}{\omega_s})[1 + 2 \frac{\rho c^2 I}{\rho_s h \omega_s^2}]^{-1} \tag{5.36}$$

where we have set

$$\oint \phi_N^2 (\vec{r}_s) dS = 2V\Lambda_N^o I \tag{5.37}$$

for simplicity. We note that for a cylindrical geometry $I = (1/L + 1/a)$.

We see that the rigid wall eigenfrequencies ω_N^o are shifted by a constant amount independent of frequency. The rigid wall fundamental frequency (N = 0) in both 4T and Mark II is given by $\omega_o^o = \pi c/2L$. If we define $\omega_o \equiv \pi c'/2L$, then Eq. (5.36) is tantamount to an apparent reduction in the sonic speed, namely

$$c' = c \left[1 + 2 \frac{\rho c^2 I}{\rho_s h \omega_s^2}\right]^{-1/2} . \tag{5.38}$$

That such a reduction exists for acoustic signals traveling in flexible wall enclosures is well known[41-45] and is discussed in Appendix B. As a matter of fact, we can quite accurately compute this reduction in 4T based on agreement between observed and calculated fundamental frequencies as shown in Chapter 2. This is based on the effective increase in fluid compressibility due to the volume flexibility per unit volume δ of the containment[44] and the relationship between sonic speed and compressibility

$$\frac{1}{\rho c'^2} = \frac{1}{\rho c^2} + \delta. \tag{5.39}$$

We see that, to a first approximation, the change in the eigenfrequency and the occurence of damping is due to $\beta \neq 0$. This shift in eigenfrequency $\omega_N - \omega_N^o$ and the value of the damping constant λ_N is proportional to the average value of σ and ζ over the boundary surface weighted by ϕ_N^2 so that those parts of the surface where the Nth standing wave is large are emphasized. The effectiveness of the flexible walls in coupling other normal modes to the Nth one is measured by the magnitudes of the integrals $\oint \phi_n \beta \phi_N dS$ entering $\oint G_N \beta \phi_N dS$ in the expression for Ψ_N in Eq. (5.25). If β is nearly uniform, most of the integrals $\oint \phi_n \beta \phi_N dS (n \neq N)$ will be quite small and Ψ_N will not differ much from the rigid wall eigenfunction ϕ_N.

We have thus succeeded in obtaining a solution to the acoustic wave equation with flexible boundaries in terms of the specific acoustic admittance $\beta(\omega,\vec{r}_s)$. If the functional dependence of $\beta(\omega,\vec{r}_s)$ on frequency $\omega/2\pi$ and wall location $\vec{r}_s$ is known, we can completely determine the total pressure field which includes the effects of the fluid-structure interaction. The structural response would then be calculated using a structural model without the fluid ("dry containment") and applying the total pressure field to the boundary. All that is required is that $\beta(\omega,\vec{r}_s)$ be small to permit a perturbation series expansion of Eq. (5.25). This is not an unreasonable expectation for containments with fairly rigid boundaries. In summary, we see that[46,47] the fluid-structure interaction effects are threefold:

(1) Mixing of the rigid wall normal modes as shown by Eqs. (5.25) and (5.26),

(2) A reduction in the rigid wall eigenfrequencies ω_N^o shown by Eqs. (5.27) and (5.35), and

(3) Damping of the free vibrations of the standing waves as given by Eq. (5.36).

It is noteworthy to mention that this method of describing the response of a fluid in a cavity with flexible walls to a source or sources, which has been called chugging in the Mark II program, is that which has been used successfully by physicists and engineers active in the field of acoustics for over three decades[48].

To verify that the acoustic fluid-structure interaction methodology correctly gives the flexible wall eigenfrequency ω_N, we shall compare the fundamental eigenfrequency ω_o as computed from Eq. (5.35) with that computed by other methods and with experimental results.

We have already made the reasonable assumption that $\beta(\omega,\vec{r}_s)$ was small enough to permit a first-order perturbation solution of Eq. (5.24). We further assume that $\beta(\omega,\vec{r}_s)$ is sufficiently uniform over the

boundary, resulting in no appreciable coupling of the rigid wall normal modes $\phi_N(\vec{r})$ such that, to a good approximation,

$$\Psi_N(\omega,\vec{r}) \cong \phi_N(\vec{r}). \tag{5.40}$$

We shall begin with the 4T using the nominal structure and fluid properties given in Table 5-1. We assume the 4T to be structurally composed of two parts: a steel cylindrical shell of thickness h_s and a base plate of thickness h_b. From a structural point of view, this is an extreme simplification, but for our purposes it will suffice as we shall demonstrate. The surface integral in Eq. (5.27) is to be evaluated over the shell and base plate resulting in the following modification to Eq. (5.35).

$$\omega_N \cong \omega_N^o \left[1 + 2\,\frac{\rho c^2}{\rho_s}\,\left(\frac{1/L}{h_b\omega_b^2} + \frac{1/a}{h_s\omega_s^2}\right)\right]^{-1/2} \tag{5.41}$$

The fundamental flexible wall eigenfrequency $\omega_o/2\pi$ computed by the above is 26.9 Hz where the rigid wall eigenfrequency $\omega_o^o/2\pi$ = 36.9 Hz.

We can also compute $\omega_o/2\pi$ using the method described in Appendix B. First, the acoustic speed is reduced from its nominal value by the distensibility of the 4T shell. The effective acoustic speed is obtained using Eq. (B.8) and the values in Table 5-1. The effect of the base plate is calculated from Eq. (B.18) using this value for c. The fundamental flexible wall eigenfrequency turns out to be $\omega_o/2\pi$ = 26.8 Hz.

Finally, we examine the results of a NASTRAN calculation for an impulsive source given in Fig. 5-3a. The eigenfrequency $\omega_o/2\pi$ as calculated by NASTRAN is 23.8 $\pm$ 0.1 Hz. The 4T NASTRAN model had a "simply supported" base plate; thus, Eq. (5.41) gives $\omega_o/2\pi$ = 23.2 Hz.

The experimental results against which we wish to compare are the Anamet 4T bell jar and impact tests[5]. The average fundamental

Table 5-1

NOMINAL 4T STRUCTURE AND FLUID PROPERTIES USED IN THE VERIFICATION OF THE ACOUSTIC FLUID-STRUCTURE INTERACTION METHODOLOGY

a = 1.0668 m (3.5 ft) = tank radius

L = 7.0104 m (23 ft) = nominal water depth

= 6.2484 m (20.5 ft) = water depth for Anamet test

h_b = 101.6 mm (4 in) = base plate thickness

h_s = 15.875 mm (5/8 in) = shell thickness

ω_b = 1185.6 S^{-1} = base plate vibrational frequency *

= 1373.6 S^{-1} **

= 674.1 S^{-1} ***

ω_s = 4913.8 S^{-1} = shell vibration frequency

ρ_s = 7700 kgm^{-3} (470.7 lbm ft^{-3}) = steel density

Y = 19.5 (10^{10}) Pa (28.3 Mpsi) = steel elastic modulus

μ = 0.28 = Poisson's ratio for steel

ρ = 1000 kgm^{-3} (62.4 lbm ft^{-3}) = water density

c = 1036 m/s (3400 fps) = acoustic speed

* Observed in Anamet 4T FSI study

** $\omega_b = \frac{1}{a}\left[\frac{Y}{\rho_s}(1-\mu^2)^{-1}\right]^{1/2}$ (clamped plate)

*** $\omega_b = (4.99)\frac{h_b}{a^2}\left[\frac{Y}{12\rho_s}(1-\mu^2)^{-1}\right]^{1/2}$ (simply supported plate)

eigenfrequency for these tests was $\omega_o/2\pi = 33.4 \pm 1.6$ Hz. We assume an acoustic speed of 1478 m/s (4849 fps) corresponding to an assumed water temperature of 18.3°C (65°F) and overpressure of 101.325 kPa (14.7 psi). The average water depth was 6.2484 m (20.5 ft) Hz. Using the observed value for ω_b given in Table 5-1, Eq. (5.41) gives $\omega_o/2\pi$ = 34.0 Hz.

We shall next examine how accurately the acoustic fluid-structure interaction methodology determines the flexible wall eigenfrequency ω_o in a Mark II suppression pool. Because of the complex nature of the Mark II suppression pool boundary, it is not as straightforward to determine the spatial average acoustic admittance $\bar{\beta}(\omega)$ as for 4T. If we instead use the distensibility δ for the Mark II, the correction factor to the rigid wall eigenfrequency $\omega_N^o/2\pi$ can be obtained by equating Eqs. (5.38) and (5.39)

$$\delta = \frac{2I}{\rho_s h \omega_s^2} \quad . \tag{5.42}$$

The flexible wall eigenfrequency $\omega_o/2\pi$ is then given by Eq. (5.41) as before. To verify this method for Mark II, we again use NASTRAN. The NASTRAN model of the Limerick-Susquehanna containment used is shown in Fig. 5-4. The volume flexibility $V\delta$, which is defined as the increase in containment volume per unit of applied pressure, was determined to be $V\delta = 1.061(10^{-3})$ m^3/kPa (0.252 ft^3/psi). It was computed from the Mark II boundary pressures resulting from an actuation of the safety relief valves (SRV). This boundary pressure has its principal frequency in the range 7 through 12 Hz. This value for $V\delta$ is the sum of separate volume flexibilities for the basemat, wall, and pedestal. From Table 4-1, the volume of water is computed to be $V = 3504.8$ m^3. Thus, $\delta = 302.7(10^{-12})$ m^2/N (2.09×10^{-6}/psi). We input the water density ρ and sonic speed c to the NASTRAN model as 1000 kg/m^3 and 1036 m/s. The computed rigid wall fundamental frequency for the same triangular impulse used before was $\omega_o^o/2\pi$ = 37 Hz

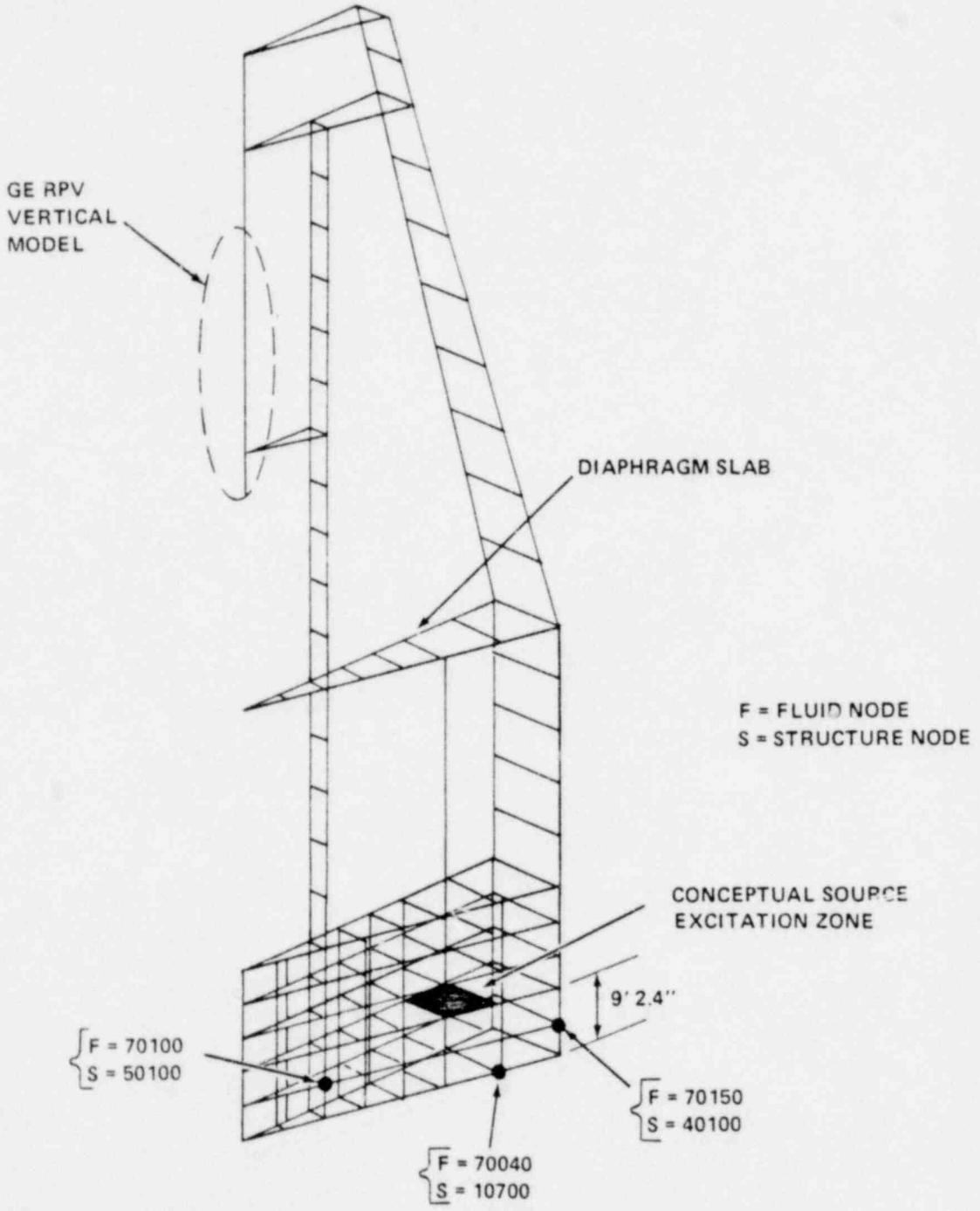

Figure 5-4 Mark II Soil-Interacted Fluid-Interacted RPV-Associated Containment NASTRAN Model

as shown in Fig. 5-5, while for flexible walls it was $\omega_o/2\pi$ = 32 Hz as shown in Fig. 5-6. Using Eq. (5.36) we find that $\omega_o/2\pi$ = 32.1 Hz, which compares quite well with 32 Hz.

Thus, we conclude from these comparisons that the flexible wall solution of the acoustic wave equation is capable of predicting the eigenfrequency ω_o to within 3%.

We need now to determine either the specific acoustic conductance or, equivalently, the damping constant[48-51] λ_N. Unfortunately, here we have no theory to guide us[52], but experience suggests[53] that the value of the fluid damping factor $\zeta = \lambda_N/\omega_N$ for a welded steel structure such as 4T of 0.045 is reasonable. Indeed this is about the value obtained from the 4T Category I chugs. For the Mark II containment, the value of ζ which will be used is set by regulatory guide[54].

What now remains is to verify the assumption that $\beta(\omega,\vec{r}_s)$ is sufficiently uniform that $\phi_N(\vec{r})$ is a good approximation to $\Psi_N(\omega,\vec{r})$ for the Nth vibrational mode. This we shall do by comparing the mode shape of the pressure response obtained during the Anamet tests with that computed by the flexible wall acoustic theory. This comparison can easily be effected using the 4T acoustic transfer function H_ω. The defining equation for H_ω is

$$p_\omega(\vec{r}) = H_\omega(\vec{r}|\vec{r}_o)S_\omega(\vec{r}_o). \tag{5.43}$$

The transfer function $H_\omega(\vec{r}|\vec{r}_o)$ is given by

$$H_\omega(\vec{r}|\vec{r}_o) = 4\pi c^2\rho \sum_N \Psi_N(\vec{r})\Psi_N(\vec{r}_o)[(\omega_N^2 + \lambda_N^2 - \omega^2)^2 - 4\omega^2\lambda_N^2]^{-1/2}\, e^{i\phi_N} \tag{5.44}$$

and

$$\phi_N = \tan^{-1}[2\omega\lambda_N(\omega_N^2 + \lambda_N^2 - \omega^2)^{-1}] \tag{5.45}$$

where $\Psi_N(\omega,\vec{r}) \cong \Psi_N(\vec{r})$ as we shall demonstrate.

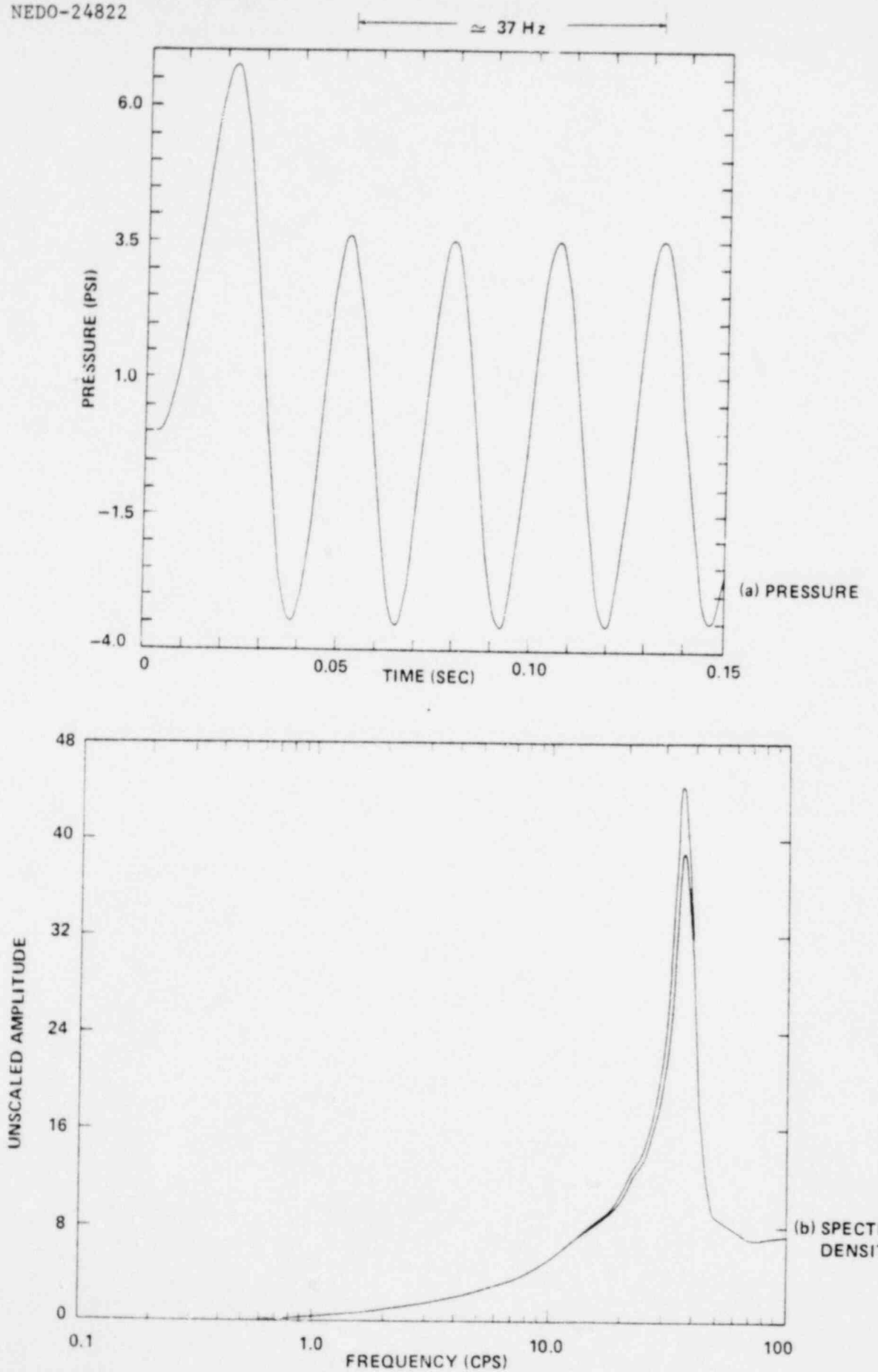

Figure 5-5 Mark II Rigid Wall Pressure and Spectral Density at Basemat

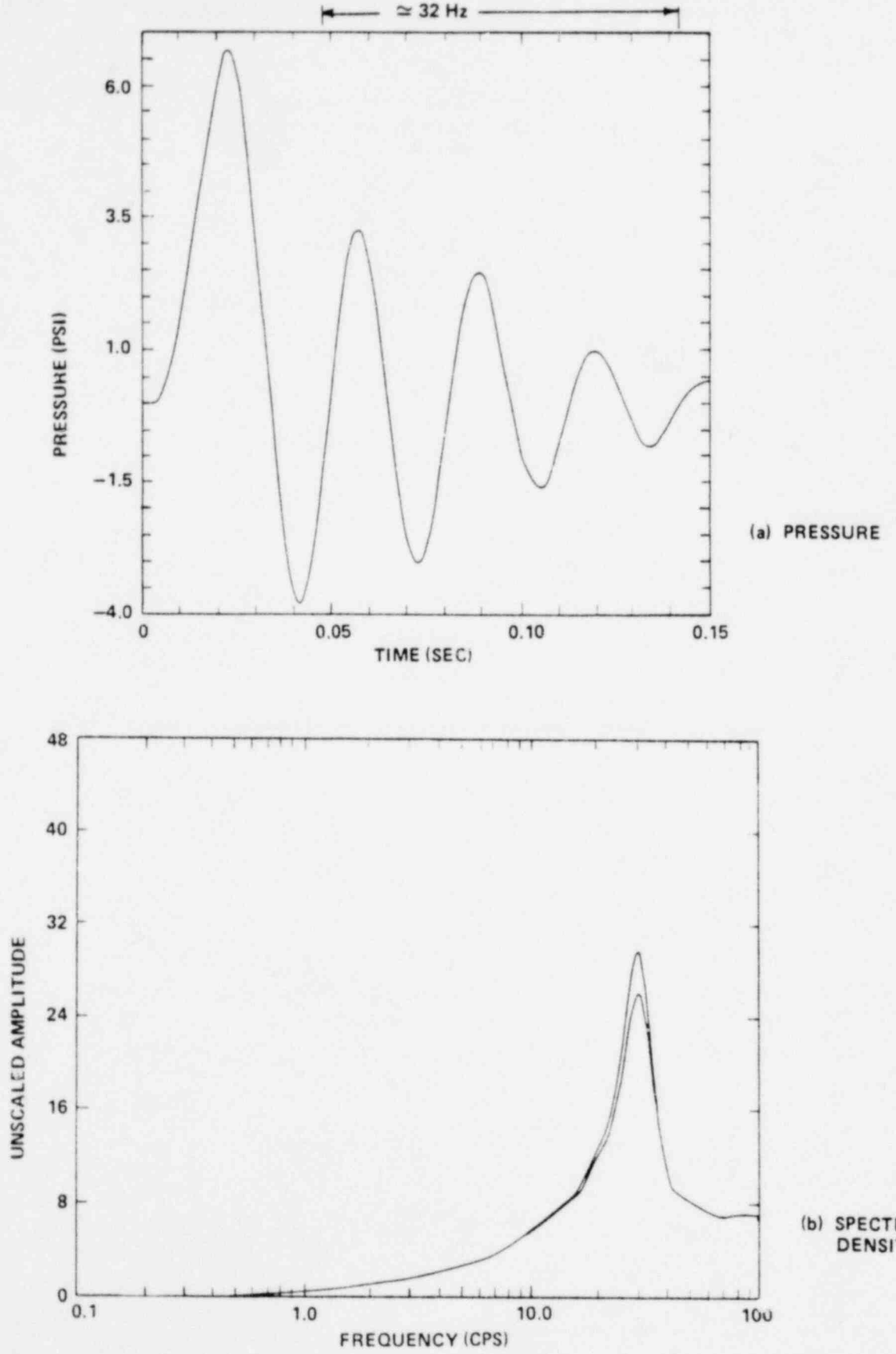

Figure 5-6 Mark II Flexible Wall Pressure and Spectral Density at Basemat

Upon inspection of Eq. (5.17), it is immediately obvious that $H_\omega(\vec{r}|\vec{r}_o) = \rho G_K(\vec{r}|\vec{r}_o)$ for the case when $\Psi_N = \phi_N$. To demonstrate the effect of fluid-structure interaction, we compare $H_\omega(\vec{r}|\vec{r}_o)$ in Fig. 5-7 for both a rigid wall and flexible wall 4T.

The flexible wall case corresponds to a sonic speed c = 701 m/s and a fluid damping factor $\zeta = 0.045$. Note that an effect of wall flexibility is to <u>increase</u> the spectral density of the pressure in some frequency ranges. We also see that the 4T responds ("rings out") primarily in the fundamental mode N = 0 for an impulsive source. Thus, under our assumption that $\beta(\omega,\vec{r}_s)$ is uniform, the fundamental mode is described by $\Psi_o(\vec{r}) \cong \phi_o(\vec{r})$ and depends on z as $\cos(\pi z/2L)$ as is seen from Eq. (4.12). The comparison between the mode shape obtained from the Anamet test results and $\cos(\pi z/2L)$ is shown in Fig. 5-8.

We have thus been able to solve the acoustic wave equation in geometries of interest with flexible walls. That we were able to do so was, in principle, not in question. What is significant, however, is that these solutions are no more complex than the rigid wall solutions provided certain assumptions hold. These assumptions circumscribe the fluid-structure interaction which is described by the specific acoustic admittance $\beta(\omega,\vec{r}_s)$ or, equivalently, by δ and ζ. Specifically:

(1) $\beta(\omega,\vec{r}_s)$ must be sufficiently small such that Eq. (5.25) is valid,

(2) $\beta(\omega,\vec{r}_s)$ must be sufficiently uniform such that the surface integral of Eq. (5.25) may be neglected so that $\Psi_N(\vec{r}) \cong \phi_N(\vec{r})$,

(3) The boundary must be locally reactive with an acoustic impedance $z(\omega)$ given by Eq. (5.29).

Hence, we are able to compute the <u>total</u> flexible wall pressure field $p = p_1 + p_2$ (Fig. 5-1) via Eq. (5.10) where the Green's function G_ω becomes[55]

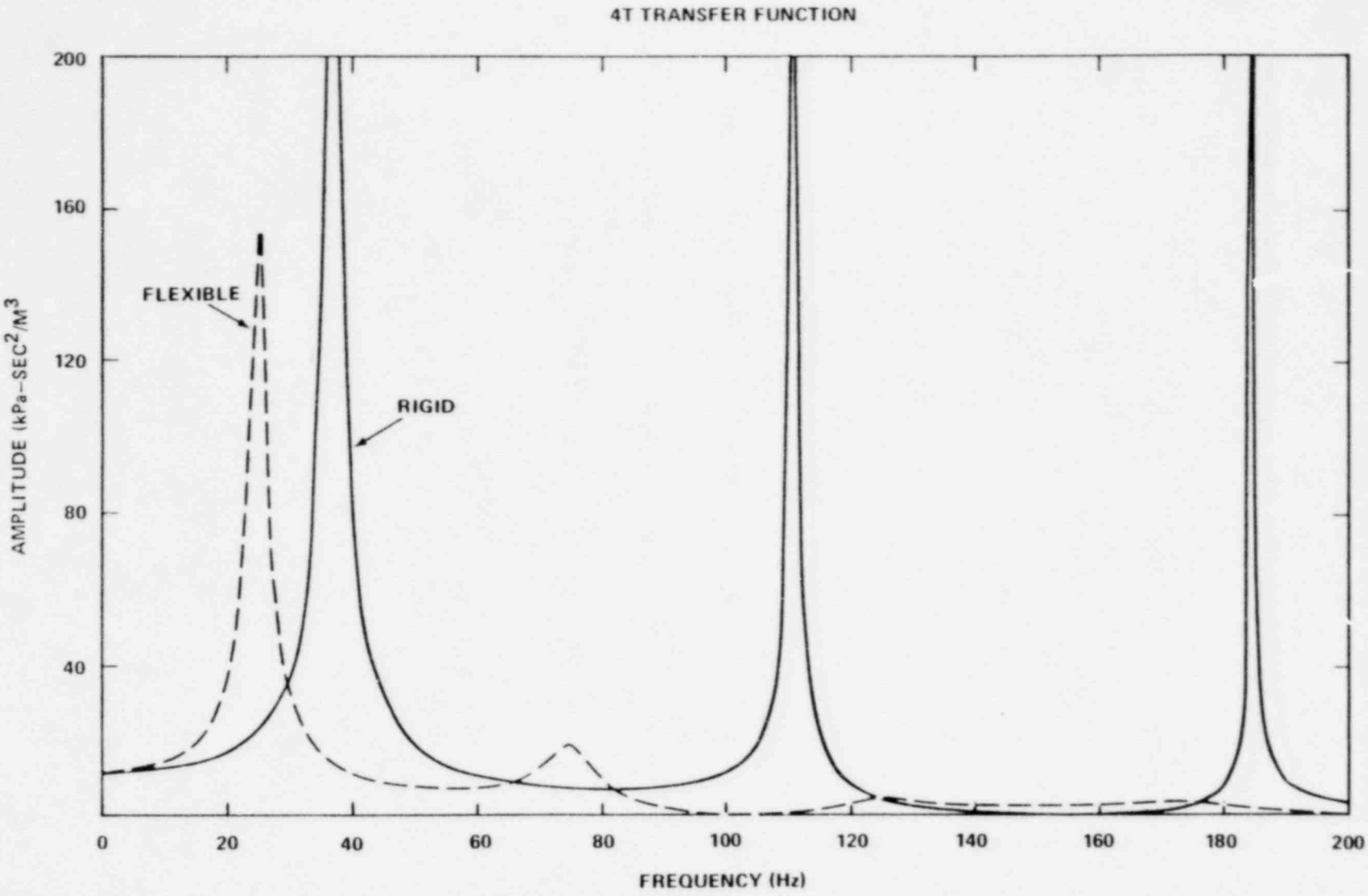

Figure 5-7 Transfer Function $\left|H_{\omega}(\bar{r}|\bar{r}_o)\right|^2$ at Bottom-Center in 4T

Figure 5-8 Normalized Mode Shape for 30 HZ as Estimated from Anamet Blttle Test No. 1 as a Function of Elevation (GENERAL ELECTRIC COMPANY PROPRIETARY)

$$G_\omega(\vec{r}|\vec{r}_o) = 4\pi c^2 \sum_n \frac{\phi_n(\vec{r}_o)\,\phi_n(\vec{r})}{V\Lambda_n[\omega_n^2 - (\omega+i\lambda_n)^2]} \quad (5.46)$$

The rigid wall eigenfunctions ϕ_n are given by Eq. (4.12) for 4T or by Eq. (4.27) for Mark II. The flexible wall eigenfrequencies ω_n are calculated from either Eq. (4.20) for 4T or Eq. (4.36) for Mark II where the speed of sound used is that given by Eq. (5.40). The damping constant $\lambda_n = \zeta\omega_n$ is obtained either by experiment, from a regulatory guide, or from a NASTRAN calculation.

Essentially, we have reduced the description of the fluid-structure interaction to the parameters δ and ζ controlling the frequency shift and damping respectively. We have already demonstrated that δ adequately describes the speed of sound and thus the eigenfrequency both in 4T and Mark II via Eq. (5.40). However, to provide further verification of this method of treating fluid-structure interaction without considering the structure per se, we again compare the predictions of flexible wall acoustic theory with the results of a flexible wall NASTRAN calculation for our 4T model. Both IWEGS and NASTRAN used essentially the same chug source shown in Table 5-2, which is a variant of the design source. For use in the NASTRAN computer program, however, the source had to be converted from a volume acceleration to a linear acceleration. This conversion was accomplished by a multiplication constant which was obtained by requiring the peak pressures calculated by IWEGS and NASTRAN to agree in a rigid wall 4T. The speed of sound was chosen to be c = 1036 m/s (3400 fps). For IWEGS, the effective speed of sound used to account for shift in eigenfrequency is c' = 650 m/s (2131 fps) and is computed from Eq. (5.41) in the same manner that Eq. (5.38) was obtained from Eq. (5.35), viz:

$$c = c'\left[1 + 2\frac{\rho c^2}{\rho_s}\left(\frac{1/L}{h_b\omega_b^2} + \frac{1/a}{h_s\omega_s^2}\right)\right]^{-1/2} . \quad (5.47)$$

Table 5-2

CHUGGING SOURCE PARAMETERS (GE125) USED IN COMPARISON OF IWEGS AND NASTRAN IN 4T

$$S(t) = - A_o \Lambda\left(\frac{2t}{\tau} - 1\right) + \sum_{i=1} A_i \sin(\omega_i t)$$

i	A_i (m^3/s^2)*	$\omega_i/2\pi$ (H_z)
0	5.2	(τ = 36 ms)
1	0.73	5.0
2	0.43	12.6
3	0.13	20.9
4	0.10	28.7
5	0.23	39.1
6	0.48	45.6
7	1.30	56.1
8	0.29	63.9

* To convert the source strengths A_i which are in terms of volume accelerations (m^3/s^2) to linear accelerations (in/s^2) suitable for NASTRAN $A_i \rightarrow (16760)A_i$

Values for the various constants are found in Table 5-1. Since the NASTRAN model treats the base plate as simply supported, we set $\omega_b = 647.1\ S^{-1}$. NASTRAN used a structural damping of 0.045 which was manifest as a fluid damping factor of $\zeta = 0.03$. The comparison of the IWEGS and NASTRAN results are shown in Fig. 5-9.

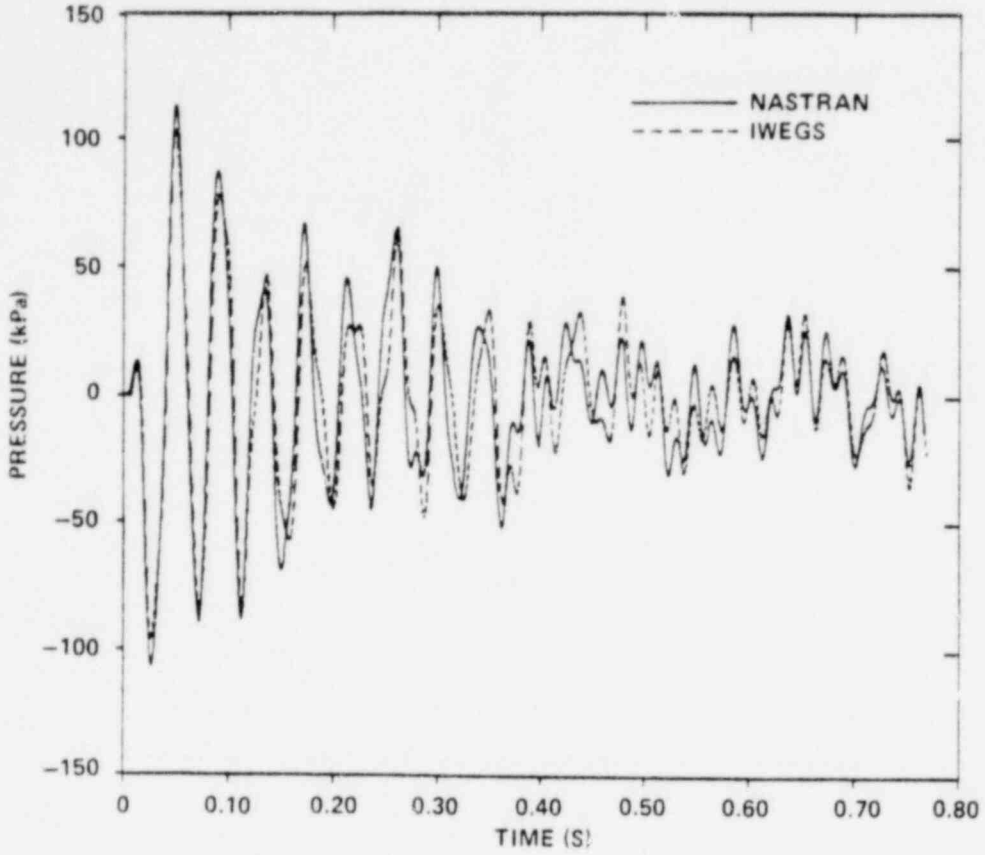

(a) PRESSURE

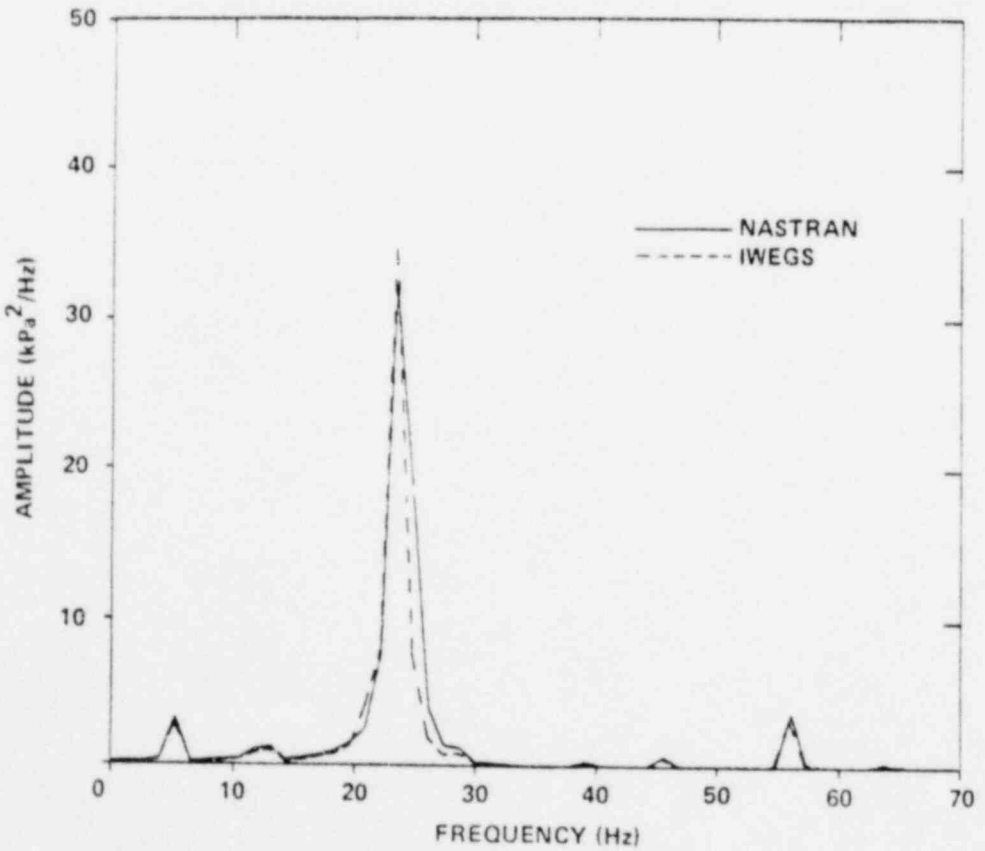

(b) SPECTRAL DENSITY

Figure 5-9 Comparison of IWEGS and NASTRAN in a Flexible Wall 4T

6. COMPARISON OF CHUGGING METHODOLOGY WITH 4T DATA

In the preceding chapters we have discussed in detail a chugging methodology which separates the chugging phenomenon into three parts: source, transfer function, fluid-structure interaction. We argued that the chug source was an impulse or series of impulses delivered to the pool by the collapse of steam bubbles. Since we did not model the vent, the source had to include the vent response felt by the pool. We showed in some detail that, to an excellent approximation, the pool transfer function can be represented by the acoustic wave equation. Finally, we determined that the fluid-structure interaction could be incorporated either via "separability" as shown by Sonin[33] or by simply solving the acoustic wave equation with flexible boundaries[38,39]. The flexible boundary solution required knowing how to obtain the appropriate frequency shift $\omega_N - \omega_N^o$ and damping constant λ_N, and we have demonstrated that such "know-how" is available. These, then, form the elements of the Mark II Improved Chugging Methodology.

In this chapter we shall demonstrate the utility of this methodology by comparison with the 4T data. For this comparison we will incorporate the 4T fluid-structure interaction via the flexible wall solution of the acoustic wave equation.

6.1 Source Investigations

Preliminary investigations of the chugging phenomena in the 4T were made using simple source density functions with IWEGS. Two types of source functions were used:

(1) Impulse, or triangular shape, and
(2) Simple harmonic, or sine waves.

All runs made were for the 4T geometry using the parameter values shown in Table 6-1.

Table 6-1

IWEGS INPUT FOR 4T PROBLEM

Pool Depth	=	7.01 m (23 ft)
Pool Diameter	=	2.13 m (7 ft)
Sonic Velocity	=	1524 m/s (5000 fps)
Damping	=	0.0%
Source Elevation	=	3.66 m (12 ft)
Density of Fluid	=	1000 kg/m^3 (62.4 lbm/ft^3)

6.1.1 Impulse Source

The triangular shaped impulse source function of 10 ms duration and 5.2 m^3/s^2 amplitude was first employed. The results are shown in Fig. 6-1. Part (a) is the source strength time-history, part (b) is the pressure response at the bottom-center of the tank, and part (c) is the spectral density of the pressure response. The spectrum density shows peaks near 55, 160, and 270 Hz. From Eq. (4.20) using parameter values from Table 6-1, the longitudinal normal modes are:

Fundamental	-	54.35 Hz
1st Harmonic	-	163.04 Hz
2nd Harmonic	-	271.74 Hz

which agree very well with the spectrum peaks of Fig. 6-1(c). Again using Eq. (4.20), using α_{01} = 1.2197, the first radial mode is 872.91 Hz. Because the width of the impulse is relatively long and the response has a factor of ω_n^{-3}, the amplitude of this mode will be very small. Hence, for the 4T, the wave motion may be considered entirely one-dimensional, or longitudinal. As we shall see later, we do not expect this to be necessarily true for the Mark II annular geometry.

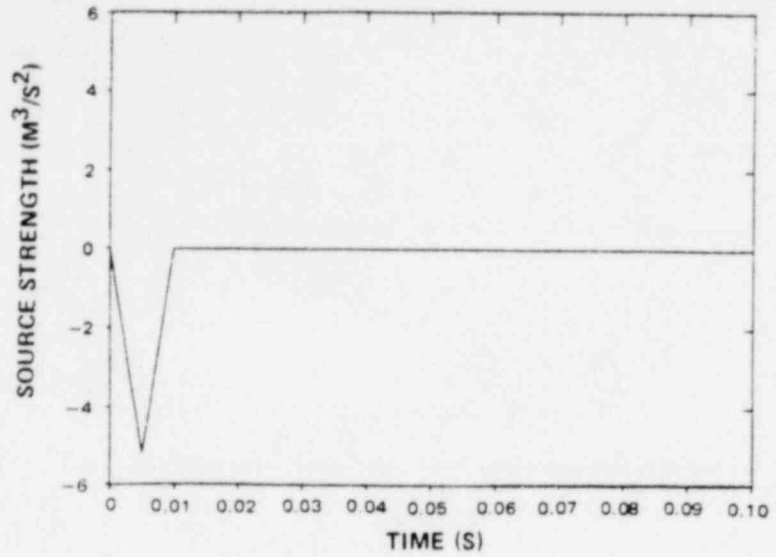

(a) SOURCE TIME-HISTORY

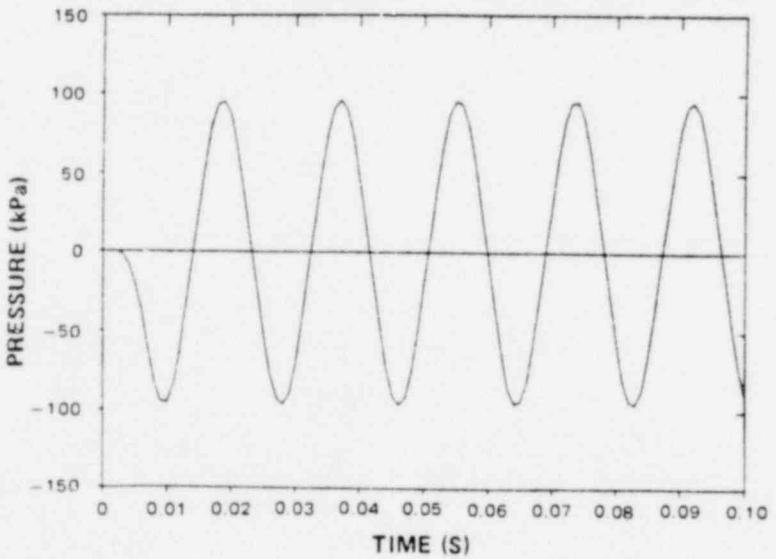

(b) 4T BOTTOM-CENTER PRESSURE TIME-HISTORY

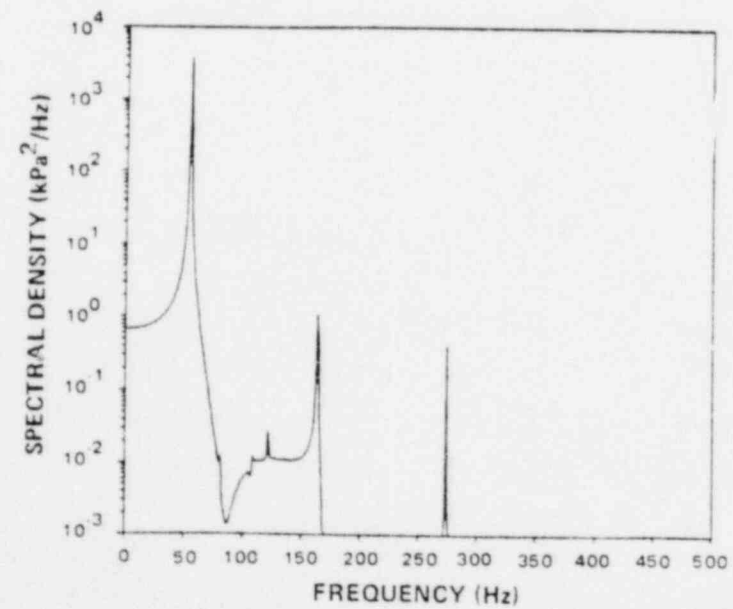

(c) PSD OF PRESSURE TIME-HISTORY

Figure 6-1 Source Investigations - 10 ms Impulse

A triangular shaped impulse source function of 20 ms duration was next employed. The results are shown in Fig. 6-2. As can be seen from the spectral density, part (c), the results are similar to the 10 ms triangle test. This is not an unexpected result. In general, if $S_\omega(\vec{r}_o)$ represents the Fourier transform of the time dependence of a point source, the Fourier transform of the resulting pressure field $p_\omega(\vec{r})$ is given by

$$p_\omega(\vec{r}) = H_\omega(\vec{r}|\vec{r}_o)S_\omega(\vec{r}_o), \tag{6.1}$$

where $H_\omega(\vec{r}|\vec{r}_o)$ is the transfer function from $\vec{r}_o$ to $\vec{r}$ and is the Green's function multiplied by the fluid density (see Eq. (5.44)).

Thus, we expect the p_ω to contain spectrum peaks in proportion to the eigenvalue content of S_ω. The spectral densities of the 10 ms and 20 ms triangles are shown in Fig. 6-3. Examination of this figure reveals that each source function exhibits power at the normal modes, although the power of the 20 ms triangle is somewhat less than the 10 ms triangle. As we shall see later, this type of analysis can be used to tailor the source function to adequately represent the test data.

6.1.2 Harmonic Source

A simple harmonic, or sine wave source function with a frequency of 5 Hz and 5.2 m^3/s^2 amplitude was next employed. The results are shown in Fig. 6-4. A 10 Hz sine wave source function of the same amplitude was also employed and the results are shown in Fig. 6-5. In both cases, the results were similar; the output pressure response was a sine wave at the same frequency as the input function. The spectrum densities show very small peaks at the pool fundamental mode. This is consistent with acoustical theory. If a system is driven at a frequency lower than the fundamental mode, the system will oscillate at the driver frequency with some excitation of the normal modes.

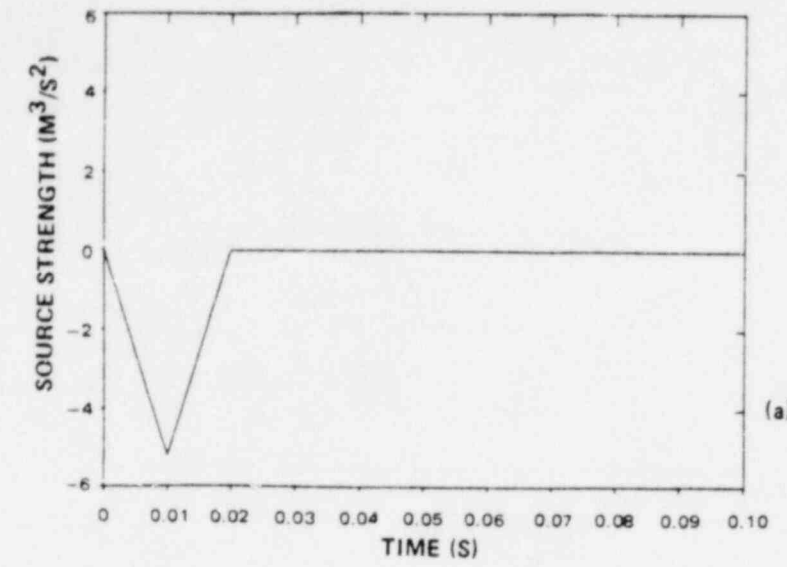

(a) SOURCE TIME-HI. "ORY

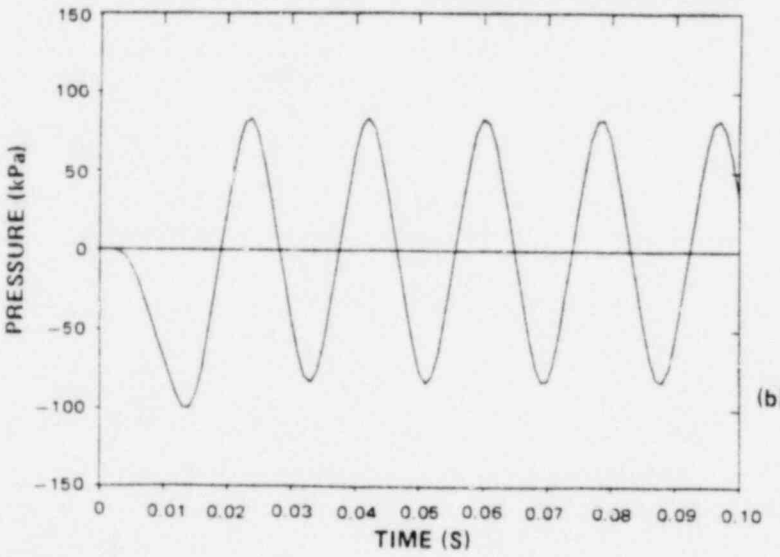

(b) 4T BOTTOM-CENTER PRESSURE TIME-HISTORY

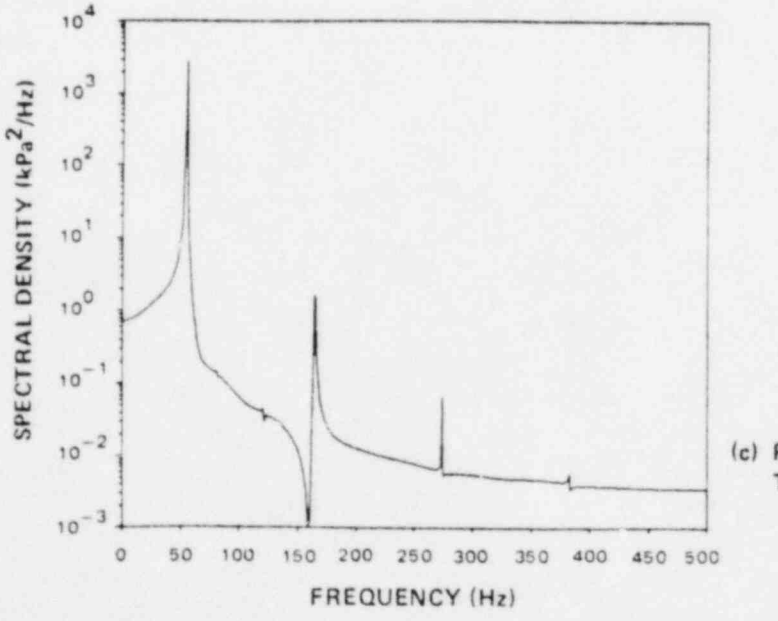

(c) PSD OF PRESSURE TIME-HISTORY

Figure 6-2 Source Investigations - 20 ms Impulse

G1002820-118

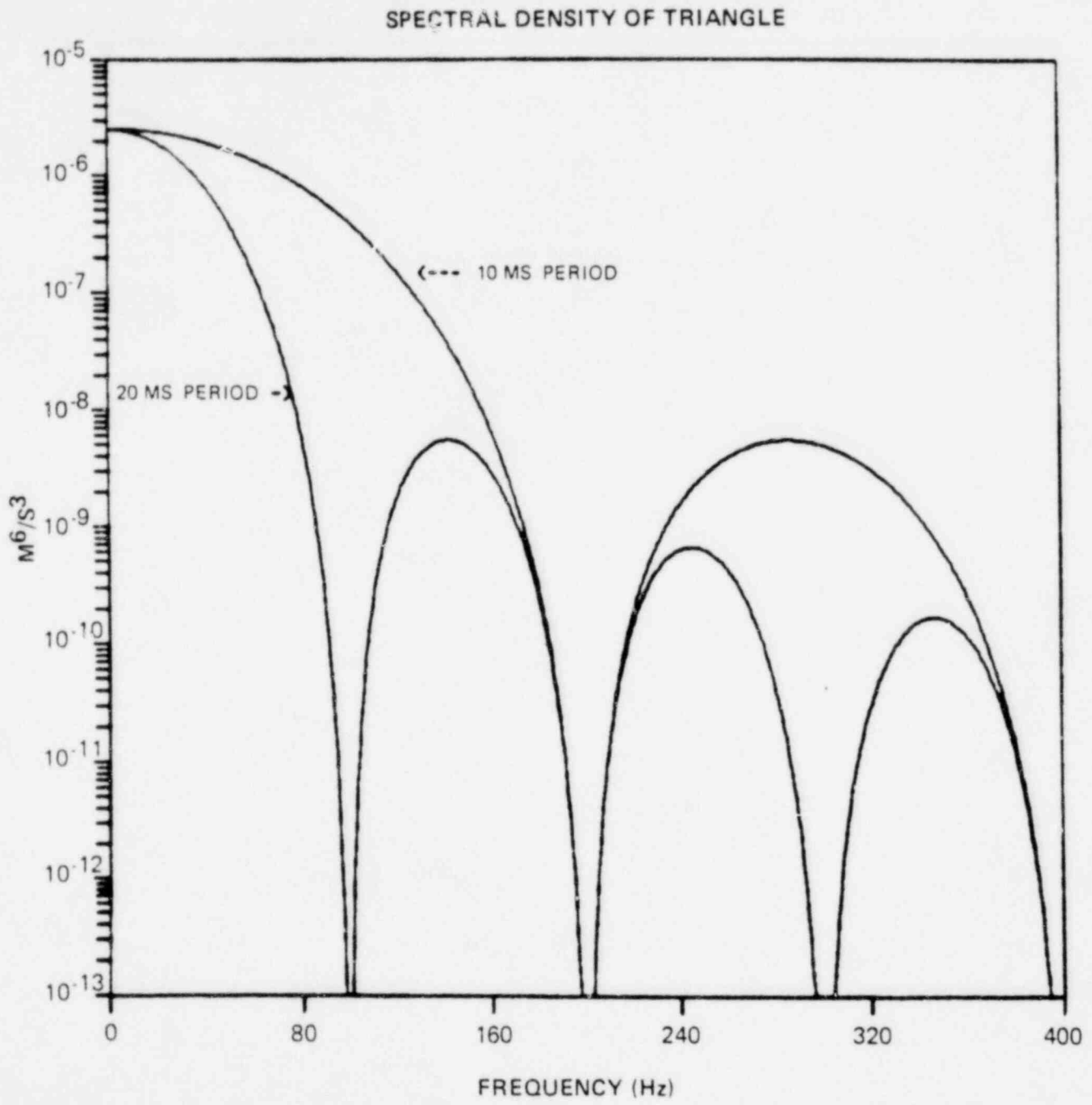

Figure 6-3 Spectral Density of 10 ms and 20 ms Impulse

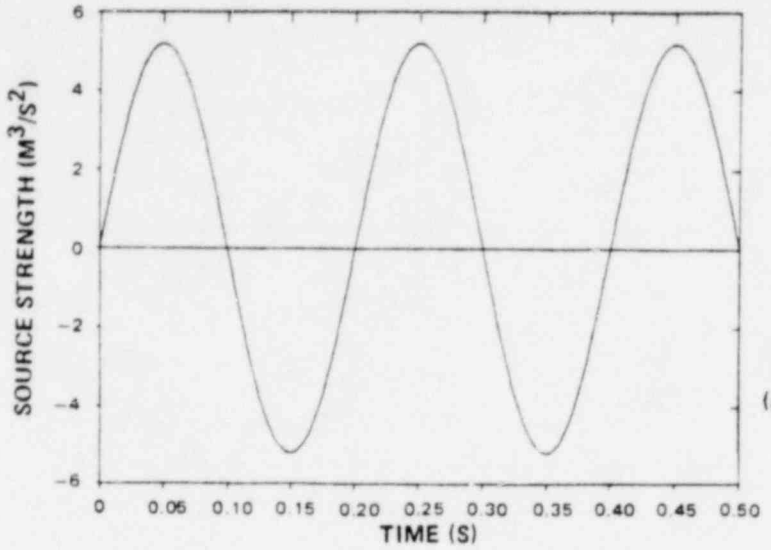

(a) SOURCE TIME-HISTORY

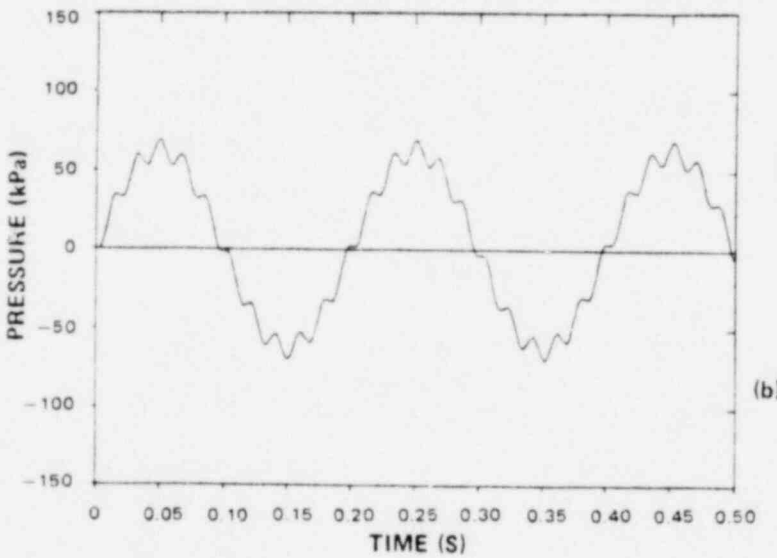

(b) 4T BOTTOM-CENTER PRESSURE TIME-HISTORY

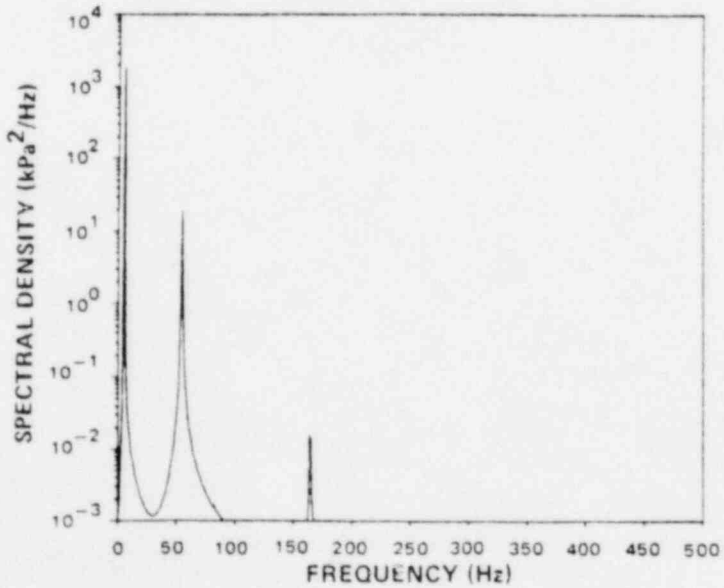

(c) PSD OF PRESSURE TIME-HISTORY

Figure 6-4 5 Hz Sine Wave Source Results

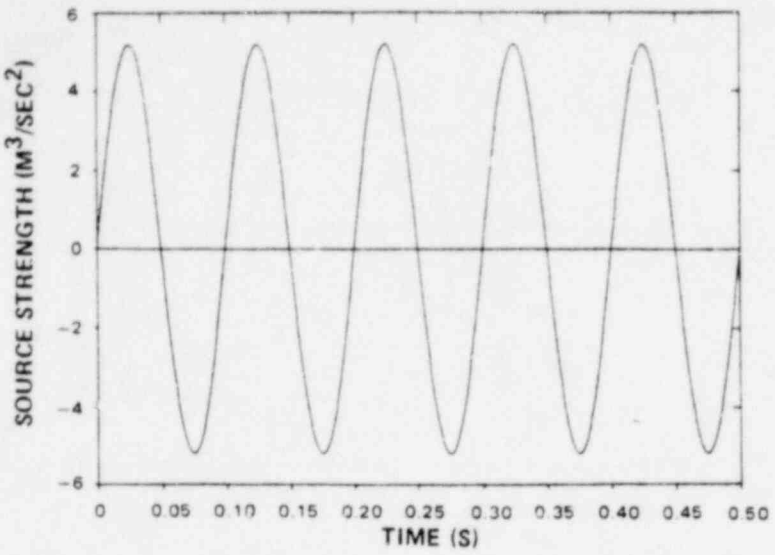

(a) SOURCE TIME-HISTORY

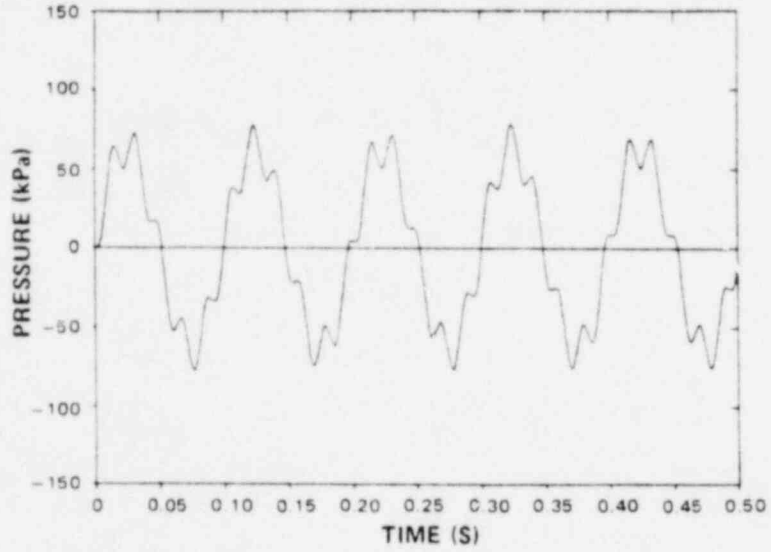

(b) 4T BOTTOM-CENTER PRESSURE TIME-HISTORY

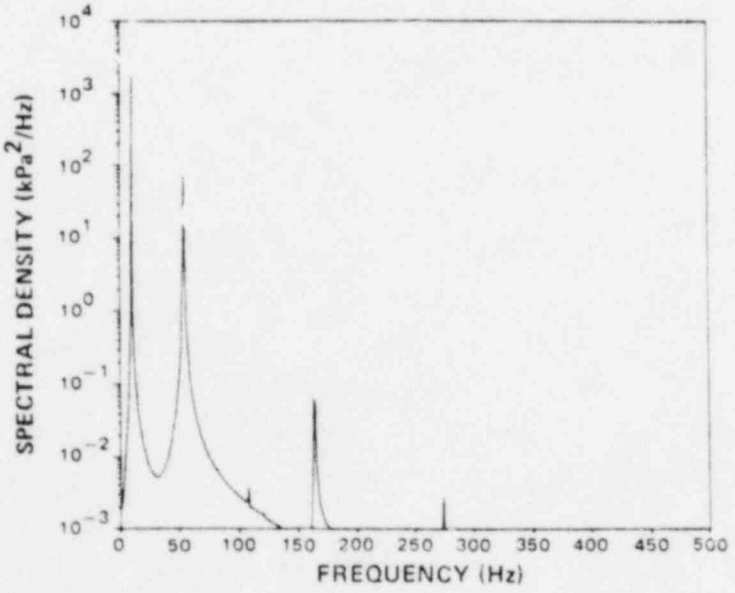

(c) PSD OF PRESSURE TIME-HISTORY

Figure 6-5 10 Hz Sine Wave Source Results

6.2 4T Sources

We have investigated briefly the behavior of the acoustic model with several very simple sources. An impulse source was shown to excite the pool fundamental frequency and the response from a simple low-frequency sine wave source was found to be relatively unchanged at the wall. We now attempt to reproduce the major chug types in the 4T data by devising more sophisticated sources for input to the acoustic model. We look at the Category I and II chugs for this comparison since they are the basic types of 4T chugging data. Category III chugs can be made by combining chugs from Categories I and II, and Category IV chugs are bounded in amplitude by Categories I and II.

The objective of this investigation was to find the source giving an acoustic model response which best represents the available test data. In Chapter 3 we argued that the chug source is either a single large impulse, a series of smaller impulses, or a combination of the two. It is not our intention to develop a chug source theoretically. According to experts in bubble collapse, no satisfactory theory currently exists[12]. Instead, we choose to create a source semiempirically, using the 4T chugging data base, and let ourselves be guided by theory whenever necessary.

If $p_\omega(\vec{r})$ is known, $S_\omega(\vec{r}_o)$ can be empirically obtained via

$$S_\omega(\vec{r}_o) = H_\omega^*(\vec{r}|\vec{r}_o)p_\omega(\vec{r})/|H_\omega(\vec{r}|\vec{r}_o)|^2 \qquad (6.2)$$

where H_ω^* is the complex conjugate of H_ω and $|H_\omega|^2 = H_\omega^* H_\omega$. Eq. (6.2) states that the source is that function which, when operated on by the transfer function, produces the observed pressure response. It is a perfectly proper way in which a source function for a complicated phenomenon can be obtained. However, besides being somewhat difficult

to carry out, a source definition via Eq. (6.2) has the added disadvantage that it is not obvious how to perform the necessary vent-frequency transformation when transporting $S_\omega(\vec{r}_o)$ from 4T to Mark II. Thus, we decided to construct a far simpler source from impulses and sines with adjustable constants having values obtained from the data being simulated. Transporting these sources to Mark II would present no special problem since that part of the source associated with vent frequencies is clearly indicated.

6.2.1 Category I Source

A Category I source is presumed to be composed of an impulse to represent steam bubble collapse plus a damped harmonic series to represent the influence of the vent response to that impulse on the pool. For impulse shape, we are guided by the inertia collapse of a spherical cavity (Rayleigh collapse)[13,14] because this type of collapse produces a pressure response indicative of a Category I chug (see Fig. 3-2). The acoustic source produced by such collapse, however, becomes inapplicable as the collapse proceeds. This is due, in addition to the reasons stated in Chapter 3, to the fact that the cavity can collapse into the vent, as in the case of the Anamet bell jar tests.

We proceed in an *ad hoc* fashion as follows to obtain an approximate impulse shape of an inertially controlled steam bubble collapse into a vent. Initially, the bubble radius is assumed to have a radius equal to that of the vent. As the collapse proceeds, the acoustic source strength is given heuristically by Eq. (3.1) until the surface area of the bubble ($2\pi R^2$) is equal to the cross-sectional area of the vent. Thence, the source is equal to zero. The resulting source and a comparable triangular impulse are pictured in Fig. 6-6a and the corresponding spectral densities in Fig. 6-6b. Although the preceding is only a plausibility argument for representing an inertially controlled bubble collapse with a triangular impulse, this must be close to the true source shape because, when input to the transfer function $H_\omega(\vec{r}|\vec{r}_o)$, the resulting pressure response compares well with the Anamet bell jar tests as shown below. In fact, due to the similarity of the Fourier

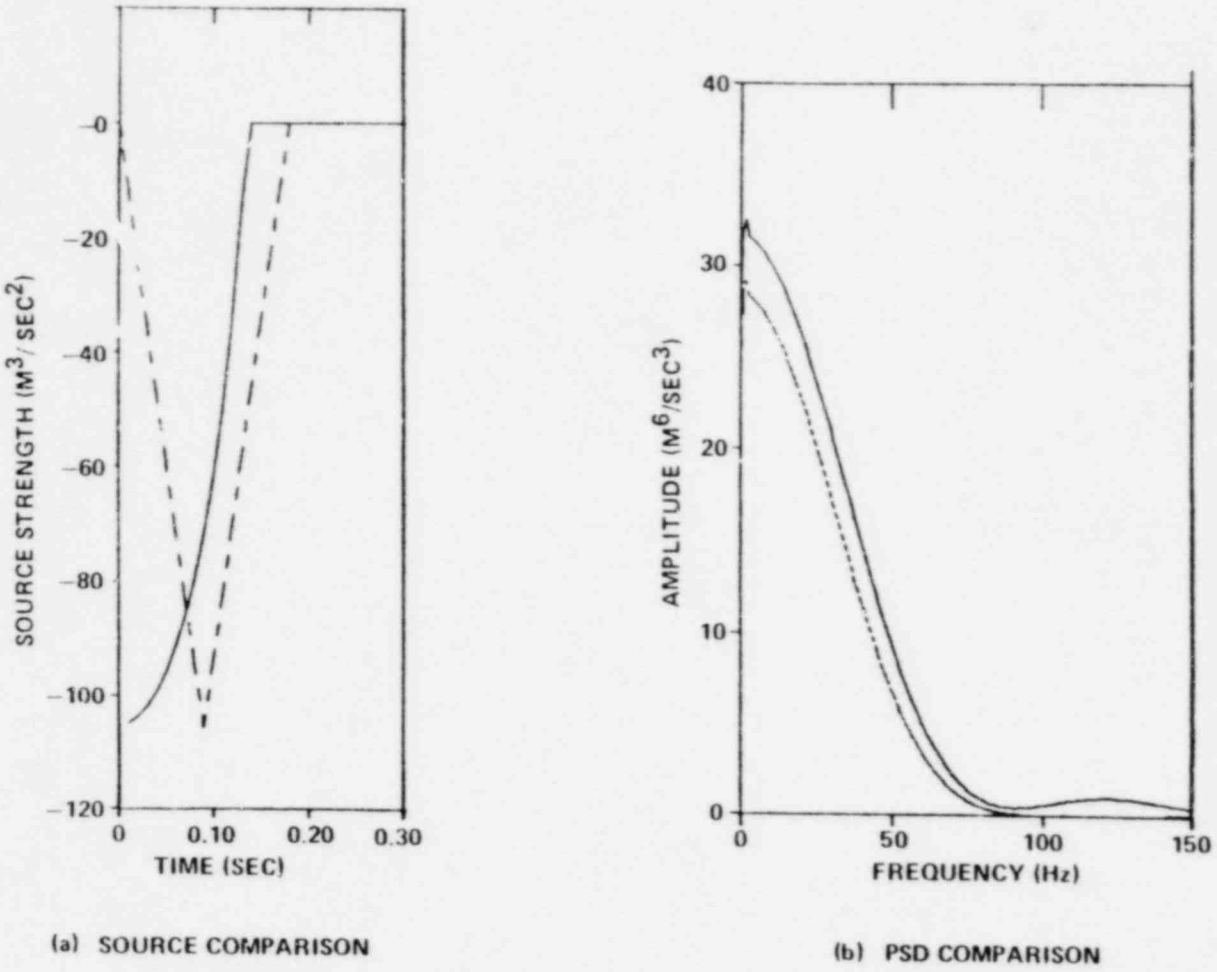

(a) SOURCE COMPARISON

(b) PSD COMPARISON

Figure 6 6 Impulse Source Spectral Density

transform for a number of functional shapes, we could have equally well chosen a rectangular or haversine impulse[56].

In addition to the impulse, the Category I source must include the response of the vent. This is shown by the results of our K-FIX simulation (see Fig. 3-7). The vent response is a damped harmonic series as is clearly shown by a low pass filtering of the test data as shown in Fig. 6-7. Thus, the complete Category I source is given by

$$S_I(t) = - A_o \Lambda\left(\frac{2t}{\tau} - 1\right) + \sum_{n=1}^{N} A_n \, e^{-\alpha\omega_n t} \sin(\omega_n t), \qquad (6.3)$$

where the ω_n are the vent acoustic frequencies. The constants A_o, A_n, τ, α, and the number of vent frequencies N are obtained from the test data and given in Table 6-2. The comparisons of our general Category I source with the Anamet bell jar test, Chug #30, and Chug #71 with test data are shown in Figs. 6-8, 6-9, and 6-10.

6.3 Category II Source

A Category II source is presumed to be composed of a series of small impulsive bubble collapses. The frequency of these "minichugs" is controlled by the vent acoustic frequencies (see Table 2-3). Thus, we represent a Category II source with

$$S_{II}(t) = u(T-t) \sum_{n=0}^{N} B_n \sin(\omega_n t), \qquad (6.4)$$

where u(x) is the Heaviside step function. The constants T and B_n are obtained from the test data and given in Table 6-3. The comparisons of our general Category II source with representative Category II chugs,

Figure 6-7 Chug #30 Low-Pass Filtered at 17 Hz
(GENERAL ELECTRIC COMPANY PROPIETARY)

Table 6-2

CATEGORY I SOURCE PARAMETERS FOR
ANAMET BELL JAR TEST, 4T CHUG #30 AND CHUG #71

$$S(t) = - A_o \Lambda\left(\frac{2t}{\tau} - 1\right) + \sum_{n=1}^{N} A_n e^{-\alpha\omega_n t} \sin(\omega_n t)$$

Parameter	Anamet	Chug #30	Chug #71

The following Figures are GENERAL ELECTRIC COMPANY PROPRIETARY and have been removed from this document in their entirety.

6-8 Comparison with Anamet Bell Jar Test No.8

6-9 Comparison with Data - Chug No.30

6-10 Comparison with Data - Chug No. 71

Table 6-3

CATEGORY II SOURCE PARAMETERS FOR
4T CHUG #11 AND CHUG #57

$$S_{II}(t) = u(T-t) \sum_{n} B_n \sin(\omega_n t)$$

	Chug #11	Chug #57

Chug #11 and Chug #57, are shown in Figs. 6-11 and 6-12.

Using the flexible wall solution to the acoustic wave equation, we postulated a Category I and II source function which contained adjustable constants. These constants in general vary from chug to chug due to the random nature of the chugging phenomenon. For appropriate choices of these constants, sonic velocity, and pool damping, any chug can be simulated with either the Category I source, the Category II source, a combination of the two, or, ultimately, a source defined by Eq. (6.2). The advantage of our Category I and II sources is that they are tractable and can be combined in such a manner to obtain a design source with relative ease. The sources clearly identify which parts are related to the vent acoustic frequencies and are transportable from 4T to Mark II in a trivial fashion.

The following Figures are GENERAL ELECTRIC COMPANY PROPRIETARY and have been removed from this document in their entirety.

6-11 Comparison with Data - Chug No.11

6-12 Comparison with Data - Chug No.57

7. MARK II DESIGN SOURCE APPLICATION

7.1 Introduction

The strategy will be to find a volumetric acceleration time dependent point source at the 4T vent exit which produces a pressure signal at the 4T bottom-center that fulfills certain signal strength, frequency, amplitude, and decay criteria. A single source representative of actual random sources will be found. This source will be regarded as characteristic of chugging and associated system responses so that, after frequency modification for the vent length element of the system and considering a range of pool acoustic speeds, it can be used in Mark II. The signal will be subject to a different damping criterion from source to pool boundary in Mark II than in 4T. The distribution of source strengths in 4T is considered to be applicable to Mark II plants because of the prototypical nature of the 4T geometry and test conditions.

Two loading cases will be provided: symmetric and asymmetric. For the symmetric case, the source will be applied synchronized at all vents. For the asymmetric case, the waveform of the symmetric case source will be increased and decreased in amplitude and each will be applied synchronized at all vents in each half of the pool. The criteria and source history for the symmetric case will now be described.

7.2 Symmetric Load Case

For the symmetric loading case, the design source found is to correspond to a Mark II suppression pool boundary forcing function which is suitably conservative with respect to its anticipated structural consequences on the basis of the maximum average pressure over the pool boundary; that is, maximum in time and average spatially. Thus, conservatism with respect to responses due mainly to vertical floor modes and symmetric shell modes is provided for. It is

assumed that a maximum average pressure criterion will be conservatively implemented by considering that all vents chug synchronously. And, it is assumed that chugs which occurred sequentially at the 4T vent can occur simultaneously at plant vents on the bases of (1) lack of trend with time into test of chug strength, as shown in Fig. 7-1 which shows chug RMS by time into test, and (2) actual chug strengths depending on local steam-water interface conditions at vent exits, which will differ among vents. The source for a suitably conservative maximum average pool boundary pressure in Mark II will produce a pressure history at bottom-center of 4T which meets criteria for signal strength, frequency content, peak and final amplitudes, and decay rate. These criteria will now be described.

(1) Criterion for Signal Strength

Overall signal strength will be characterized by the mean square 4T bottom-center pressure (BCP) signal taken over 0.768 seconds, chosen as discussed in Section 2. Since the average effect of all vents chugging with different actual chugs is anticipated to be applicable in Mark II, one might adopt the mean mean square of the 137 chugs in the data base, which was 110.3 kPa^2 (2.32 psi^2). But conservatism was introduced by assuming that only Category I and III (higher strength) chugs might occur in a Mark II pool instead of essentially the same distribution among chug categories as in the data base and adopting as the design objective mean square that of the mean of the 39 Category I and III chugs. This is 181.6 kPa^2 (3.82 psi^2).

(2) Criterion for Frequency Content

There are three parts to the criterion for frequency content.

First, the strong 5 and 13 Hz components are taken as fundamental and first harmonic of the vent acoustic response. These frequencies, increased in the Mark II application by the ratio of 4T vent length

Figure 7-1 Chug rms versus Time into Test

(GENERAL ELECTRIC COMPANY PROPRIETARY)

to plant vent length, are to be applied in the source as 0.768-second sinusoids with zero phase. As to strength, the 4T BCP PSD of these frequencies must bound the mean PSD of these frequencies for the 137-chug data base.

Second, the strong signals in the 20 to 30 Hz range are taken as pool response reinforced by the second harmonic of vent response varying in frequency because of changes in pool acoustic speed. The mean PSD in this range for Categories I and III is bounded by the 4T BCP from the design source. To cause this BCP signal, an initial negative triangular impulse is used in the design source, the acoustic pool model producing the appropriate frequency at 4T BCP using a selected pool acoustic speed following correction for fluid-structure interaction. This frequency will be modified in Mark II by requiring that a range of pool acoustic speeds from 732 to 1311 m/s (2400 to 4300 fps) be used. (These values are without the 4T fluid-structure interaction correction.) The source impulse does not change, however. A source base width of 0.036 seconds is chosen based on the observed duration of prechug underpressure in 4T.

And third, higher frequencies are introduced in the 0.768-second zero-phase sinusoids in the source at discrete higher vent harmonics having strength sufficient to bound the mean PSD of the 137-chug data base from 30 to 80 Hz. The frequencies of these signals are also to be increased by the vent length ratio.

(3) Criteria for Peak and Final Amplitudes

While it is assumed that any signal waveform fulfilling the mean square and frequency criteria will cause similar structural responses, two 4T BCP amplitude criteria are also adopted. First, it is required that the 4T BCP signal from the design source have a peak positive overpressure (POP) at least equal to the mean POP of Category I and III chugs. This is 55.9 kPa (+8.1 psi). It is required to occur on the first positive cycle, as in the 4T waveforms. And second, it was required that the final cycle have peak amplitudes of ±20.7 kPa

(±3 psi), values conservatively representative of 4T BCP signal amplitudes at the end of the 0.768-second period.

(4) Criterion for Decay

The 4T data exhibit a decaying waveform in both the vent and the pool for the Category I and III chugs. It is expected that the Mark II will display similar decaying waveforms; however, the rate of decay is not expected to emulate that observed in 4T. Thus, for conservatism, it is required that the signal associated with the 4T vent waveforms be incorporated into the source as unattenuated (undamped) sinusoids. The only damping allowed will be that originating from structural damping specified by regulatory guide as Mark II unique. That damping characteristic of Category I and III chugs in 4T corresponds to 4.5% in the fluid. To ensure that there has been no error toward nonconservatism, the Mark II chugging design source will be constructed using a value of damping in the 4T fluid of 6%. This requires a stronger source to produce the same BCP in 4T than otherwise would be the case.

The design source found meets all of these criteria. It can be expressed by the equation

$$S(t) = - A_o \Lambda\left(\frac{2t}{\tau} - 1\right) + \sum_{n=1}^{8} A_n \sin(2\pi f_n R t) \qquad (7.1)$$

where $S(t)$ is the volumetric point source acceleration, m^3/s^2, and $\tau = 0.036$ second is the duration of the impulse. The triangular impulse function Λ is defined by Eq. (3.3). Values for the design chug source parameters are given in Table 7-1. Note that this source is made unique for each Mark II via the parameter R which is defined as the ratio of the 4T vent length 28.65 m (94 ft) to that of a specific Mark II.

Table 7-1

DESIGN CHUG SOURCE PARAMETERS

n	f_n (Hz)	A_n (m^3/s^2)
0	-	5.2
1	5	0.70
2	12.6	0.44
3	20.9	0.10
4	28.7	0.08
5	39.1	0.14
6	45.6	0.25
7	56.1	0.25
8	63.9	0.13

On criterion (1), the mean square of the design source signal at 4T BCP is 291.4 kPa^2 (6.13 psi^2), while the objective was 182.1 kPa^2 (3.82 psi^2). The excess is a consequence of fulfilling the other criteria.

On criterion (2), the PSD of the 4T BCP signal from the design source is compared to the mean PSD of all 137 chugs in the data base in Fig. 7-2. It is compared to the mean PSD of each chug category in Fig. 7-3 and to the mean PSD of Categories I and III in Fig. 7-4. The pool response peak at 25 Hz corresponds to an assumed acoustic speed of 701 m/sec (2300 fps) following adjustment for fluid-structure interaction and air content.

On criterion (3), the POP of the design source at 4T BCP is 75.1 kPa (10.9 psi) exceeding the criterion of 55.8 kPa (8.1 psi). The final amplitudes exceed ±20.7 kPa (±3 psi).

The design source history is shown in Fig. 7-5; impulse, sinusoids, and net signal are shown. The signal from it at 4T BCP is shown in Fig. 7-6.

Further indications of the degree of conservatism of the 4T BCP signal from the design source are that the mean square of 291.4 kPa^2 (6.13 psi^2) exceeds that of 91% of the chugs in the data base and the POP of 75.1 kPa (10.9 psi) exceeds that of 91% of the chugs in the data base.

The following Figures are GENERAL ELECTRIC COMPANY PROPRIETARY and have been removed from this document in their entirety.

7-2 Chug rms versus Time into Test

7-3 Comparsion of Design Source Rssponse PSD Compared to Mean PSDs of the Four Categories

7-4 Comparison of Design Source Response PSD to Category I and III PSDs

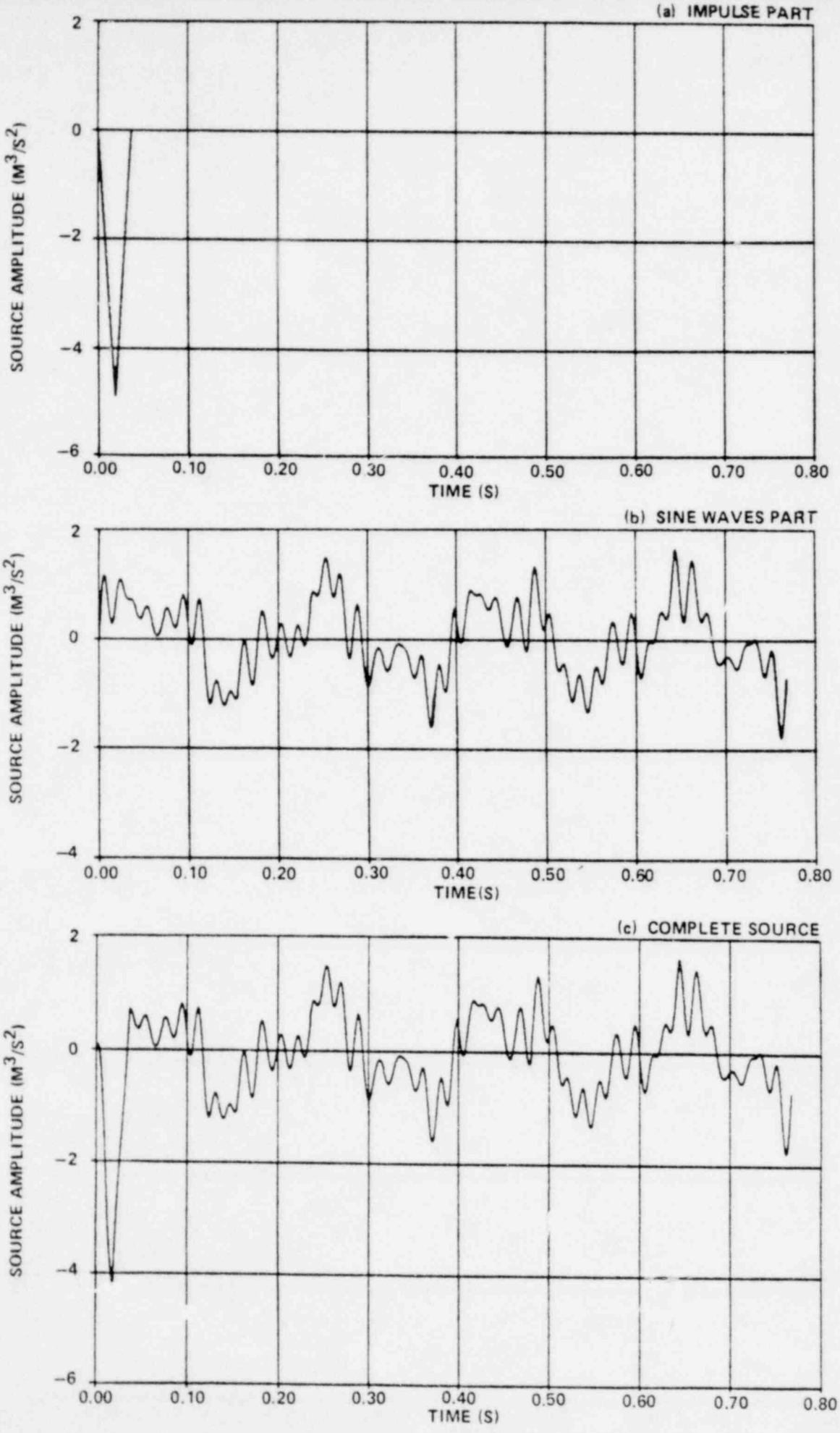

Figure 7-5 Design Source Time-History

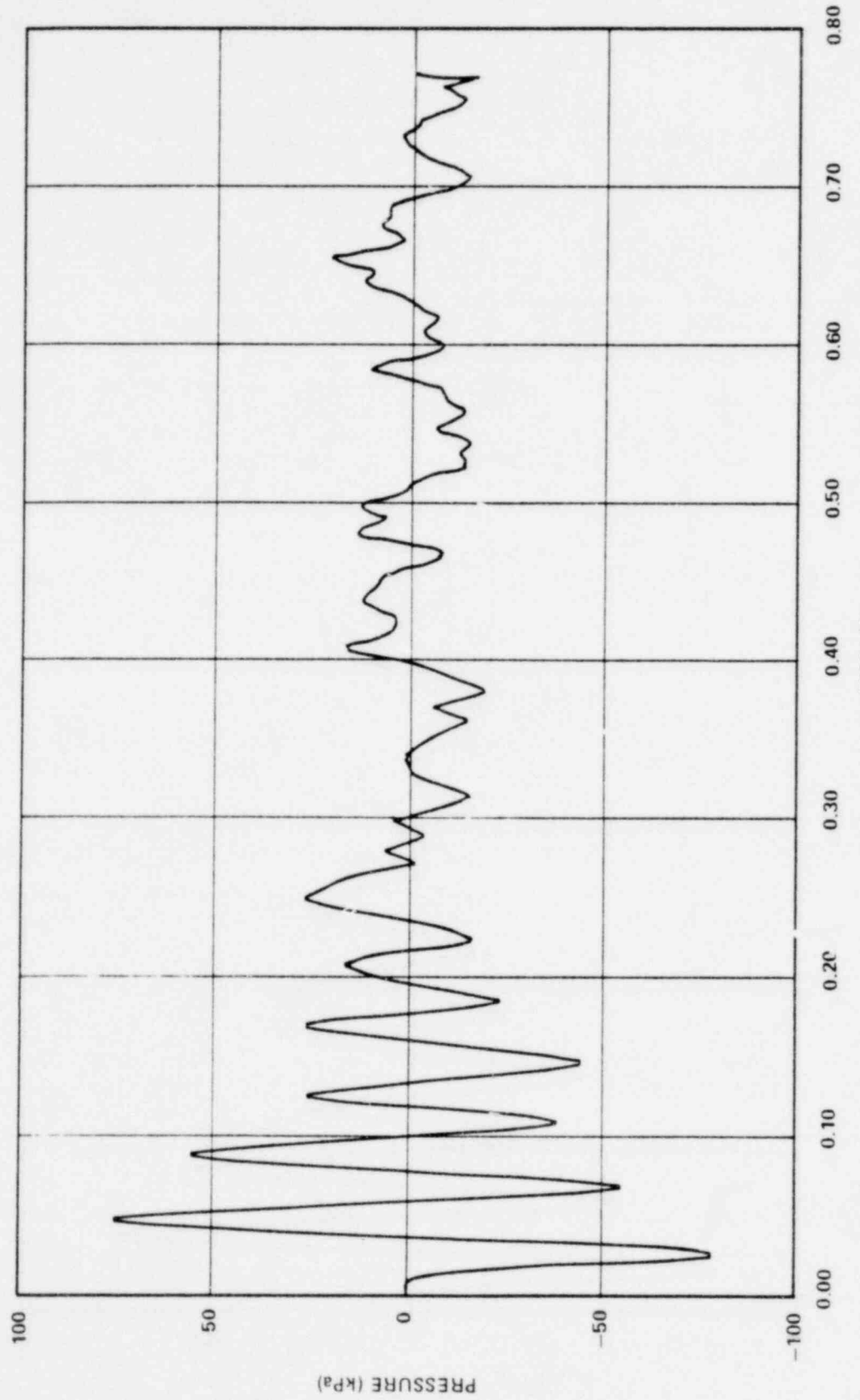

Figure 7-6 Design Source Pressure Response at Bottom-Center of 4T Tank

G1002820 89

Throughout this analysis, the 4T BCP signal mean square and PSD have been the principal bases for evaluating total signal strength and signal strength by frequency. Let us examine whether these are the measures most pertinent to structural consequence.

One alternative would be to use peak overpressure alone; but no frequency information is conveyed. Another alternative would be to use response spectra which evaluate the peak response of single degree of freedom (SDOF) "structures" for these highly transient chug events.

For low frequencies having few but constant-amplitude cycles during the chug event, the reduced response due to shortage of cycles to achieve steady state response would be properly reflected in the response spectrum. With the PSD, this problem is overcome by using the same time duration for application as was used for test evaluation. With response spectra, there is the question of whether the mean (peak) response at each frequency is a suitable profile for a mean "total" (all-frequency) response since there is no measure of total signal response. With the PSD, however, there is a single measure of total signal strength, the total mean square, and it is arithmetically equal to the area under the mean PSD values at all frequencies. Response spectra vary depending on the critical damping chosen, a factor not affecting PSDs. However, when it is required that a synthesized signal correspond to a target signal using response spectra, this is ordinarily done at two different damping values so that waveform by frequency is better matched.

In the case of chugging, as transient as many of the signals are, signal root-mean-square (RMS) by frequency from PSDs is very closely correlated with the 2% response spectrum by frequency. This is shown in Fig. 7-7 through 7-10 for four different frequency ranges by there being little scatter of points about the lines. (The slopes of the four lines are also nearly identical because the measured response spectrum values were adjusted to steady state response by dividing by the fraction of steady state response achieved in the number of cycles

The following Figures are GENERAL ELECTRIC COMPANY PROPRIETARY and have been removed from this document in their entirety.

7-7 Steady State Response Spectrum versus rms 4T
Run 28 Chugs, 4 to 6 HZ

7-8 Steady State Response Spectrum versus rms 4T
Run 28 Chug, 13 Hz

7-9 Steady State Response Spectrum versus rms 4T
Run 28 Chugs, 17 to 22 Hz

7-10 Steady State Response Spectrum versus rms 4T
Run 28 Chugs, 30 Hz

of the particular peak frequency which occurs in the 0.768-second interval. This fraction of steady state cycles for 2% damping systems appears in Fig. 7-11.) Thus, the PSD method reliably reflects structural consequence by frequency, even for events as transient as chug response signals. Nevertheless, to ensure that any possible special effect of waveform on structural response is considered, peak and final amplitudes are included in the criteria.

The symmetric case fulfills the Newmark-Kennedy criteria for combining response peaks by the square root of the sum of the squares (SRSS) method. Two of the criteria deal with forcing function peak amplitudes. One is that the design peak amplitude exceeds the upper 84% point in the distribution of peak amplitudes among recurrences of the event. For the symmetric case, the mean mean square is 110.3 kPa^2 (2.32 psi^2) and the variance among mean squares is 1763 kPa^4 (0.78 psi^4) for a standard deviation of 42.3 kPa^2 (0.89 psi^2). Taking the distribution of mean squares as approximately normal out to a least one standard deviation, the upper 84% point is at mean plus one standard deviation, which is 152.1 kPa^2 (3.20 psi^2). Because the 4T BCP mean square of the design source is 291.4 kPa^2 (6.13 psi^2), it clearly meets this Newmark-Kennedy criterion since probability points for both peak amplitude and mean square will correspond for similar overall waveforms. The other Newmark-Kennedy criterion on peak amplitude is that the ratio of design to median peak amplitude is at least 1.15. Using the mean mean square for the median, the ratio of peak amplitudes for similar waveforms can be found from the square root of the ratio of mean squares, $(6.13/2.32)^{1/2} = 1.63$, which exceeds 1.15. Thus, the design objective mean square for the symmetric case meets the two Newmark-Kennedy peak amplitude criteria. Other criteria on signal duration, waveform, and zero mean must also be met by examination of forcing function histories.

7.3 Asymmetric Load Case

Attention will now be turned to the asymmetric load case.

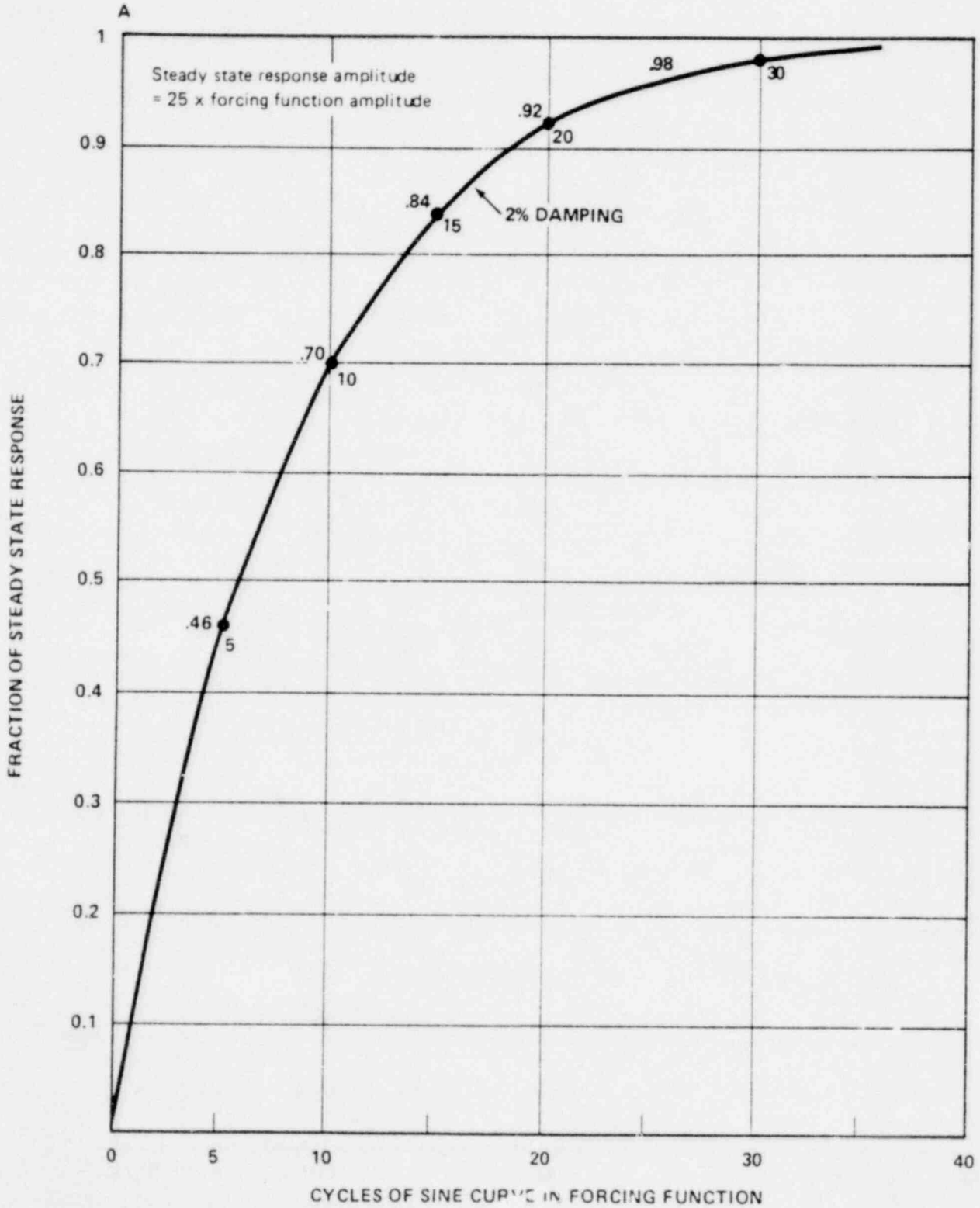

Figure 7-11 Fraction of Steady State Response Due to a Limited Number of Applied Cycles

In principle, chugging could produce some lateral force or overturning moment on the pool boundary as well as a symmetric force. This could be due to unequal strengths among chugs or to pool boundary signals which are not exactly in phase throughout the pool. To account for this possibility, an asymmetric load case will also be provided. It will be defined in terms of vertical moment on the floor, and it will be assumed that the source pattern developed will also have essentially the same conservatism for other characterizations of asymmetric loading such as containment lateral force, etc. The criterion will be in terms of a quantity called RMS-moment. Compared to maximum actual floor moment, which is the integral of the pressure-area-moment arm product taken at an instant when there is an unfavorable combination of pressure values over the floor, the RMS-moment is the sum of products of RMS values at 4T BCP of randomly chosen chugs and the moment arm of a point beneath each vent. The RMS-moment is selected because its probability distribution is much easier to evaluate than that of the actual moment, yet a chosen asymmetric pattern of sources will be equally conservative in its effect in both distributions as to having a selected small exceedance probability. That is, the values in the probability distributions of RMS-moment and maximum actual moment are assumed to be simply proportional to each other.

A number of general aspects of the RMS-moment will be touched on, followed by further details on some assumptions, and then a derivation of the $1 + \alpha$ and $1 - \alpha$ adjustment factors required.

Maximum actual floor moment will have plant-specific values and will depend on the nature of pool modal response. To provide an appropriate generic asymmetric set of sources, however, the view is taken that a source will cause a 4T BCP single-cell pressure history over a region beneath each vent, the region for each vent having the same area. In actuality, if pool boundary pressures are not synchronized over the pool and/or result from varying source strengths, the fact that identical instantaneous single cells would not be formed over the pool could be expected to lead to decreased pressures where high pressures were expected and increased pressures where low pressures

where expected with the result that maximum actual moments could easily be less than implied by the spatial distribution of their sources. Thus, it is regarded as either appropriate or conservative to characterize a possible asymmetric effect of chugging in terms of sources which would produce a chosen 4T BCP RMS-moment over the floor. By considering the probability distribution of 4T BCP RMS values, we can proceed with a method which assumes that such RMS values occur randomly over the pool, from which, by statistical methods, we can characterize the probability distribution of RMS-moment, select an upper probability point, devise any one simple actual deployment of RMS values such that they provide the desired RMS-moment, and make a corresponding deployment of source strengths at the vents.

There is evidence that the foregoing approach is valid regardless of the detailed phasing relationship among pool boundary signals. That is, for all signals in phase but of a different strength over the pool or randomly separated signals in their degree of synchronization, sensitivity testing using potential flow shows that virtually the same value of maximum instantaneous containment lateral force is achieved - at a chosen small exceedance probability - regardless of the exact synchronization of the chug signals from fully synchronized to random variation up to one-third of the 0.768-second chug duration. Greater desynchronization leads to a decreased asymmetric effect. Thus, for simplicity, sources may be applied synchronized for the asymmetric case, as for the symmetric case, and still provide a suitably conservative asymmetric pressure effect.

This completes the assumption of the method. A number of aspects will now be discussed in detail, following which the equations will be derived for calculating the two required chug source strengths.

Since appropriate source strength by frequency was used in the symmetric case, the same source history waveform is used for the symmetric case except it is reduced and increased in amplitude for application to the two halves of the pool. Thus, the asymmetric case

is just as conservative in its symmetric effect as the symmetric case itself but it additionally provides a conservative asymmetric excitation.

If it is assumed that all vents may not chug at near the same time, the spatial distribution of vents not chugging is regarded as random with the effect that the floor moment would simply be reduced in magnitude. Accordingly, it is assumed that all vents chugging will provide the highest floor moment.

Under random assignment of chug strengths to vents, it is surprising to note that exact chug synchronization - and thus simultaneous occurrence of peak pressure values on the pool boundary - leads to the same asymmetric effect at some small nonexceedance probability as do various degrees of random nonsynchronization. A study using actual 4T chug bottom-center pressure histories showed that, in 50 trials of assigning randomly chosen 4T BCP histories to vent exits in a Mark II configuration under potential flow conditions, the maximum value of peak instantaneous lateral force on the containment portion of the pool boundary was very nearly the same for the cases of all chugs synchronized as it was for chugs occurring at random with a uniform probability distribution. This pattern is shown in Fig. 7-12. In the synchronized case, the lateral force was due to a relatively high positive pressure at one side of the containment together with a relatively low positive pressure at the other side. With nonsynchronization, positive and negative parts of the waveform can occur simultaneously; this feature tended to have a balancing effect so that the maximum peak lateral force was due ot a relatively high positive pressure on one side of the containment and a relatively low negative pressure on the other side. It is assumed that Mark II pool boundary chug wave forms would show a similar effect; therefore, the criterion for the asymmetric case deals with the distribution of peak pool boundary pressures occuring simultaneously-implemented in the distribution of the rms-monent-without the need to consider random phasing as well.

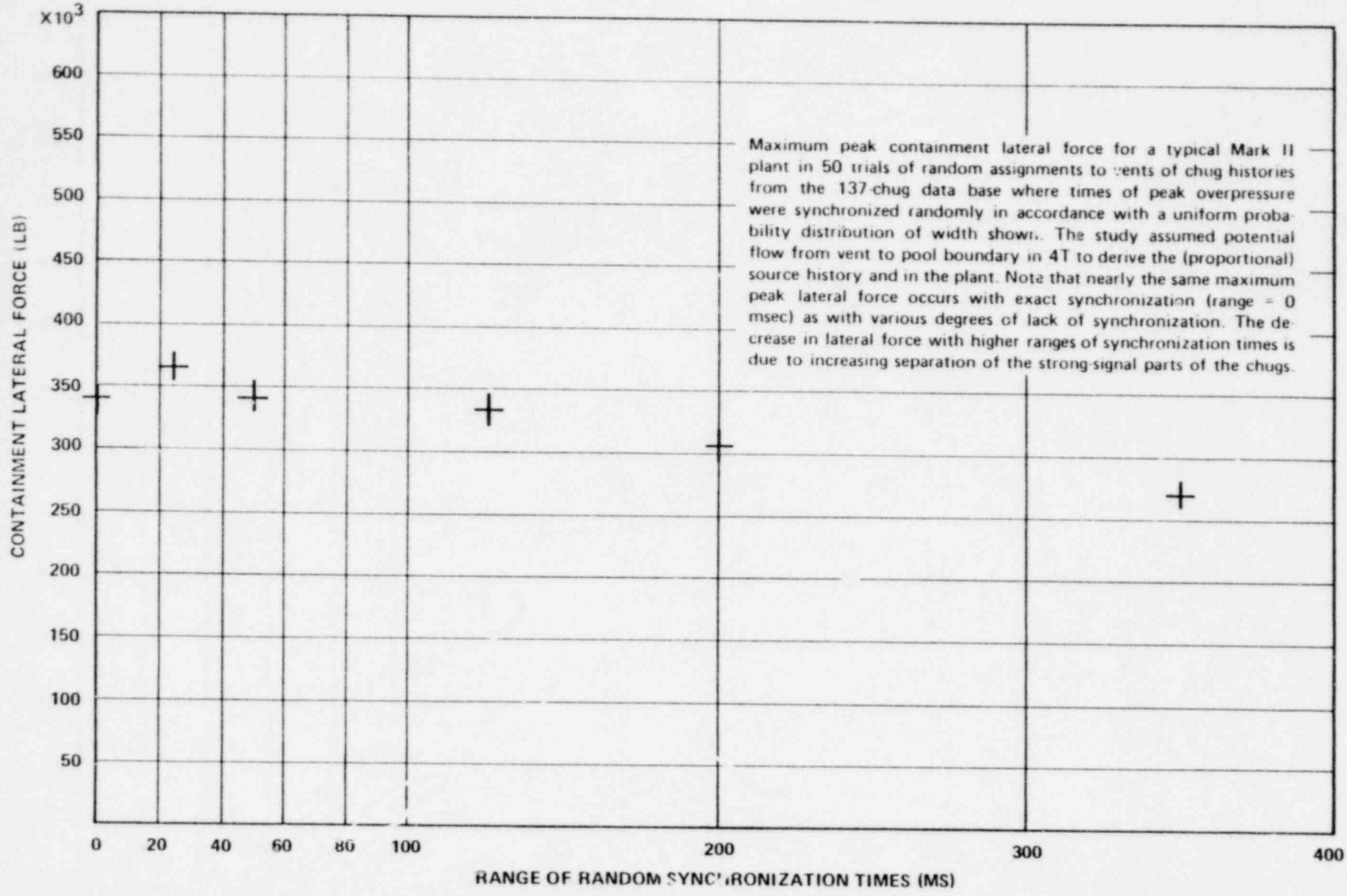

Figure 7-12 Containment Lateral Force vs Range of Random Synchronization Times

The asymmetric case criterion will be in terms of an exceedance probability of RMS-moment. The corresponding value of RMS-moment will be found on the basis that the distribution of RMS-moment is normal. This assumption is anticipated to be reasonable because, while the distribution of 4T chug RMS is skewed (long-tailed) to the right, the RMS-moment is determined by the sum of products of RMS values and moment arms, particularly moment arms to vents opposite each other and most distant from the axis of rotation. The moment arms are linear multipliers. Provisions of the central limit theorem apply. This theorem states that the distribution of the sum of several randomly chosen values from even an arbitrary distribution tends to normality as the number of values is increased and as the distribution of the underlying population of individual values is closer to normality. (The tendency of sample means from an arbitrary distribution to be normally distributed is a well-known illustration of the central limit theorem.) Thus, a value of RMS-moment chosen by normality to fulfill a criterion for exceedance probability is considered to be likely to actually have that probability in application. Even under a departure from normality, the chosen RMS-moment will have only a slightly different exceedance probability from the one in the criterion.

This concludes discussion of the assumptions in the method for the asymmetric cases. We proceed now to state the criterion, and derive the equations for calculating the two chug source strengths required.

The criterion for the asymmetric case is that a value of RMS-moment is to be found such that it is exceeded in no more than one poolwide chug per hour of chugging. With poolwide chugs assumed to occur at the same rate as in 4T, which is approximately every two seconds, the probability criterion for one per hour is 1/1800, found in one tail of the absolute-valued half-normal distribution for RMS-moment - and therefore at the 1/3600 ordinate in one tail of the complete normal distribution - which is at 3.45 standard deviations above the mean.

To find the RMS-moment corresponding to this criterion, we first require the equation for RMS-moment as a random variable so that its mean (expectation) and variance can be calculated and used to characterize its distribution.

The RMS-moment is computed by applying randomly chosen 4T BCP RMS values to the pool floor beneath each vent, as

$$M_{RMS} \equiv \sum_{i=1}^{n} L_i \, (P_{RMS})_i \qquad (7.2)$$

where

M_{RMS} = RMS-moment, kPa-m, a random variable

L_i = moment arm to centerline of i^{th} vent, positive and negative values about the axis of rotation, ft

= $R_i \cos \theta_i$ where

R_i = radius to centerline of i^{th} vent, ft

θ_i = angular location of i^{th} vent, where 0° is normal to the axis of rotation on the side having positive L_i values, as illustrated in Fig. 7-13

$(P_{RMS})_i$ = RMS at 4T BCP of chug at i^{th} vent, kPa, a random variable

n = number of vents.

Since P_{RMS} is a random variable, M_{RMS} is also a random variable taking on different values as different groups of n P_{RMS} values occur.

We require the expected value (mean) and variance of M_{RMS},

$$E[M_{RMS}] = E[P_{RMS}] \sum_{i=1}^{n} L_i, \text{ by applying the expectation operator to the } M_{RMS} \text{ equation.} \qquad (7.3)$$

= 0 if vents are symmetric about the axis, due to $\sum L_i = 0$.

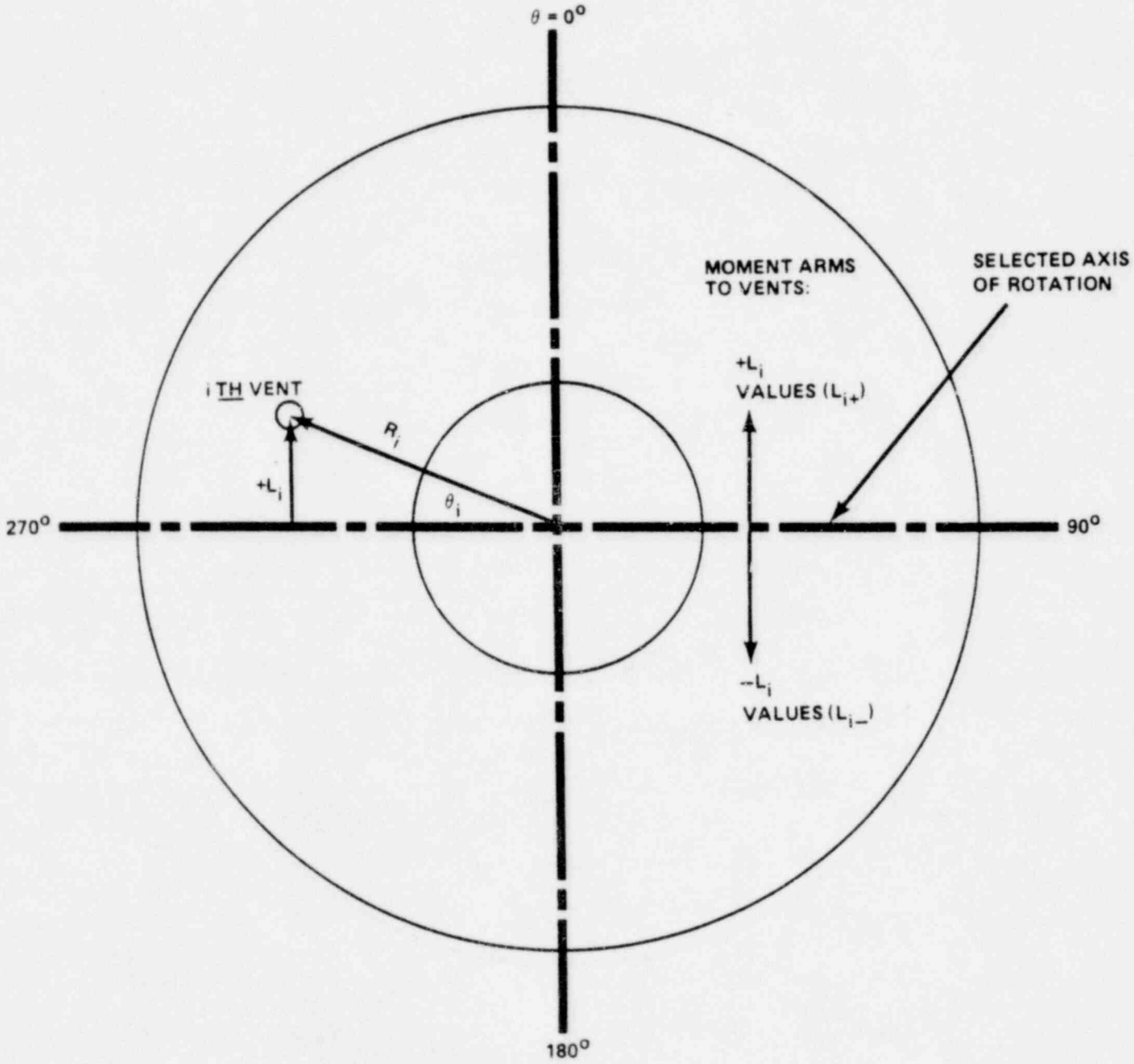

Figure 7-13 Arrangement of Values for L_i or R_i and Θ_i

$$V[M_{RMS}] = V[P_{RMS}] \sum_{i=1}^{n} L_i^2, \text{ by the propagation of errors method and independence of } P_{RMS} \text{ values among the vents.} \quad (7.4)$$

From the 137-chug data base, $E[P_{RMS}] = 9.65$ kPa (1.4 psi) and $V[P_{RMS}] = 19.02$ kPa^2 (0.4 psi^2).

Assume that M_{RMS} is normally distributed. The design value of M_{RMS}, designated M^*_{RMS}, at the upper 1/3600 point of the M_{RMS} distribution is found at 3.45 standard deviations above the mean; thus,

$$M^*_{RMS} = E[M_{RMS}] + 3.45\ (V[M_{RMS}])^{1/2} . \quad (7.5)$$

Use the positive $E[M_{RMS}]$ if it is not 0.

M^*_{RMS} can be made to occur due to a $+\Delta P_{RMS}$ applied beneath all vents on one side of the axis and $-\Delta P_{RMS}$ applied beneath all vents on the other side. ΔP_{RMS} in kPa can be computed for <u>one</u> side, on a plant-specific basis, by

$$\Delta P_{RMS} = \frac{M^*_{RMS}}{2} \quad \frac{2}{\left(\sum L_{i+} - \sum L_{i-}\right)} \quad . \quad (7.6)$$

one side, positive L_{i+} — other side, negative L_{i-}

To find the proportional basis for adjusting the source, define

$$\alpha = \frac{\Delta P_{RMS}}{P_{RMS,D.S.}} \quad (7.7)$$

where $P_{RMS,D.S.}$ ≡ the RMS of the design source at 4T BCP, kPa

$= (291.4)^{1/2} = 17.1$ kPa (2.5 psi)

Thus,

$$\alpha = \Delta P_{RMS}(kPa)/17.1 \tag{7.8}$$

and the amplitude adjustment factors on the symmetric source for a plant are $1 + \alpha$ and $1 - \alpha$.

The Mark II source used for the symmetric load case is adjusted in amplitude to obtain two new sources

$$S_1(t) = (1 + \alpha)\, S(t) \tag{7.9}$$

$$S_2(t) = (1 - \alpha)\, S(t), \tag{7.10}$$

where α is calculated as shown in Eq. (7.8). $S_1(t)$ is applied to all vents on one side of the diameter chosen as the axis of rotation, and $S_2(t)$ is applied to all vents on the other side. They are applied simultaneously.

The same considerations for calculating pool boundary forcing functions are to be made for this case as for the symmetric case.

8. APPLICATION TO THE MARK II CONTAINMENT

As discussed in Chapter 5, two equivalent methods can be used to calculate the Mark II containment response due to chugging. These methods are briefly outlined in Figs. 8-1 and 8-2.

Fig. 8-1 shows the flexible wall application method wherein the appropriate damping and corrected sonic velocity are used with the design source distribution in IWEGS/MARS to calculate the total flexible wall pressure field in the Mark II containment. The total flexible wall pressure field is then applied to a containment structural model without water for the calculation of the containment response. The sonic velocity input to IWEGS/MARS in this method is corrected from its rigid wall pure water value by use of Eq. B.1. The damping value input to IWEGS/MARS is specified by regulatory guide[54] for the type of structure under consideration (e.g., steel, reinforced concrete, prestressed concrete).

Fig. 8-2 shows the rigid wall application method wherein the appropriate sonic velocity is used with the design source distribution in IWEGS/MARS to calculate the rigid wall pressure field. The rigid-wall pressure field is then applied to a coupled fluid-structure containment model for the calculation of the containment response. The sonic velocity input to IWEGS/MARS in this method is selected from the range of values specified in Chapter 7. Eq. B.1 can be used for this calculation if the distensibility δ is set equal to zero.

Details of the selection of sonic velocity, damping, and the design source distribution are discussed in Sections 8.2, 8.3, and 8.4.

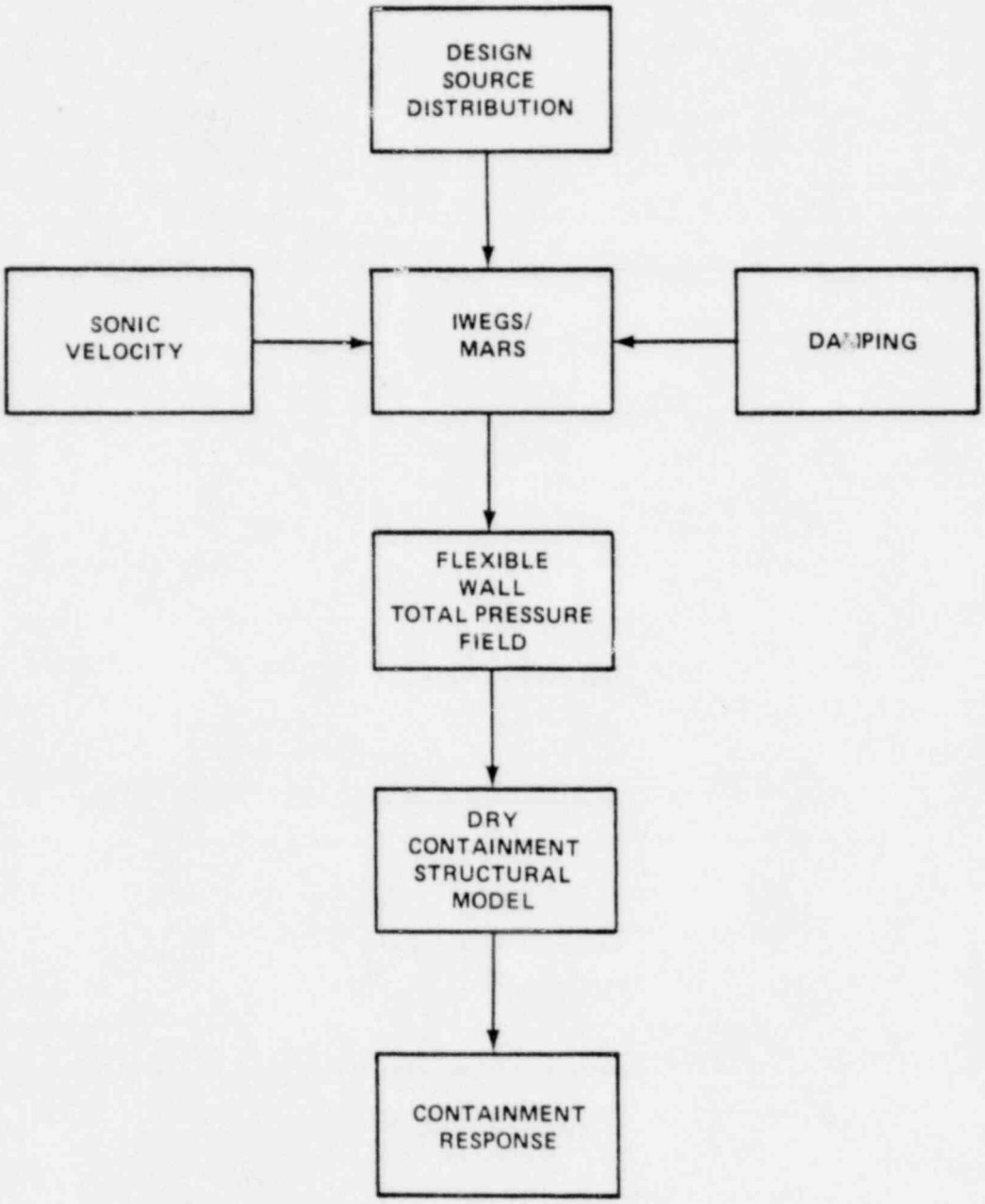

Figure 8-1 Flexible Wall Application Method

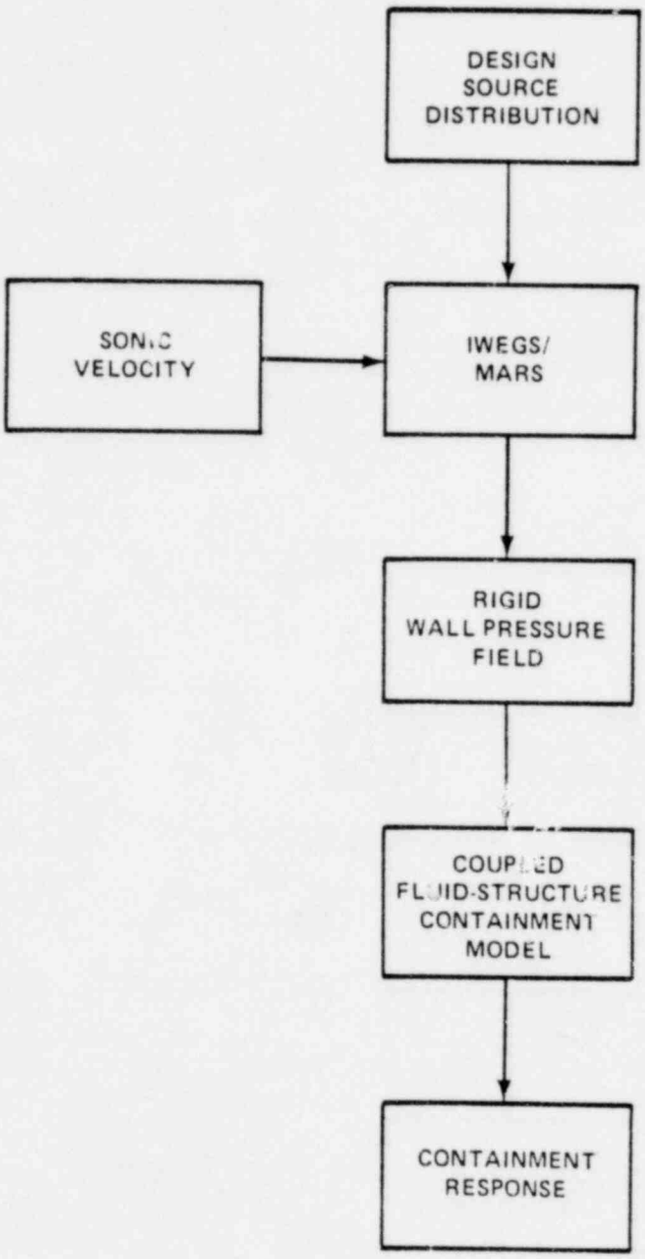

Figure 8-2 Rigid Wall Application Method

8.1 The Mark II Containment and Vent Geometry

The geometry of the Mark II containment selected for use in this sample calculation is shown in Figs. 8-3 and 8-4. The downcomers are set on four radii at approximately 15° intervals in a somewhat irregular pattern. The downcomer exits are all at the same elevation z_1 (3.65 m, 12 ft) and the pool depth, $z_1 = L$ is 7.39 m (24.25 ft). The origin of the IWEGS/MARS annular coordinate system is on the containment centerline on top of the basemat as shown in Figs. 8-3 and 8-4

8.2 Selection of Sonic Speed and Damping

The calculation of rigid wall pressure time-histories corresponding to the improved Mark II chugging methodology requires, as a parameter, the speed of sound in the suppression pool water. The characteristic vibration frequencies of the suppression pool water are directly proportional to the sonic speed. It was observed, during 4T testing, that the vibration frequency of the wetwell water generally increased over the course of a given test. This is believed to be due to the fact that air was being driven from the water with increasing water temperature. To account for this frequency shift in a Mark II analysis, it will be necessary to perform the calculations over a range of sonic speeds. Each result must then be regarded as an equally likely consequence of the chugging phase of a postulated loss of coolant accident (LOCA).

In the absence of a direct measurement of the sonic speed during the 4T tests, it is necessary to infer an appropriate range from the measured vibration frequencies of the wetwell liquid. This is done with the use of the well-known formula relating the vibration frequency to the sonic speed:

$$f = \frac{c}{4L} \tag{8.1}$$

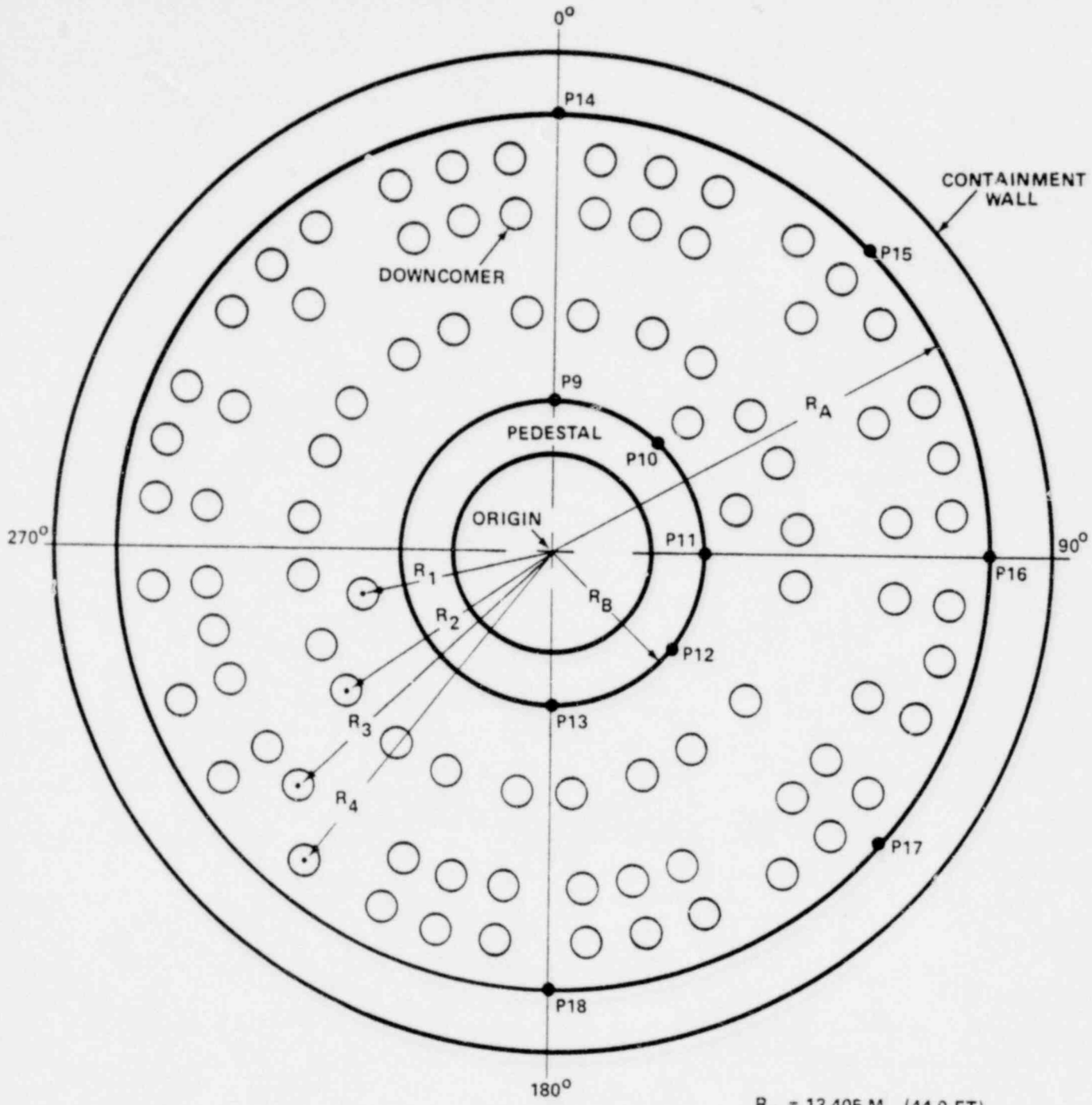

R_A = 13.405 M (44.0 FT)
R_B = 4.534 M (14.87 FT)
R_1 = 5.7912 M (19.0 FT)
R_2 = 7.4676 M (24.5 FT)
R_3 = 10.5156 M (34.5 FT)
R_4 = 12.1920 M (40.0 FT)

Figure 8-3 Sample Mark II Containment Plan View

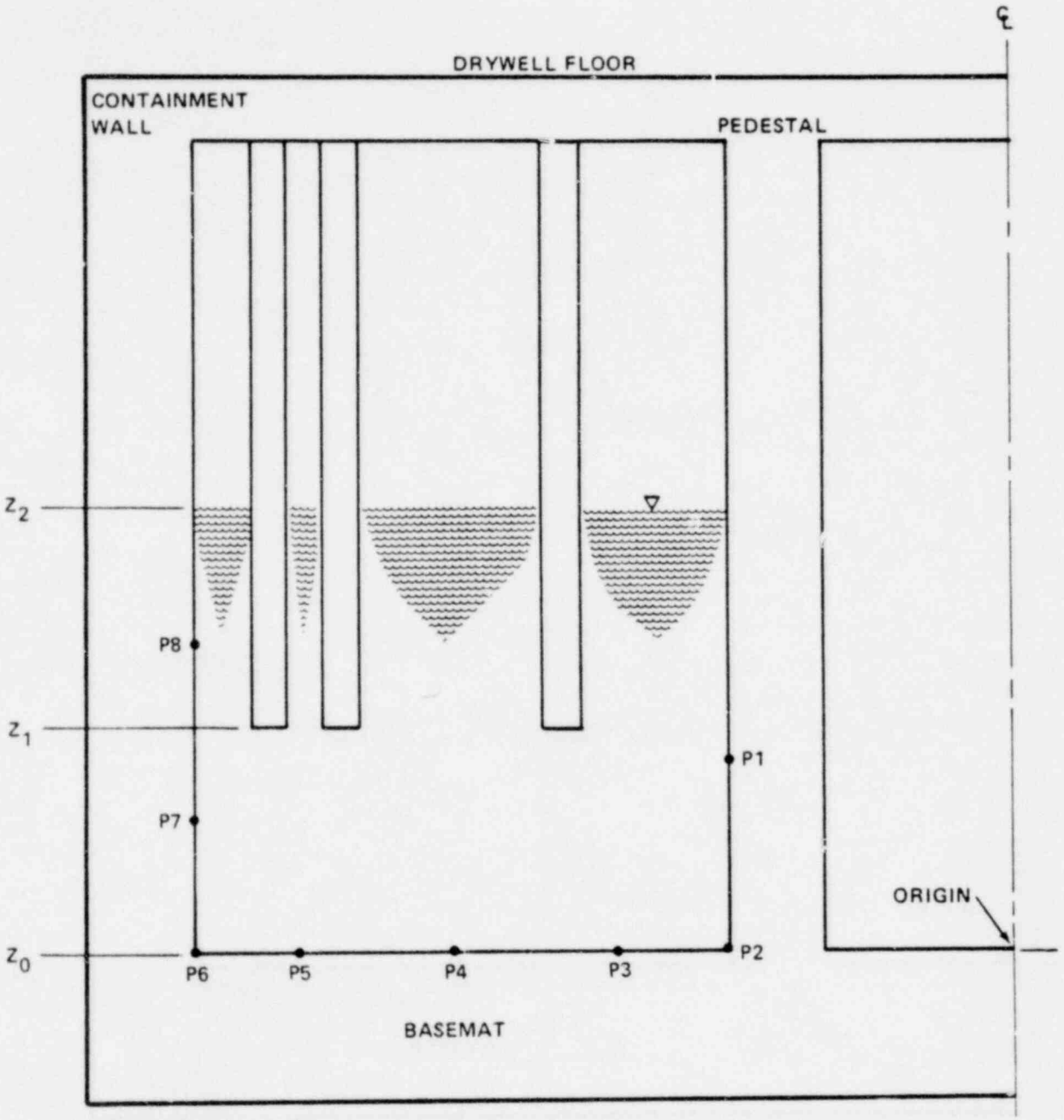

Z_0 = 0.0 m (0.0 FT)
Z_1 = 3.6576 m (12.00 FT)
Z_2 = 7.3914 m (24.25 FT)

Figure 8-4 Sample Mark II Containment Elevation View

where:

f = vibration frequency, Hz
c = sonic speed, m/s
L = water depth, m.

This formula applies to the case of one-dimensional fluid vibration in a rigid cylinder container with a free surface. A modification is required to account for the effect of container flexibility. Appendix B shows that for the 4T material and dimensions this effect reduces the frequency by 42%. Thus, for the 4T, the relationship between sonic speed and frequency becomes:

$$f = \frac{(0.58)\ c}{4L} \tag{8.2}$$

The range of sonic speeds was determined from the observed range of pool vibration frequencies for Category I and III chugs. These 39 chugs represent the fraction of the 4T data base for which the chug impulse imparted to the pool was of sufficient strength to excite its natural vibration mode.

The ringout frequency is determined to be between 17 and 27 Hz. Thus, the range of sonic speeds for chugging due to the presence of air is

$$732 \text{ m/s } (2400 \text{ fps}) \leq c \leq 1311 \text{ m/s } (4300 \text{ fps}) \tag{8.3}$$

If the method of separability is selected to assess for fluid-structure interaction (see Fig. 5-1), then IWEGS/MARS will be used to generate rigid wall pressures (p_1) and the sonic speed is to be selected from the range in Eq. (8.3). However, if IWEGS/MARS is required to generate flexible wall pressures ($p_1 + p_2$), then the range of sonic speeds in Eq. (8.3) is further modified to account for containment flexibility via

$$c' = c\sqrt{1 + \rho c^2 \delta} \tag{8.4}$$

where the distensibility δ, when multiplied by the gross supression pool volume, is the volume flexibility. The volume flexibility $V\delta$ is a measure of the increase of volume per unit pressure applied and is containment unique.

8.3 Selection of Damping Factor

As demonstrated in Chapter 5, the damping of the pressure response is essentially due to energy dissipation in the structure (see Eq. (5.28)); for design, structural damping values are specified by regulatory guide[52]. The proper damping value to be used in IWEGS/MARS depends on how the fluid-structure interaction is to be treated. Thus, two choices are possible. If IWEGS/MARS is to provide rigid wall pressures which in turn will be used as input to a suitable structural analysis model with compressible fluid elements, then of course the damping factor $\zeta \equiv \lambda_N/\omega_N = 0$. On the other hand, if IWEGS/MARS is used to provide total flexible wall pressures which are to be used in conjunction with a structural model without water, i.e., a "dry containment," then the proper damping factor to use is that which produces a damped pressure response comparable with the response generated by a fluid-structural model. For example, an impulse input to the NASTRAN Mark II model shown in Fig. 5-4 yields the flexible wall pressure response given in Fig. 5-6. The average value of the damping constant ζ given either by an average of the logarithmic decrements or exponential fits yields $\zeta = 0.093 \pm 0.005$. The value of the damping factor input to the model was 0.02 for the structure. The soil-structure interaction was considered and significantly contributed to ζ. For the following example, a nominal value of $\zeta = 0.04$ was used in IWEGS/MARS.

8.4 Calculation of the Asymmetry Factor

For design, two load cases are considered: symmetric and asymmetric. The symmetric case needs no further elaboration. However, for the asymmetric case, we obviously cannot use the same source at all vents. Instead, all sources are adjusted by the source asymmetry factor α. Given a specified vent pattern, α is calculated from Eq. (7.8). For our prototypical Mark II containment $\alpha = 0.167$. Asymmetric sources $S_1(t)$ and $S_2(t)$ are then computed via Eq. (7.9) and applied at vent locations described in Fig. 7-13.

8.5 Results

Using the design source described in Chapter 7 and the sonic velocity, damping, and asymmetry factor discussed in the previous sections, the flexible wall pressure field in the sample Mark II containment was generated.

Figs. 8-5 and 8-6 show the pressure time-histories in a radially-oriented plane at 0° for the symmetric load case. The eight pressure transients shown in these figures are for points P1 through P8 as shown in Fig. 8-4. Fig. 8-7 shows flexible wall pressure time-histories at the intersection of the containment wall and basemat at five different angles from 0° to 180° for the symmetric load case. Figure 8-8 shows five pressure time-histories at the intersection of the pedestal and basemat for angles between 0° and 180° for the symmetric load case.

As can be seen from these figures, all the pressure traces are very similar in appearance. The peak overpressure on the basemat is on the order of 20 to 28 kPa (3 to 4 psid). Peak underpressures are of a similar magnitude. Pressures near the pool surface are less than those on the basemat, as expected. Decay of pressure occurs in all the pressure traces after 0.768 sec, which is the time at which the source ceases to act. The initial portion of the pressure time-histories shows no decay. This is due to the fact that the damping constant for the vent sine waves in the design source is conservatively assumed to

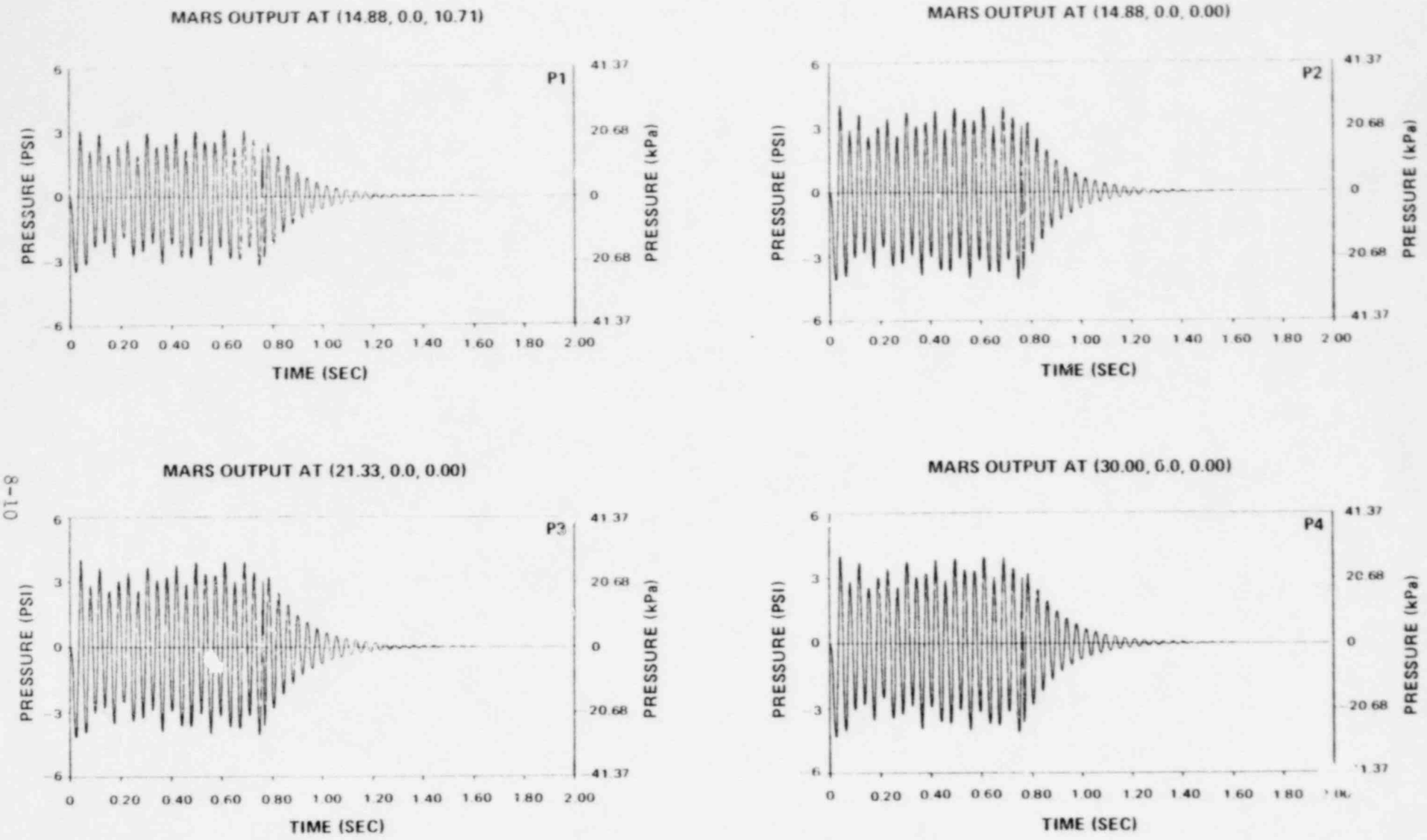

Figure 8-5 Flexible Wall Pressure Time-Histories at $\theta = 0^{o}$ - Symmetric Load Case
(See Fig. 8-4 for Location of Points)

G1002820.99

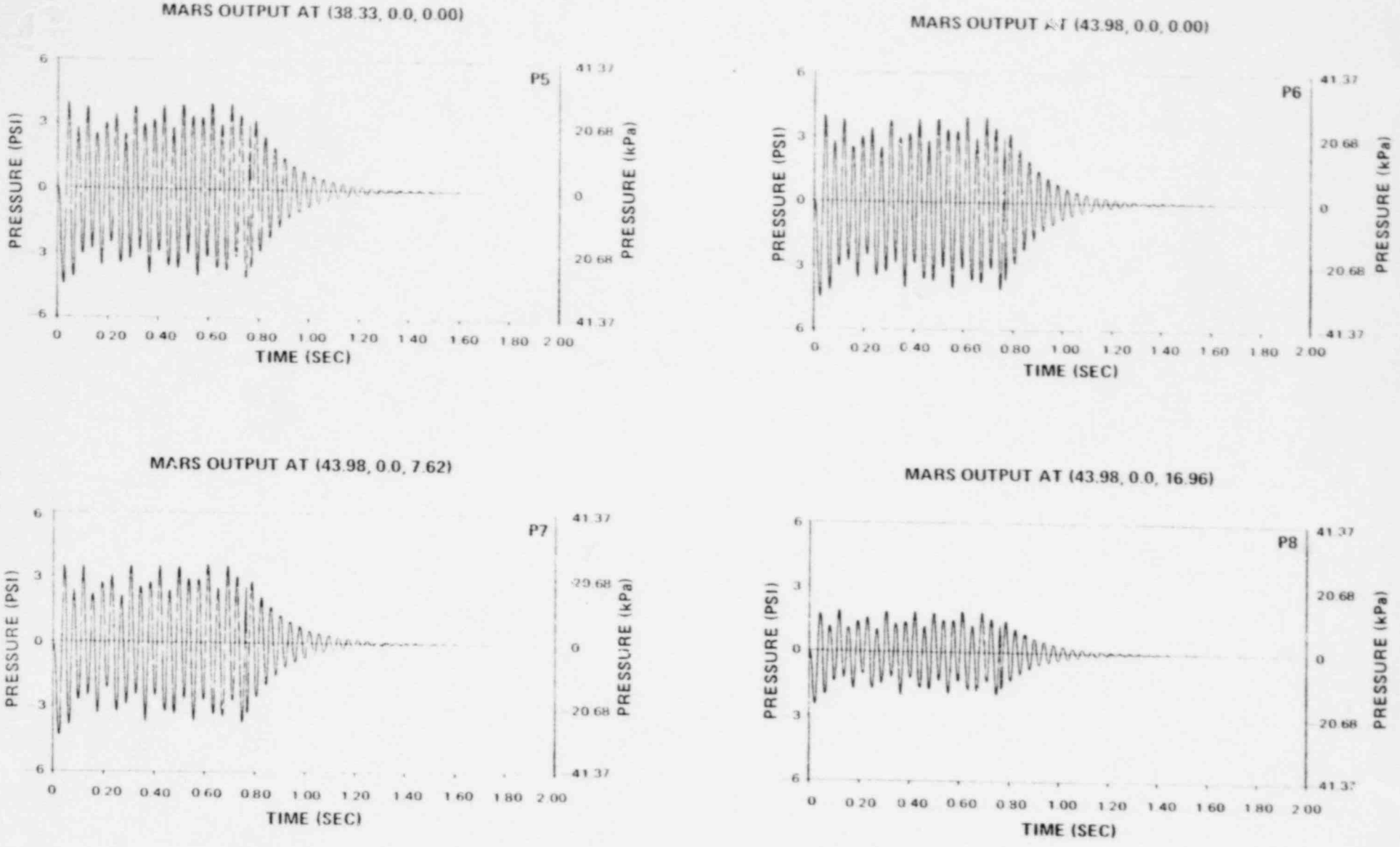

Figure 8-6 Flexible Wall Pressure Time Histories at $\theta = 0^{o}$ - Symmetric Load Case
(See Fig. 8-4 for Location of Points)

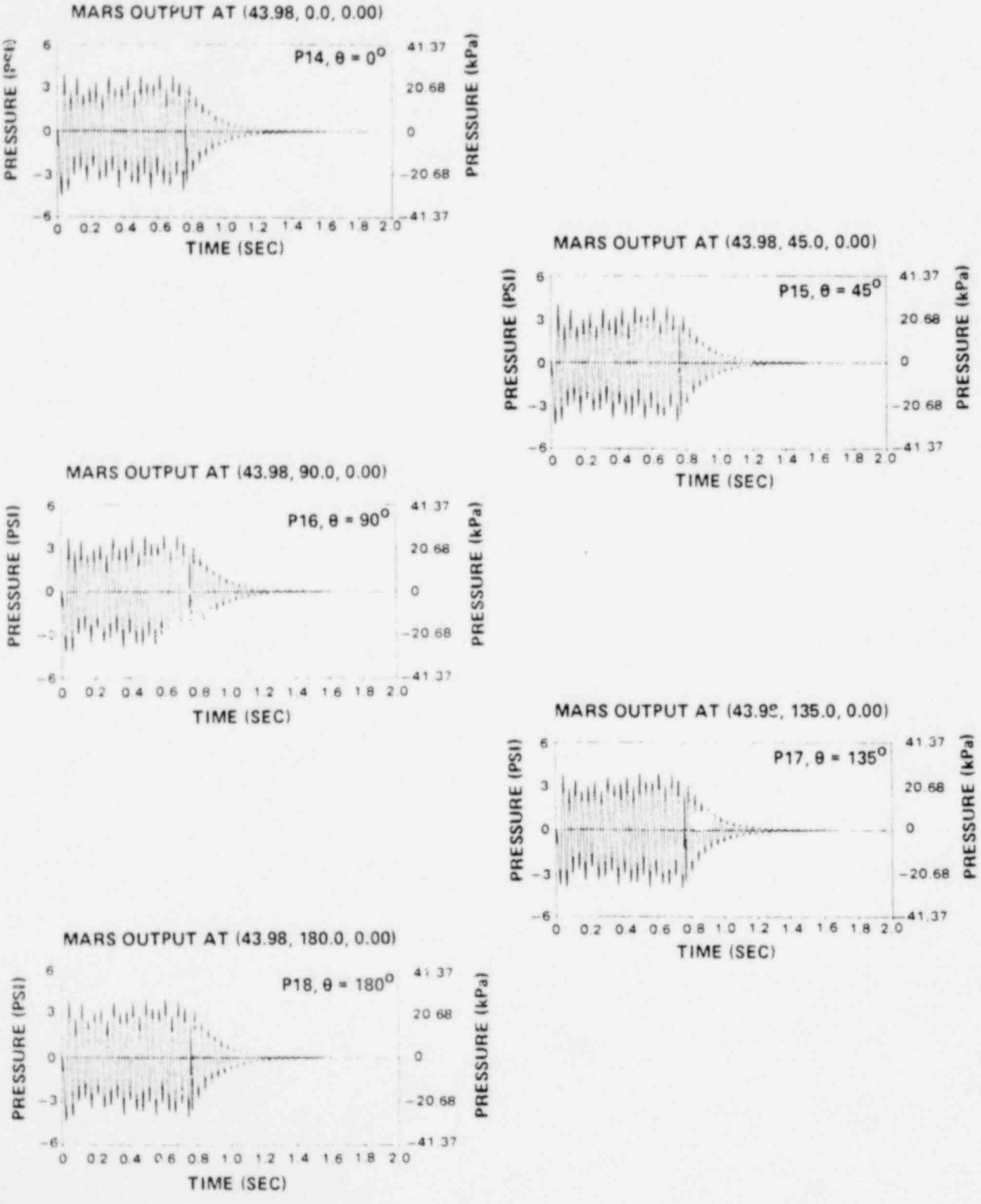

Figure 8-7 Flexible Wall Pressure Time-Histories on Containment Wall at Basemat - Symmetric Load Case (Refer to Fig. 8-3 for Location of Points)

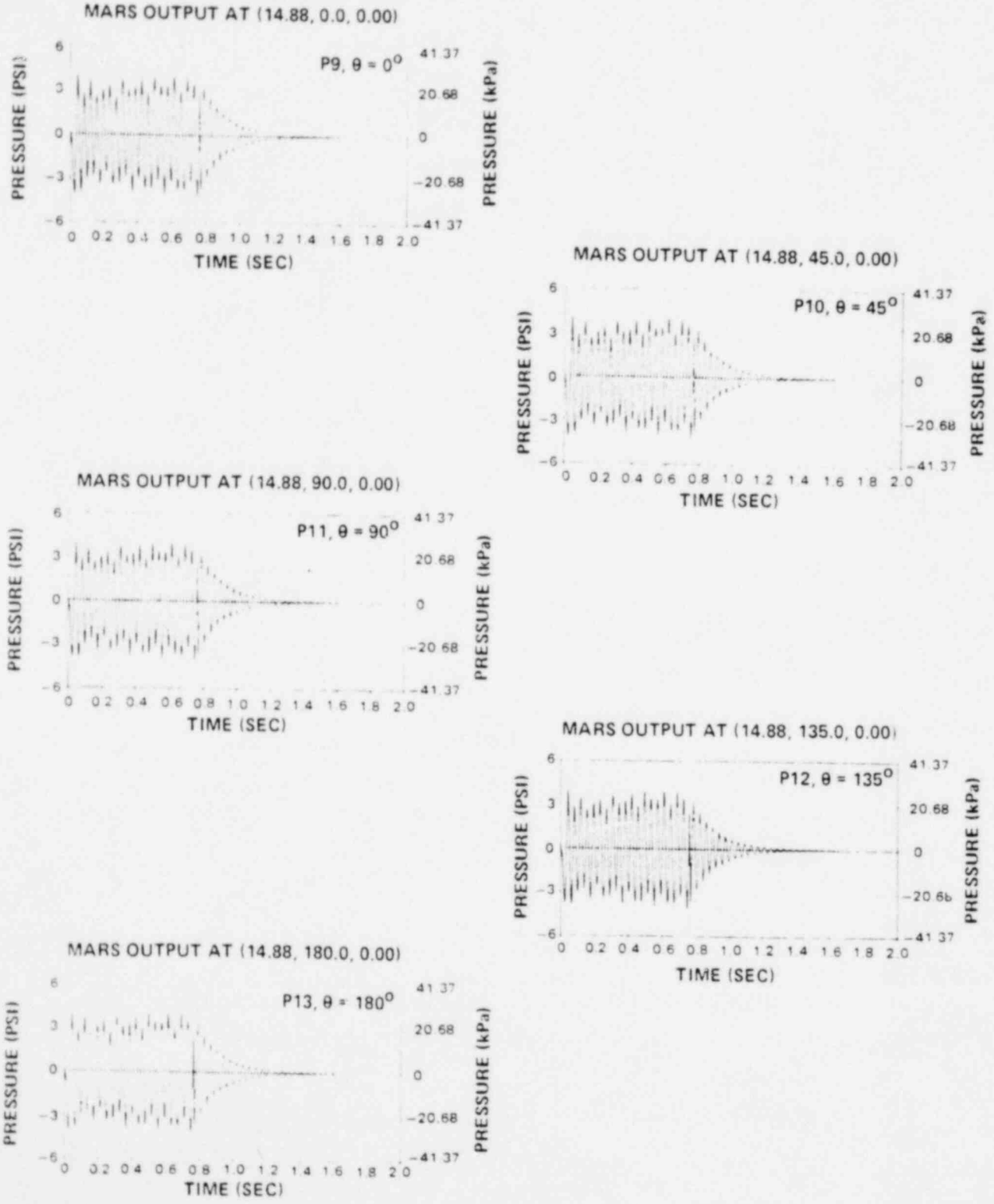

Figure 8-8 Flexible Wall Pressure Time-Histories on Pedestal at Basemat - Symmetric Load Case (Refer to Fig. 8-3 for Location of Points)

be zero. A spectral analysis of a typical flexible wall pressure time-history is shown in Fig. 8-9. Contribution from the pool axial fundamental at 25 Hz can be seen along with a contribution from the vent fundamental at 10 Hz.

Asymmetric load case results can be seen in Fig. 8-10 where flexible wall pressures at the intersection of the containment wall and basemat at 0° and 180° are shown. The pressure time-history at 0° is in the middle of the "high side" of the pool where the design source strength has been multiplied by $(1 + \alpha)$. The pressure time-history at 180° is in the middle of the "low side" of the pool where the design source has been multiplied by $(1 - \alpha)$. These two traces show that the limit of the asymmetry in the asymmetric chugging load is less than 14 kPa (2 psi). A comparison of the asymmetric load case peak overpressure and peak underpressure with the bounding load specification is shown in Fig. 8-11.

The symmetric load case flexible wall pressure field was then applied to the Mark II containment structural model shown in Fig. 8-12. This structural model is an ANSYS finite element model of a typical reinforced concrete Mark II containment. Flat shell elements are used to model the reinforced concrete containment structure and the reactor vessel. Pipe elements are used to model the columns supporting the drywell floor. The ANSYS program uses stiffness-proportional-damping. A damping value corresponding to a structural modal damping value of approximately 4% was used.

Acceleration response spectra for various important nodes in the containment are shown in Figs. 8-13 through 8-17. Results for the improved chugging load (shown as solid lines) are compared to the Dynamic Forcing Function Information Report (DFFR) bounding load (dashed lines). The four curves shown for each load definition correspond to spectral damping values of 0.5%, 1.0%, 2.0%, and 5.0%. The improved chugging load acceleration response spectra peaks are two to seven times lower than the bounding load except on the RPV in the vertical direction where they are similar to the bounding load results.

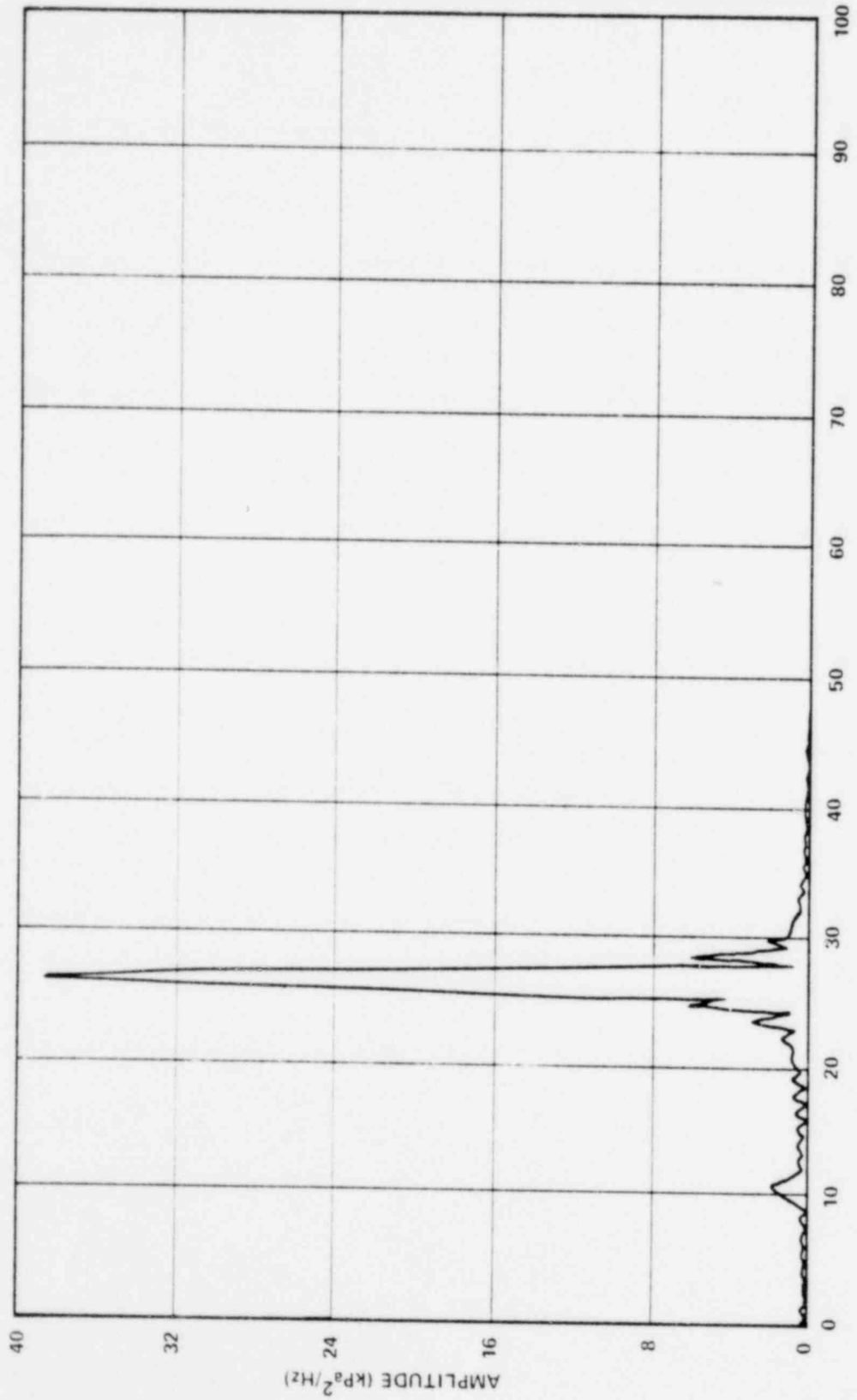

Figure 8.9 PSD of Typical Flexible Wall Pressure Time-History (Symmetric Load Case)

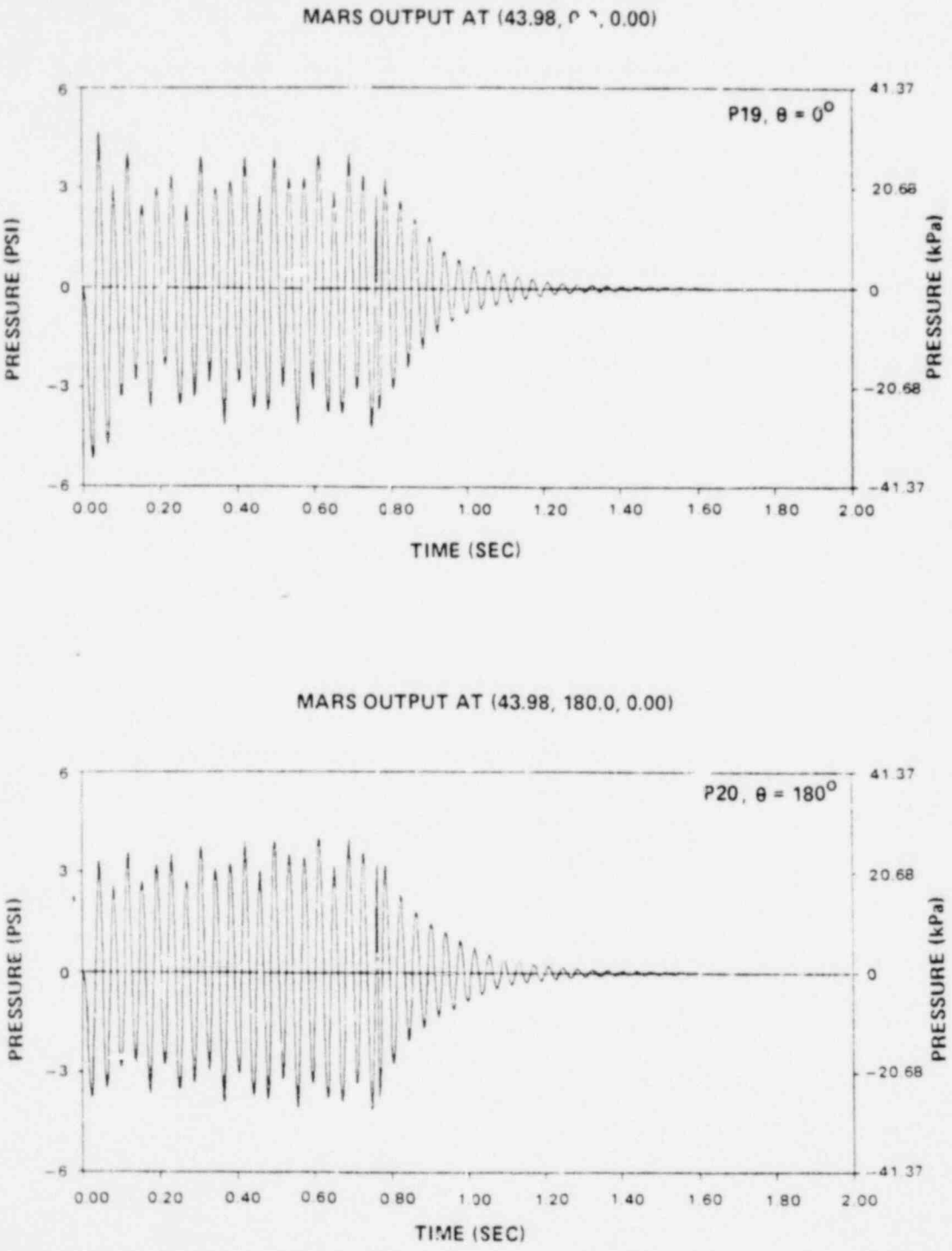

Figure 8-10 Flexible Wall Pressures at Basemat and Containment Wall - Asymmetric Load Case

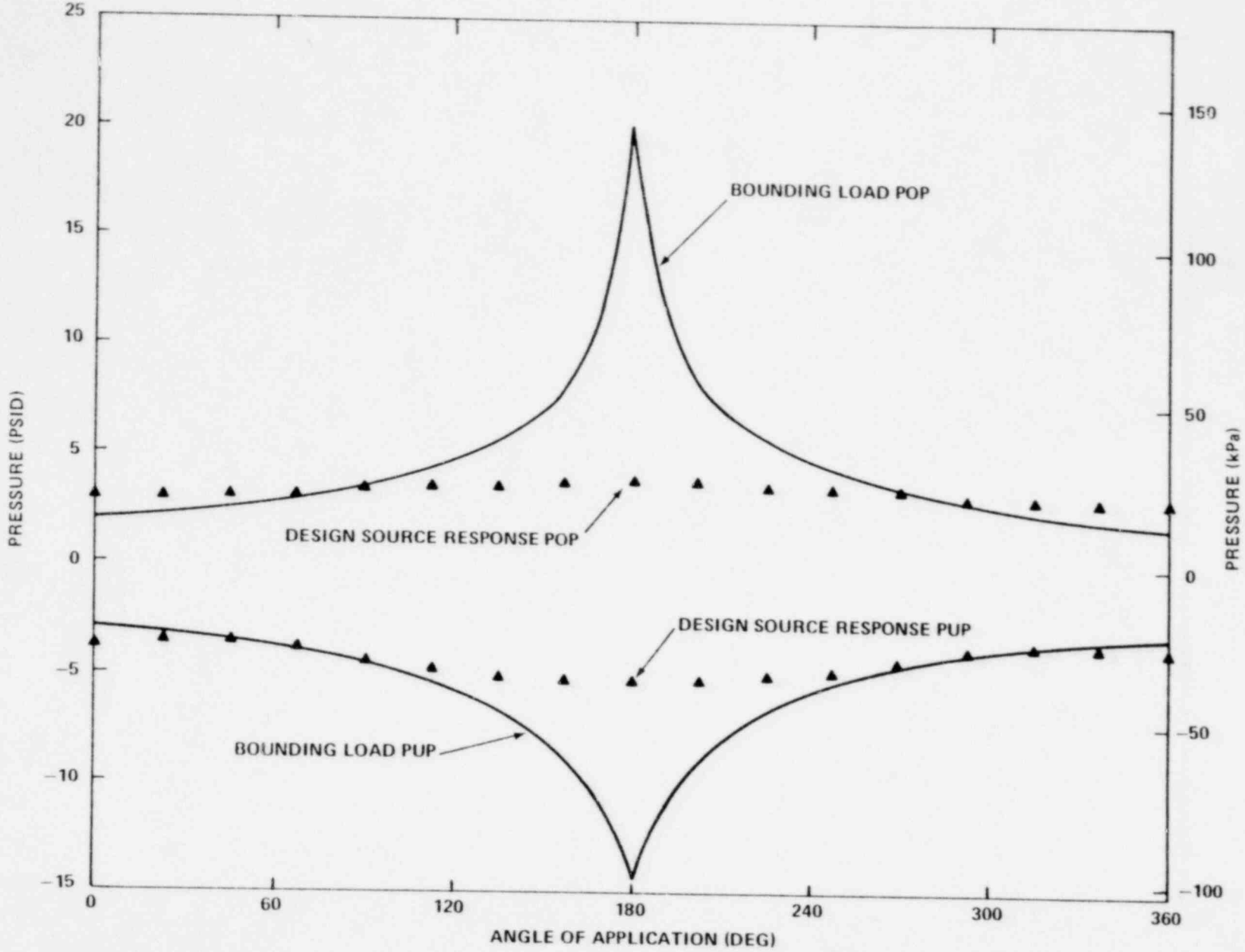

Figure 8-11 Chugging Load Profile - Asymmetric Load Case

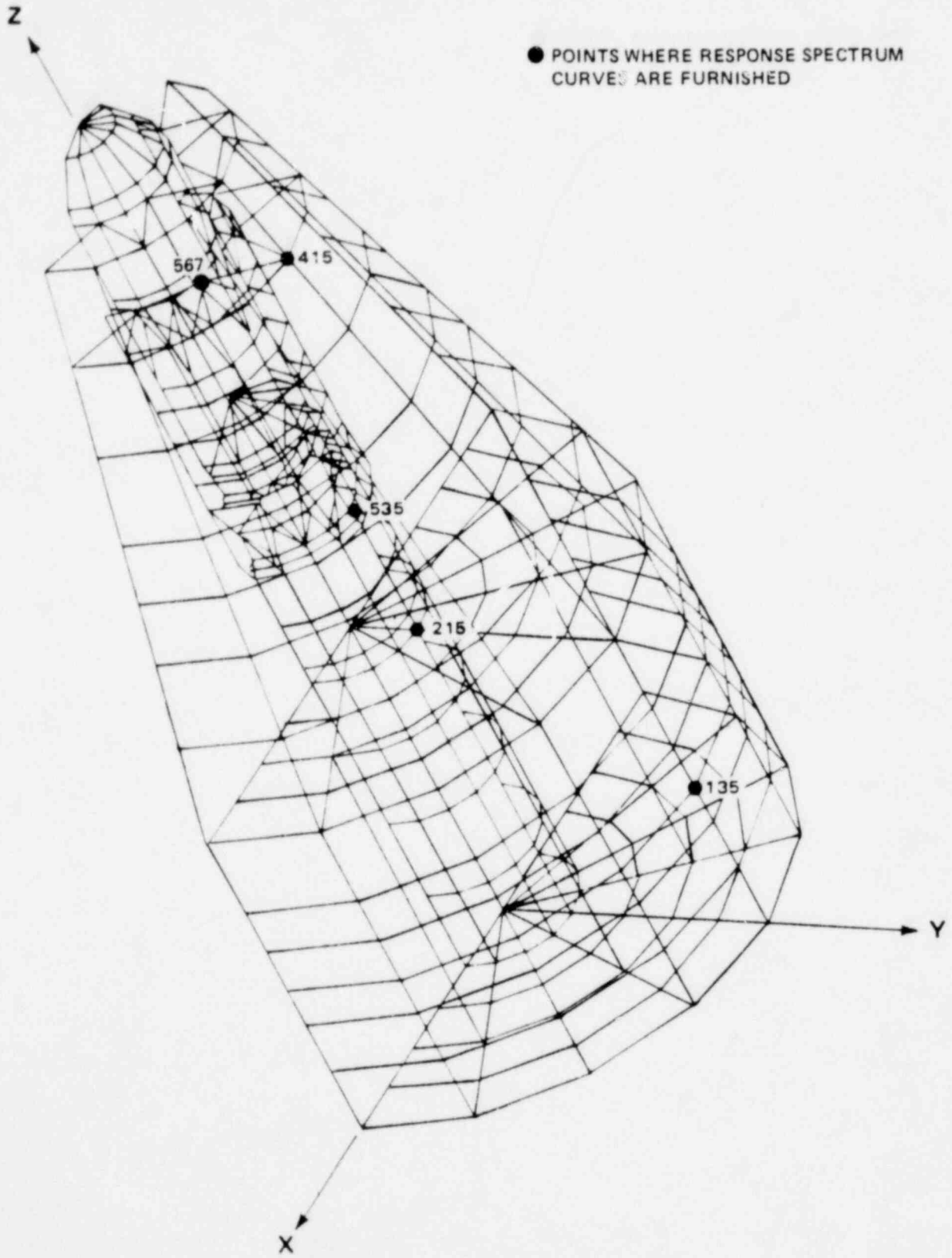

Figure 8-12 The 5 Node Points Where Broadened Acceleration Spectra Are Furnished.

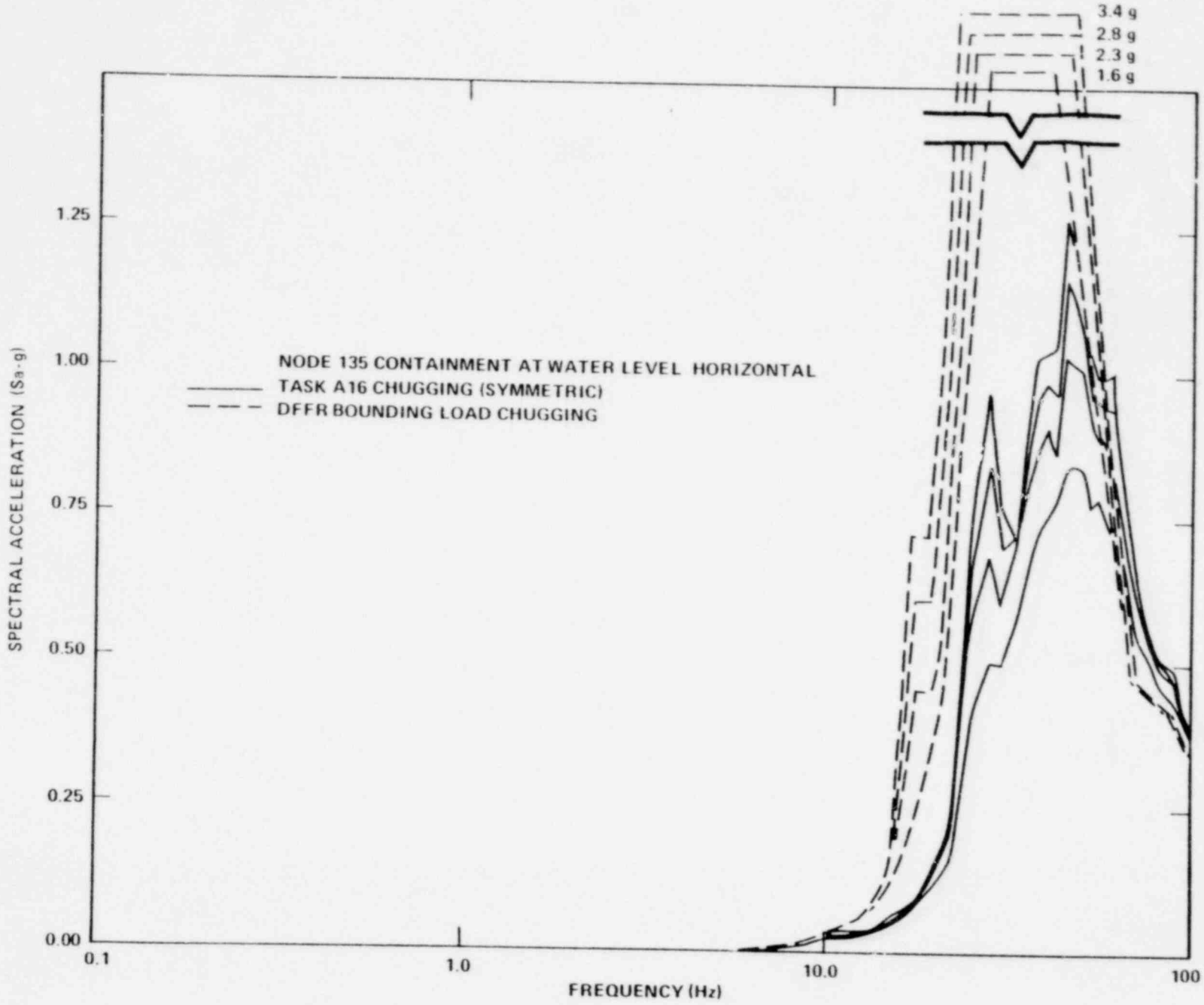

Figure 8-13 Mark II Containment Acceleration Response Spectrum

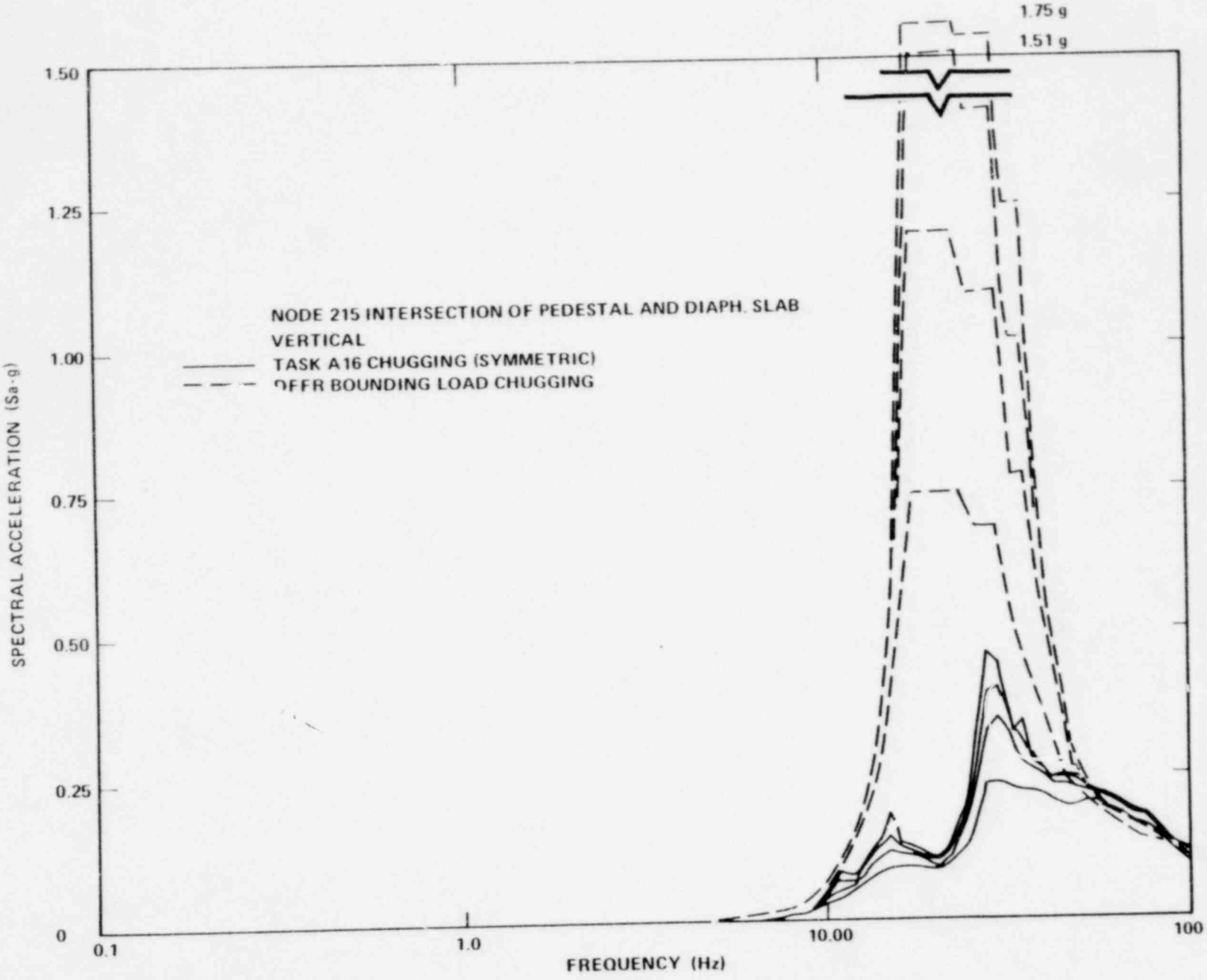

Figure 8-14 Mark II Containment Acceleration Response Spectrum

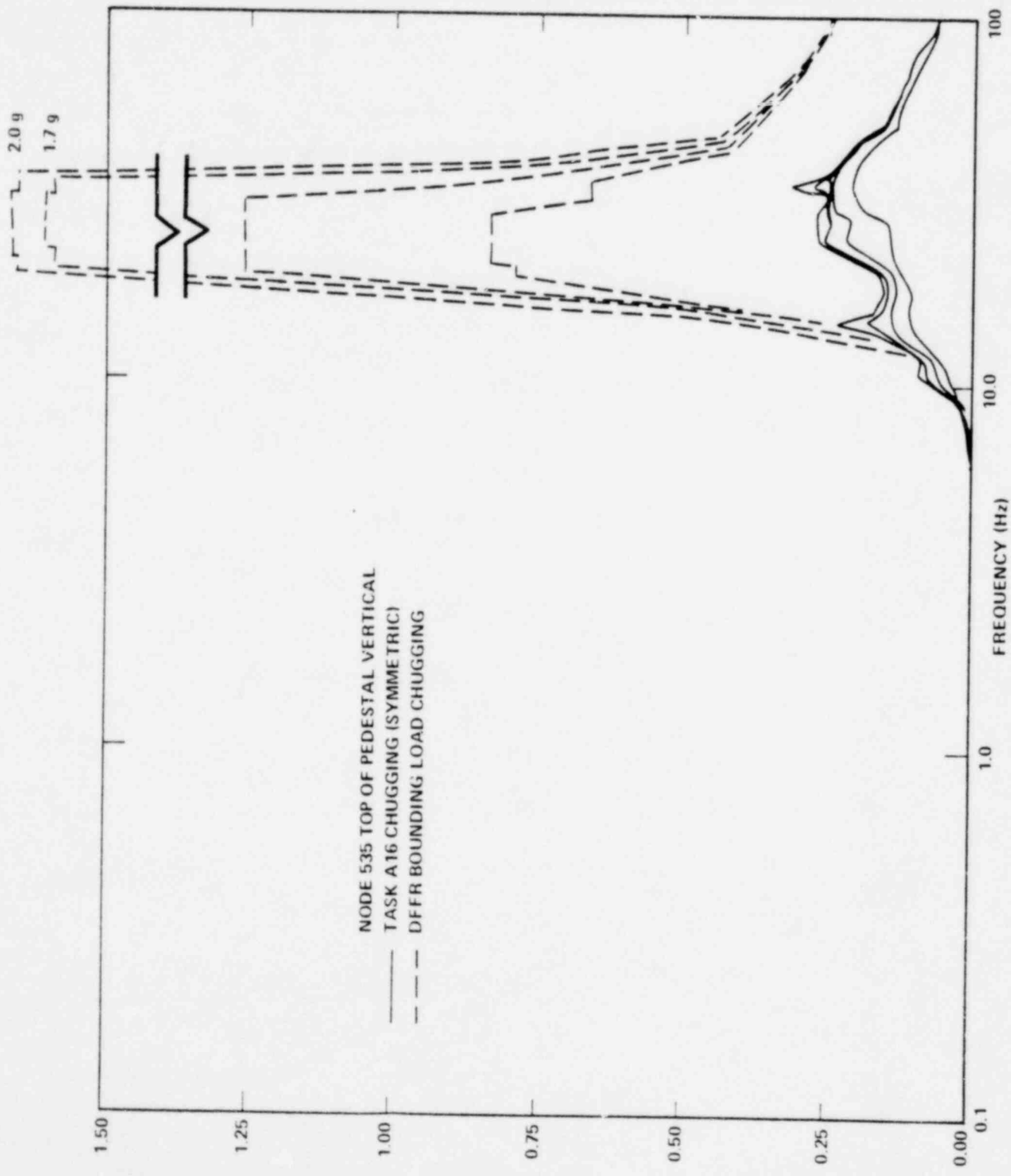

Figure 8-15 Mark II Containment Acceleration Response Spectrum

G1002820 109

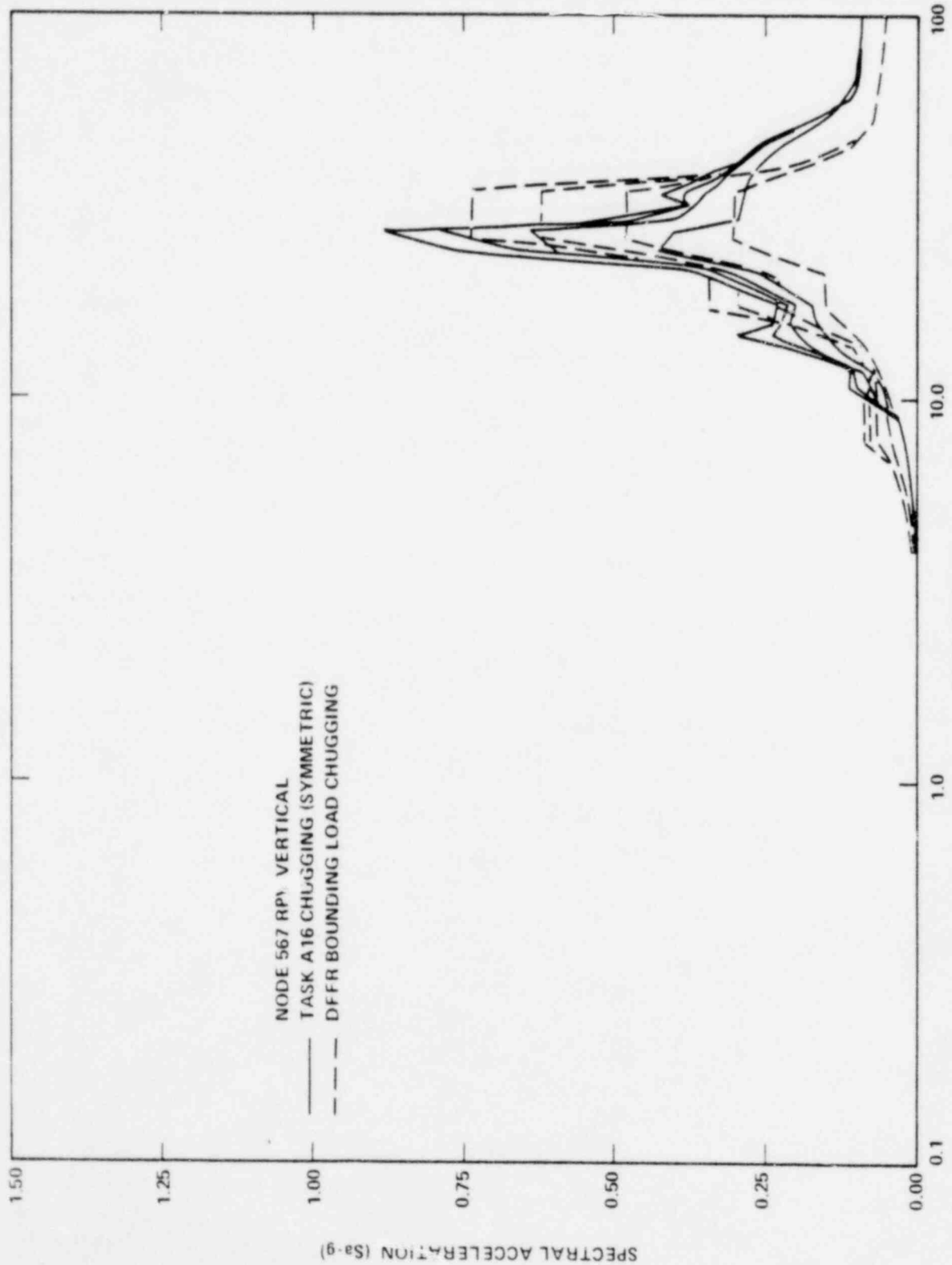

Figure 8-16 Mark II Containment Acceleration Response Spectrum

G1002820 110

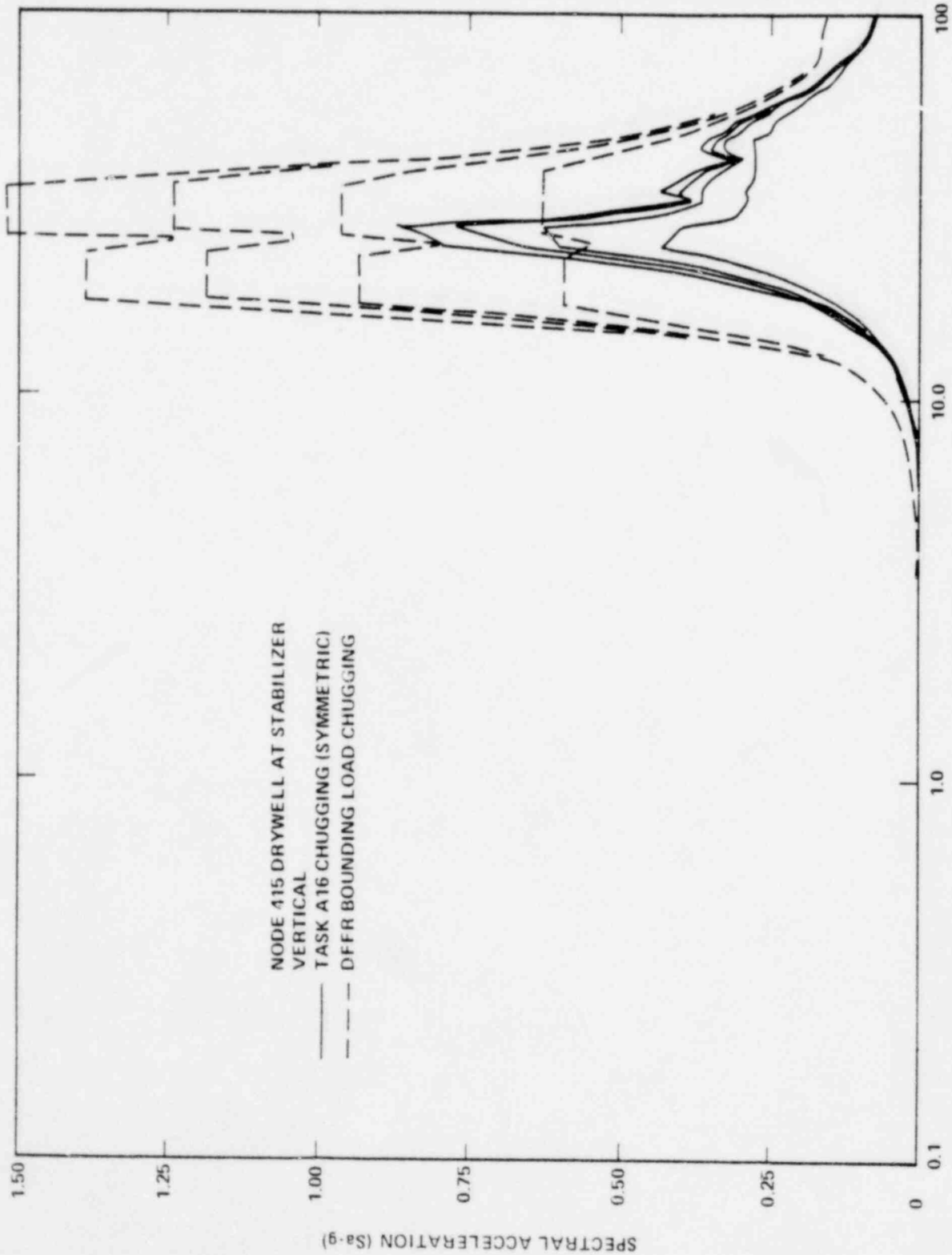

Figure 8-17 Mark II Containment Acceleration Response Spectrum

GLOSSARY OF SYMBOLS

a	Radius of 4T cylinder or outer radius of Mark II annulus
A	Cross section area (B.2)
A_n	Category I source strength term (3.2)
b	Inner radius of Mark II annulus (pedestal)
$B = \rho c^2$	Bulk modulus (Appendix B)
B_n	Category II source strength term (3.4)
c	Acoustic speed
c'	Effective acoustic speed (2.4), (Appendix B)
D	Diameter of cylindrical tank (4T)
$f = \omega/2\pi$	Frequency
g	Geometrical factor (B.8), (Table B-1)
$g(\vec{r}\|\vec{r}_o) = \frac{e^{ikR}}{R}$	Green's function for infinite space
G	General Green's function (4.2), (4.3)
G_k	Green's function for frequency $\omega/2\pi$ (4.)
h	Boundary thickness
H_ω	Transfer function (5.44)

I	A constant (5.37)
$J_m(x)$	Bessel function of order m
$J'_m(x)$	Derivative of Bessel function of order m
$k = \omega/c$	Wave number
$K_n(\omega)$	Flexible wall eigenvalue (5.3)
ℓ	Axial quantum number (see page 4-7)
L	Water depth
L^N	Spatial differential operator (3.9), (5.1)
m	Azimuthal quantum number (see page 4-7)
$M = \rho_s h$	Effective mass per unit area (5.30)
n	Radial quantum number (see page 4-7)
$n = n,m,\ell$	Quantum number trio (see page 4-7)
$N_m(x)$	Neumann function of order m
p	Acoustic pressure (3.10)
p_o	Equilibrium pressure (3.10)
P	Total pressure (3.10)
q	Chug source function
q_ω	Fourier transform of chug source function

r	Radius from origin
$\vec{r}$	Radius vector from origin
r_o	Radial position of source in 4T
r_j	Radial position of jth source in Mark II
$R = \lvert\vec{r}-\vec{r}_o\rvert$	Distance between source and observer
$R = 2\zeta_s M\omega_s$	Boundary resistance factor (5.30)
R_o	Initial void radius (3.1)
$R(t)$	Void radius (3.1)
s	Entropy per unit mass (3.7)
S	Surface area
$S(t)$	Chug source strength (3.1), (3.2), (3.4)
t	Time
T	Temperature (3.7)
T	Duration of Category II chug source (3.4)
$u(x)$	Heaviside step function
$\vec{u}$	Acoustic fluid velocity (3.5), (3.6), (3.7)
u_n	Acoustic fluid velocity normal to the boundary
V	Water volume
V_g	Noncondensible (air) volume (B.20)
V_ℓ	Liquid volume (B.20)
w	Boundary displacement (3.9)

x	Air volume fraction (B.23)
Y	Young's (elastic) modulus (Table 5-1), (B.4)
z	Elevation from origin
z_o	Axial position of source in 4T
z_j	Axial position of jth source in Mark II
$z(\omega) = p/u$	Acoustic impedance (5.30)
α_{mn}	Characteristic numbers for Bessel functions in cylindrical geometry (4.16)
$\beta(\omega,\vec{r}_s)$	Specific acoustic admittance (see page 5-6), (5.5)
$\bar{\beta}(\omega)$	Spatial average specific acoustic admittance (5.30)
γ_{mn}	Characteristic numbers for Bessel functions in annular geometry (see page 4-11)
δ	Acoustic density change (3.10)
δ	Boundary distensibility (2.4), (5.39)
$\delta(x)$	Dirac delta function (4.3)
δ_{mn}	Kronecker delta symbol (4.13)
ε_m	Normalization constant (see page 4-7)
$\zeta = \lambda_N/\omega_N$	Fluid damping factor
ζ_s	Structural damping factor
$\zeta_{mn}(r)$	Radial function for annular geometry (4.28)

η	Bulk viscosity (3.6)
η_N	Rigid wall wave number (5.12)
θ	Azimuth angle
θ_o	Azimuth angle of source in 4T (4.19)
θ_j	Azimuth angle of jth source in Mark II (4.30)
κ	Thermal conductivity
λ_N	Fluid damping constant (5.6), (5.36)
$\Lambda_n(\omega)$	Eigenfunction mean square amplitude (4.13)
$\Lambda_N^o(\omega)$	Rigid wall eigenfunction mean square amplitude (5.14)
$\Lambda(x)$	Triangular impulse function (3.3)
μ	Coefficient of shear viscosity (3.6)
μ	Poisson's ratio
$\xi(\omega,\vec{r}_s)$	Specific acoustic conductance (see page 5-6)
$\bar{\xi}(\omega)$	Spatial average specific acoustic conductance (see page 5-13), (5.33)
$\pi = 3.14159...$	Ratio of circumference to diameter of a circle
ρ	Mean fluid density
ρ_s	Mean boundary density

$\sigma(\omega,\vec{r}_s)$	Specific acoustic susceptance (see page 5-6)
$\bar{\sigma}(\omega)$	Spatial average specific acoustic susceptance (see page 5-13), (5.34)
$\vec{\tau}$	Viscous-stress tensor (3.7)
τ	Impulse duration
$\phi_n(\vec{r})$	Rigid wall eigenfunction (4.8), (4.12), (4.27)
Φ	Potential energy per unit mass (3.6)
$\Psi_n(\omega,\vec{r})$	Flexible wall eigenfuntion (5.3), (5.24), (5.25)
ω_n	Flexible wall eigenfrequency (5.6), (5.27), (5.35), (5.41)
$\omega_n^o \equiv c\eta_n$	Rigid wall eigenfrequency (5.27)
ω_b	4T base plate vibrational frequency (5.41), (Table 5-1)
ω_s	Structure vibrational frequency (5.29), (5.35)
ω_s	4T shell vibrational frequency (5.41), (Table 5-1)
$\Omega_n(\vec{r})$	Spatial factor for annular geometry (4.18), (4.33)
∇	Gradient operator
∇^2	Laplacian operator
$\Box^2$	D'Alembertian operator (4.1)
$\partial/\partial n$	Normal deviation (5.5)

REFERENCES

1. T. R. McIntyre, et al. "Mark II Pressure Suppression Test Program Phase I Tests," NEDO-13442-01, June 1976.

2. "Mark II Pressure Suppression Test Program Phases I, II, and III of the 4T Tests," Application Memorandum, January 1977.

3. W. J. Bilanin, et al, "Mark II Lead Plant Topical Report, Pool Boundary and Main Vent Chugging Loads Justification." NEDO-23617, September 1977.

4. S. A. Wilson, et al, "The Multivent Hydrodyanamic Model for Calculating Pool Blundary Loads Due to Chugging - Mark II Containments," NEDO-21669, February 1978.

5. "Mark II Containment Supporting Program. Summary of 4T Fluid-Structure Interaction Studies," NEDO-23710, September 1978.

6. P. Huber, "4T Test Facility Fluid-Structure Interaction," informal comments on the Anamet Report, August 10, 1977 (see Mk II-389E, November 7, 1977).

7. W. A. Grafton, et al.,"Mark II Pressure Suppression Test Program, Phase II and III Tests," NEDO-13468, March 1977.

8. S. T. Nomanbhoy, "Pressure Oscillations Due to Condensation of Steam in a Water Pool," NEDO-24016, June 1977.

9. J. M. Healzer, "Single Vent Chugging Model," NEDO-23703, September 1977.

10. L.W. Florscheutz and B.T. Chao, "On the Mechanics of Vapor Bubble Collapse," J Heat Transfer, May 1965, pp 209-20.

11. M.S. Plesset and S.A. Zwiek, "A Non-Steady Heat Diffusion Problem with Spherical Symmetry," J Appl Phys, Vol 23, 1952, p 95.

12. M.S. Plesset and A. Prosperetti, "Bubble Dynamics and Cavitation," Ann Rev Fluid Mech, 1977, 9:145-185.

13. H. Lamb, Hydrodynamics, sixth edition, Dover Publications, 1945, p 122.

14. J. Lighthill, Waves in Fluids, Cambridge University Press, 1978, p 87.

15. D.E. Gray, American Institute of Physics Handbook, third edition, McGraw-Hill Book Company, 1972, pp 3-44.

16. P.M. Morse and K.U. Ingard, Theoretical Acoustics, McGraw-Hill Book Company, 1968, pp 863-866.

17. P.M. Morse and K.U. Ingard, Theoretical Acoustics, McGraw-Hill Book Company, 1968, pp 270-300.

18. L.E. Kinsler and A.R. Frey, Fundamentals of Acoustics, second edition, John Wiley & Sons, 1962, Chapter 9.

19. J.J. Markham, et al, "Absorption of Sound in Fluids," Rev Mod Phys, 1951, 23, 4, 353.

20. L.D. Landau and E.M. Lifshitz, Fluid Mechanics, Addison-Wesley Publishing Co, 1959, pp 298-304.

21. D.E. Gray, American Institute of Physics Handbook, third edition, McGraw-Hill Book Company, 1972, pp 3-206-9.

22. W.C. Rivard and M.D. Torrey, "K-FIX: A Computer Program for Transient, Two-Dimensional, Two-Fluid Flow," LA-NUREG-6623, Los Alamos Scientific Laboratory, April 1977.

23. P.M. Morse and H. Feshbach, Methods of Theoretical Physics, Part 1, McGraw-Hill Book Company, 1953, pp 834-857.

24. P.M. Morse and K.U. Ingard, Theoretical Acoustics, McGraw-Hill Book Company, 1968, pp 319-322.

25. P.M. Morse and K.U. Ingard, Theoretical Acoustics, McGraw-Hill Book Company, 1968, pp 604-605.

26. P.M. Morse and H. Feshbach, Methods of Theoretical Physics, Part 1, McGraw-Hill Book Company, 1953, p 849.

27. M. Abramowitz and I. Stegun, Handbook of Mathematical Functions, AMS-55, National Bureau of Standards, June 1964.

28. H.F. Bauer, "Tables of Zeros of Cross Product Bessel Functions...," MTP-AERO-63-50, NASA George C. Marshall Space Flight Center, 1963.

29. C.W. McCormick (ed.), "MSC/NASTRAN User's Manual, Volumes I and II," Revision MSR-39, The MacNeal-Schwendler Corporation, May 1976.

30. J.A. Joseph, "MSC/NASTRAN Application Manual for CDC 7000 Series," Revision MSR-32, The MacNeal-Schwendler Corporation, May 1975.

31. _____, "CDC/NASTRAN, Supplementary Documentation, Applications Manual," Revision Q, Control Data Corporation Publication No. 86616700 (contains MSC/NASTRAN Applications Manual for CDC 6000 Series), September 1976.

32. R.H. MacNeal, "The NASTRAN Theoretical Manual (Level 15.0)," NASA Documentation No. SP-221 (01) (includes Level 15.5 Supplement), December 1972.

33. A.A. Sonin, "Rationale for a Linear Perturbation Method to Deal with the Flow Field Perturbations in Complex Fluid-Structure Interaction Problems," Massachusetts Institute of Technology, March 1979.

34. G.J. DeSalvo and J.A. Swanson, ANSYS User's Manual, Swanson Analysis Systems, Inc, August 1978.

35. P.C. Kohnke, ANSYS Theoretical Manual, Swanson Analysis Systems, Inc, November 1977.

36. G.J. DeSalvo, ANSYS Verification Manual, Swanson Analysis Systems, Inc, April 1979.

37. P.M. Morse and K.U. Ingard, Theoretical Acoustics, McGraw-Hill Book Company, 1968, p 555.

38. P.M. Morse and K.U. Ingard, Theoretical Acoustics, McGraw-Hill Book Company, 1968, pp 561-562.

39. P.M. Morse, Vibration and Sound, McGraw-Hill Book Company, 1948, pp 410-412.

40. P.M. Morse and K.U. Ingard, Theoretical Acoustics, McGraw-Hill Book Company, 1968, p 559.

41. P.M. Morse, Vibration and Sound, McGraw-Hill Book Company, 1948, p 401.

42. P.M. Morse and R.H. Holt, "Sound Waves in Rooms", Rev Mod Phys, 1944, pp 16, 69.

43. P.M. Morse and K.U. Ingard, Theoretical Acoustics, McGraw-Hill Book Company, 1968, pp 263-264.

44. E.B. Wylie and V.L. Streeter, Fluid Transients, McGraw-Hill Book Company, 1978, pp 3-8, 9-11, 19-29, 140-142.

45. P.M. Morse and K.U. Ingard, Theoretical Acoustics, McGraw-Hill Book Company, 1968, pp 475-477.

46. P.M. Morse and K.U. Ingard, Theoretical Acoustics, McGraw-Hill Book Company, 1968, pp 688-689.

47. J. Lighthill, Waves in Fluids, Cambridge University Press, 1978, p 92.

48. P.M. Morse and H. Feshbach, Methods of Theoretical Physics, McGraw-Hill Book Company, 1953, pp 1459-1462.

49. P.M. Morse, Vibration and Sound, McGraw-Hill Book Company, 1948, pp 401-412.

50. L.E. Kinsler and A.R. Frey, Fundamentals of Acoustics, second edition, John Wiley & Sons, 1962, pp 447-454.

51. P.M. Morse and K.U. Ingard, Theoretical Acoustics, McGraw-Hill Book Company, 1968, pp 579-599.

52. W.T. Thomson, Vibration Theory and Applications, Prentice-Hall, Inc, 1963, p 70.

53. N.M. Newmark and E. Rosenblueth, Fundamentals of Earthquake Engineering, Prentice-Hall, Inc, 1971, pp 420-423.

54. U.S. Atomic Energy Commission, Directorate of Regulatory Standards, Regulatory Guide 1.61, "Damping Values for Seismic Design of Nuclear Power Plants," October 1973.

55. J.D. Jackson, Classical Electrodynamics, John Wiley & Sons, 1962, pp 183-186.

56. R.N. Bracewell, The Fourier Transform and Its Applications, second edition, McGraw-Hill Book Company, 1978, pp 386-398.

Appendix A

THE 4T CHUGGING DATA BASE

Cumulative histograms of peak overpressure (POP) for the 4T data base runs are shown in Fig. A-1. A PSD for a 10-second period during chugging in 4T liquid break run 36 is shown in Fig. A-2. Comparison to the mean PSD for the 137-chug data base can be made by referring to Fig. 2-9.

The following Figures are GENERAL ELECTRIC COMPANY PROPRIETARY and have been removed from this document in their entirety.

A-1 Cumulative Probability Distributions for Peak Overpressure at Bottom-Center for Groups of 4T Runs

A-2 PSD Plot for 4T Run 36, Bottom-Center Pressure

Appendix B

ACOUSTIC SPEED REDUCTION

There are two principal factors which can have a pronounced effect on acoustic velocity and thus perturb the ringout frequency from a pure water, rigid tank c/4L value. They are:

(1) Container flexibility and
(2) Air content in the water.

In this appendix we address these factors with the ultimate intentions of understanding their influence and being able to quantitatively predict their influence on the 4T and Mark II pool ringout frequency.

B.1 Container Flexibility Effects on Ringout Frequency

The acoustic wave propagation velocity determines the ringout frequency of a chugging signal via c'/4L. A relatively exhaustive treatment of the effect of pipe wall flexibility and support on the acoustic wave propagation velocity is given in the literature[1-3].

The general equation for the speed of transmission c of an acoustic signal in a contained fluid of density ρ written in terms of compressibility is

$$\frac{1}{\rho c'^2} = \frac{1}{\rho c^2} + \delta, \qquad \text{(B.1)}$$

where the term $1/\rho c^2$ is the unbounded fluid compressibility and c the unbounded sonic velocity. The added compressibility due to motion of the containment boundaries is represented by δ which is the distensibility of the containment.

$$\delta = \frac{1}{A}\left(\frac{dA}{dp}\right)_{p=0} \simeq \frac{1}{A}\frac{\Delta A}{\Delta p} \quad . \tag{B.2}$$

Various different formulas for c result from the calculation of the term ($\Delta A/A\Delta p$) for various containment geometries. We will develop the formula for the simple case of a cylinder (pipe).

The area change for a thin walled cylinder which expands radially only is related to the elongation (strain) in the pipe wall by definition

$$\Delta\varepsilon = \frac{\Delta D}{D} = \frac{1}{2}\frac{\Delta A}{A} \quad , \tag{B.3}$$

where ε is the strain in the pipe wall and D is the diameter of the cylinder. The strain in the cylinder wall is related to the applied stress by Young's modulus, Y

$$Y = \frac{\Delta\sigma}{\Delta\varepsilon} \quad . \tag{B.4}$$

The stress σ in the pipe wall is assumed to be hoop stress only and is given by the well known formula

$$\Delta\sigma = \frac{\Delta PD}{2h} \quad , \tag{B.5}$$

where h is the cylinder wall thickness.

By combining equations (B.2), (B.3), and (B.4) we calculate

$$\frac{\Delta A}{A\Delta p} = \frac{D}{hY} \quad , \tag{B.6}$$

and the acoustic propagation velocity becomes

$$c'^2 = \frac{c^2}{1 + \rho c^2 D/hY} \quad . \tag{B.7}$$

Equations similar to (B.7) have been derived for thin and thick walled pipes for various types of pipe anchoring. All of these formulas are of the form

$$c'^2 = \frac{B/\rho}{1 + (BD/hY)g} \quad , \tag{B.8}$$

where B, the bulk modulus, is defined as $B = \rho c^2$ and g is a geometrical factor which takes on various forms depending on pipe wall thickness and pipe support.

The various forms of g taken from Reference 3 are shown in Table B-1. Formulas for circular tunnels and noncircular pipes are also given in Reference 3.

From these data we see that D/h = 134.4. Thus, the 4T tank can be considered thin walled. If we consider the tank as fixed at one end (the base plate) then,

$$g = 1 - \mu^2 = 0.92. \tag{B.9}$$

The term B/ρ is the square of the basic acoustic velocity of pure water c which, for the average pool temperature and pressure in the 4T data base tests, is taken to be

$$c = \sqrt{B/\rho} = 1524 \text{ m/s } (5000 \text{ fps}) \tag{B.10}$$

Table B-1

FORMS OF THE FUNCTION g^3

Thin Walled Pipes (D/h > 25)

1.	Anchored at upstream end only	$g = 1 - \mu/2$
2.	Anchored axially	$g = 1 - \mu^2$
3.	No axial anchoring	$g = 1$

Thick Walled Pipes (D/h < 25)

1.	Anchored at upstream end only	$g = \frac{2h}{D}(1 + \mu) + \frac{D}{D+h}(1-\frac{\mu}{2})$
2.	Anchored axially	$g = \frac{2h}{D}(1 + \mu) + \frac{D(1-\mu^2)}{D+h}$
3.	No axial anchoring	$g = \frac{2h}{D}(1 + \mu) + \frac{D}{D+h}$

μ = Poisson's ratio for the pipe wall material.

In applying the above formulas to the 4T we make use of the follcwing geometrical and material data:

$\rho = 994$ kg/m^3
$\mu = 0.28$
$D = 2.134$ m
$h = .0159$ m
$Y = 1.95 \times 10^{11}$ Pa

We calculate the reduction in acoustic wave propagation velocity due to flexibility in the 4T tank as

$$\frac{c'}{c} = [1 + (BD/hY)g]^{-1/2} = 0.64 \qquad (B.11)$$

Thus, the acoustic wave propagation velocity in the 4T tank is reduced by about 36% due to 4T wall flexibility.

The effect of the flexible 4T base plate can be estimated using a one-dimensional model originally formulated by Balsa[4]. Figure B-1 illustrates the geometry and loading of this one-dimensional model. The pressure field in the 4T tank is assumed to be axial and the base plate is represented with a spring-mass system with the same mass and natural frequency as the plate. The sides of the 4T walls are considered rigid. The correction arising from the 4T wall flexibility, calculated above, will be made by adjusting the acoustic velocity.

The governing equations and boundary conditions for the model are

$$\Box^2 p(z,t) = \left[\frac{\partial^2}{\partial z^2} - \frac{1}{c^2}\frac{\partial^2}{\partial t^2}\right] p(z,t) = 0 \qquad (B.12)$$

$$p(0,t) = 0 \qquad (B.13)$$

$$\frac{\partial}{\partial z} p(0,t) = -\rho \frac{\partial^2 w}{\partial t^2} \qquad (B.14)$$

$$\frac{\partial^2}{\partial t} w(t) + 2\zeta_s \omega_s \frac{\partial}{\partial t} w(t) + \omega_s^2 w(t) = -\frac{1}{h\rho_s} p(0,t) \ , \qquad (B.15)$$

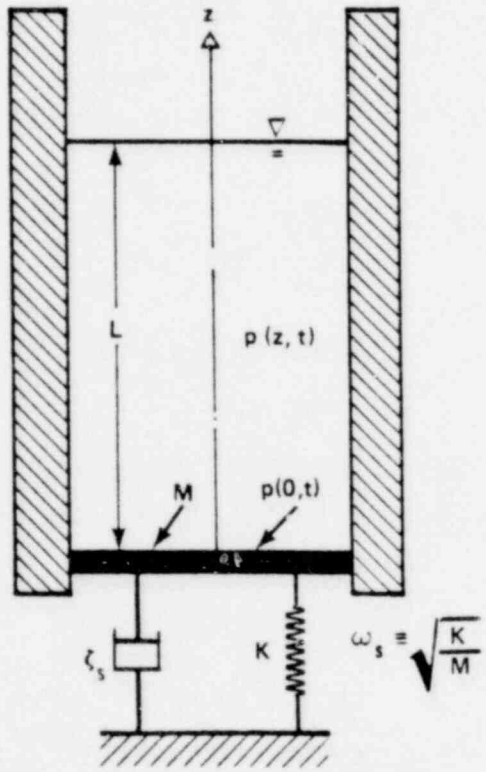

Figure B-1 Simplified 4T Model with Flexible Base

where ρ is the fluid density, ρ_s the plate density, h the plate thickness, p the fluid pressure, and w the plate displacement. For the calculation of the coupled system natural frequencies we take

$$p(z,t) = p_o \sin[\frac{\omega}{c}(L-z)]\, e^{-i\omega t} \tag{B.16}$$

and

$$w(t) = w_o e^{-i\omega t} \quad . \tag{B.17}$$

Substitution of these equations into Equations (B.13) and (B.14) yields the characteristic frequency equation

$$\tan(\frac{\omega_n L}{c}) = \frac{\rho_s h}{c\rho}[\frac{\omega_s^2}{\omega_n} - \omega_n] \tag{B.18}$$

and the system damping constant

$$\lambda_n = 2\zeta_s\omega_s\,[1+(\frac{\omega_s}{\omega_n})^2 + (\frac{\rho L}{\rho_s h})\sec^2(\frac{\omega_n L}{c})]^{-1} \quad , \tag{B.19}$$

where $\omega \equiv \omega_n - i\lambda_n$ is the complex frequency.

The base plate frequency for 4T was experimentally determined[5] to be 188.7 Hz. Thus, $\omega_s = 1185.6\ s^{-1}$. The 4T base plate thickness is 10.16 cm. For a steel density $\rho_s = 7700\ kg/m^3$ and using the value given above for ρ and c, solution of Equation (B.18) gives $\omega_n/2\pi$ = 30.8 Hz. Thus, the correction for the 4T base plate flexibility is an additional 11% reduction in the frequency corrected for wall flexibility. For a more exact correction, see Reference 4.

B.2 Effects of Entrained Air on Ringout Frequency

The propagation velocity of an acoustic wave in water can be dramatically reduced if air bubbles are dispersed throughout the liquid[6-8]. A straightforward calculation demonstrates that this is indeed true even with a small amount of air present in the form of bubbles in the liquid.

Consider the total volume V of the 4T or Mark II suppression pool fluid which can be expressed as the sum of the liquid volume V_ℓ and the air volume V_g. A change in pressure results in a volume change

$$\Delta V = \Delta V_\ell + \Delta V_g \quad . \tag{B.20}$$

The bulk modulus B of the fluid is defined by

$$B = \frac{\Delta p}{\Delta \rho / \rho} = - \frac{\Delta p}{\Delta V / V} \tag{B.21}$$

which also is valid for the liquid and air separately. Thus

$$B = \frac{B_\ell}{1 + x\,(B_\ell / B_g - 1)} \tag{B.22}$$

where $x = V_g/V$ is the air volume fraction. The mixture density ρ in terms of the liquid and air densities is

$$\rho = x\,\rho_g + (1-x)\rho_\ell \quad . \tag{B.23}$$

Substitution of Eqs. (B.22) and (B.23) into Eq. (B.8) yields the acoustic wave speed as a function of wall flexibility and air volume fraction

$$c' = c\,\{[x(\frac{\rho_g}{\rho_\ell} - 1) + 1][1 + x\,(\frac{\rho_\ell c^2}{p} - 1) + \rho_\ell \frac{c^2 D}{hY}\, g]\}^{-1/2} \tag{B.24}$$

where the air bubbles are considered to compress isothermally such that $p = B_g$. Comparison of Eq. (B.24) with experimental data is shown in Fig. B-2. The minimum acoustic propagation velocity in bubbly air-water mixtures can be as low as 70 fps for a void fraction of 0.5. While the test conditions existing in the 4T tank had much smaller air contents than this, a substantial reduction in the acoustic velocity is still possible.

It is possible to estimate the amount of air present in the 4T pool during the chugging tests by comparing the observed pool fundamental frequency to its pure water, rigid tank value. For pure water in a rigid 4T tank the fundamental frequency is $f_o = c/4L = 54$ Hz.

If we account for flexibility in the 4T tank, then this fundamental ringout frequency is reduced by factors of 0.64 and 0.89 to 30.8 Hz. The average pool fundamental ringout frequency for the 14 Category I chugs was 21.7 ± 3.6 Hz during the 4T chugging tests. This implies an air reduction factor for frequency (and acoustic velocity) of

$$\frac{21.7 \pm 3.6}{30.8} = 0.70 \pm 0.12 \quad . \tag{B.25}$$

Mark III tests[9] showed an acoustic velocity of 1018 m/s (3340 fps). Ignoring the small PSTF flexibility correction, this acoustic velocity implies an air reduction factor of 0.69 which agrees favorably with the 0.70 reduction observed in the 4T tests.

From Figure B-2 one can calculate that air content reduction factors in the range 0.69 to 0.70 imply air content in the water of 0.06% to 0.07% by volume. Allowing for the fact that flexibility has been ignored, this amount of air is too large but consistent with an air fraction 0.04% which would be required for Eq. (B.24) to yield a speed of sound c' such that $c'/4L = 21.7$ Hz.

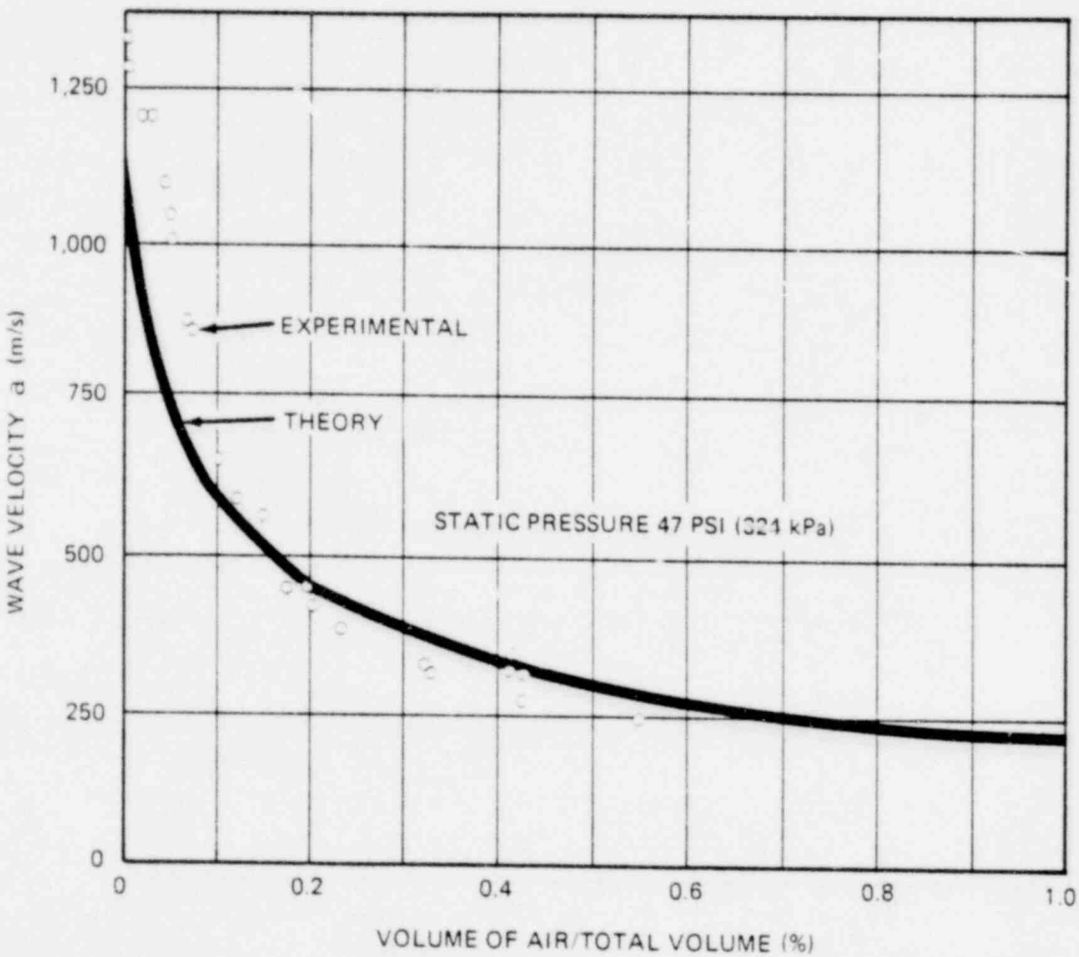

Figure B-2 Propagation Velocity (a) of a Pressure Wave in Pipeline for Varying Air Content (Theoretical and Experimental Results)*

*Taken from Reference 6

REFERENCES

1. P.M. Morse and K.U. Ingard, Theoretical Acoustics, McGraw-Hill Book Company, 1968, pp 475-477.

2. J.S. Lighthill, Waves In Fluids, Cambridge University Press, 1978, pp 89-99.

3. E.B. Wylie and V.L. Streeter, Fluid Transients, McGraw-Hill Book Company, 1978, pp 3-8, 19-29, 140-142.

4. "Mark II Containment Supporting Program, Summary of 4T Fluid-Structure Interaction Studies,"NEDO-23710, September 1978.

5. "Mark II Containment Supporting Program, Summary of 4T Fluid-Structure Interaction Studies," NEDO-23710, September 1978.

6. E.B. Wylie and V.L. Streeter, Fluid Transients, McGraw-Hill Book Company, 1978. pp 19-29.

7. G.B. Wallis, One-Dimensional Two-Phase Flow, McGraw-Hill Book Company, 1969, pp 25, 143-144, 266.

8. S.W. Gouse, Jr., and G.A. Brown, "A Survey of the Velocity of Sound in Two-Phase Mixtures," E.P.L. Report DSR 8040-1, Massachusetts Institute of Technology, April 1963.

9. A. M. Varzaly, W. A. Grafton, and D. S. Seely, "Mark III Confirmatory Test Program Full Scale Condensation Strafification Phenomena Test Series 5707," NEDO-21853, August 1978.

Appendix C

FLUID-STRUCTURE INTERACTION SEPARABILITY THEOREM

This appendix contains Ain A. Sonin's complete paper entitled "Rationale for a Linear Perturbation Method to Deal with the Flow Field Perturbations in Complex Fluid-Structure Interaction Problems," dated March 1979. The theory in this paper constitutes one of the two ways fluid-structure interaction is incorporated into the chugging methodology.

NEDO-24822

RATIONALE FOR A LINEAR PERTURBATION METHOD TO DEAL WITH THE FLOW FIELD PERTURBATIONS IN COMPLEX FLUID-STRUCTURE INTRACTION PROBLEMS

Ain A. Sonin

Department of Mechanical Engineering
Massachusetts Institute of Technology
Cambridge, Massachusetts 02139

PROGRESS REPORT
March 1979

on work sponsored by the
U.S. Nuclear Regulatory Commission,
Office of Nuclear Regulatory Research
under contract number NRC-04-77-011.

RATIONALE FOR A LINEAR PERTURBATION METHOD TO DEAL WITH THE FLOW FIELD PERTURBATIONS IN COMPLEX FLUID-STRUCTURE INTRACTION PROBLEMS*

Ain A. Sonin

Department of Mechanical Engineering
Massachusetts Institute of Technology
Cambridge, Ma. 02139

ABSTRACT

A formal justification is developed for a method in which hydrodynamic data for a transient in a rigid-wall system (derived, for example, from a small-scale experimental simulation) is used as input in a linear computation for the perturbation flow field due to actual wall flexibility. The method is useful in problems where the basic flow transient is so complex that it can be quantified only empirically, and where the fluid-structure interaction is too complex for the fluid side to be represented by an à priori defined equivalent mass.

* Work supported by the U.S. Nuclear Regulatory Commission, Office of Nuclear Regulatory Research, Division of Reactor Safety Research, under Contract No. NRC-04-77-011.

1. INTRODUCTION

The analysis of loads resulting from complex flow transients in vessels is often further complicated by the effects of elastic boundaries. Numerical methods are almost invariably required, and even so, only relatively simple problems can be solved practicably [1]. The purpose of this paper is to identify a class of such problems where it is useful to separate the flow field into a component which would result if the walls were perfectly rigid, and a perturbation which arises because of wall flexibility. We will show rigorously that the effects of the wall flexibility can be derived separatley by means of a perturbation analysis which in most cases is considerably simpler than the general problem. The pressure of the rigid-wall flow field appears as a forcing function at the boundary of the perturbation flow field.

This result is useful in two ways. First, it simplifies analysis. The calculation for the flow transient with assumed rigid boundaries can be done first and the additional effects of wall flexure can be derived by a separate perturbation calculation in which the fluid behaves linearly.

The second utility of our result arises in cases where the flow transient is so complex that a computation for it, or for its rigid-wall component, is difficult or impossible. In such cases, the first calculation can be replaced by experimental data for a small-scale simulation using rigid walls. Our analysis provides a formal justification for a method of using such data as

input in a relatively simple calculation for the perturbation caused by wall flexibility. Such a combined empirical/analytical approach is often more practical than a complete empirical simulation which includes both the effects of wall flexure and the fluid dynamic transient proper.

The technique of applying the experimental rigid-system load as a forcing function to compute structural oscillations has been used widely to solve problems involving flow-induced vibrations of cylinders and similar structures [2]. In those applications, the question of how one deals with the inertially induced pressure field in the fluid is resolved simply by introducing an equivalent mass, one which can be determined semi-empirically for a given body geometry. The method we propose here is useful in more complex problems where an equivalent water mass cannot be specified à priori, and where a solution must be derived for the flow field perturbation which results from wall flexibility.

The mehtod suggested here is not novel. Bedrosian [3], for example, has applied essentially this method to compute the fluid-structure interaction effects in pressure-suppression containment vessels of boiling-water reactors. The purpose of the present paper is to give the method a formal basis, and to specify the conditions which must be satisfied if it is to be valid.

2. ANALYSIS

We consider a class of problems where an essentially inviscid motion is induced in a liquid by the transient application of pressure at one or several of the places where the liquid is bounded by gas. Elsewhere, the liquid is bounded by solid, but flexible, walls. The general case is best illustrated with an example (Figure 1).

A vertical pipe is partially submerged in a liquid pool which is initially at rest, and bounded above by a region of gas. An event is triggered by a sudden discharge of gas or vapor into the pipe from above, causing the clearing of the liquid from the pipe, the formation of a gas bubble at the pipe end, and the rise or oscillation of the liquid in the pool. If the pool boundaries are rigid, the resulting pressure history at some point on the pool floor, for example, might be the one sketched in Figure 2. If the boundaries are elastic, they, and together with them the pool, would be set into oscillation, and the resulting pool acceleration and deceleration would give rise to an additional oscillatory component of pressure, as indicated on the figure. We aim to show how these two contribution to the pressure can be separated.

The liquid dynamics in governed by the equation of motion,

$$\rho \left(\frac{\partial \vec{v}}{\partial t} + \vec{v} \cdot \nabla \vec{v} \right) = -\nabla p - \rho g \nabla z , \qquad (1)$$

the equation of mass conservation,

$$\frac{\partial \rho}{\partial t} + \nabla \cdot (\rho \vec{v}) = 0 \qquad (2)$$

and the isentropic pressure-density relation, $dp/d\rho = c^2$. We shall assume that the latter applies in the linear approximation,

$$p - p_o = c_o^2 (\rho - \rho_o) \qquad (3)$$

where p_o, c_o, and ρ_o are the pressure, speed of sound and density, respectively, in the undisturbed fluid.

The boundary conditions must be specified for Eqs. 1 - 3 at the free surfaces and at the solid walls. We assume that the pressure at any free surface is uniform and, for the purposes of the analysis of the liquid, given. In Figure 1, the trapped gaseous space above the liquid is one free surface, and the bubble emerging from the pipe is another. The free-surface boundary condition can thus be express as

$$p = p_i(t) \quad \text{at the i'th free surface .} \qquad (4)$$

At the flexible solid walls one must apply a boundary condition like

$$v_\perp = \frac{dx}{dt} \qquad (5)$$

where $v_\perp$ is the fluid velocity component directed perpendicularly into the wall, and x is the displacement of the wall (away from the fluid) from its initial, equilibrium position under hydrostatic conditions. The wall displacement x is governed by a structural equation of motion which can be expressed symbolically as

$$m \frac{d^2x}{dt^2} = (p - p_o) - \sigma \left(x, \frac{dx}{dt}, \frac{d^2x}{dt^2}, \ldots, t\right) \qquad (6)$$

where m is the local mass of the wall per unit area, p is the local instantaneous pressure in the fluid, p_o is the initial hydrostatic pressure, and σ is a local structural restraining force per unit area, whose magnitude depends on the displacement x of the wall from its initial equilibrium position, on the time derivatives of x, and possibly also on the time t itself. The form of σ is governed by structural considerations. Note that when the displacements x are small, the boundary condition embodied in Eqs. 5 and 6 can to a good approximation be applied at the equilibrium, or undisturbed, location of the wall rather than at the actual, instantaneous deflected position.

We separate the varibles into three components by writing

$$\vec{v} = 0 + \vec{v}_1 (\vec{r}, t) + \vec{v}_2 (\vec{r}, t) \qquad (7)$$

$$p = p_o(\vec{r}) + p_1 (\vec{r}, t) + p_2 (\vec{r}, t) \qquad (8)$$

$$\rho = \rho_o + \rho_1 (\vec{r}, t) + \rho_2 (\vec{r}, t) \qquad (9)$$

where the subscript (o) refers to the values corresponding to the initial static conditions in the fluid, the subscript (1) refers to the hypothetical perturbation which would be caused if the imposed blowdown occurred in the system with rigid walls, and the subscript (2) refers to the remainder of the quantity, and represents the perturbation which can be attributed to the flexibility of the walls. The initial pressure distribution p_o is assumed to be hydrostatic,

$$p_o = \text{constant} - \rho_o g z \qquad (10)$$

By definition, the rigid-wall flow is the solution of Eqs. 1-3 with $\vec{v}_2$, p_2 and ρ_2 equal to zero. Thus,

$$(\rho_o + \rho_1)\ (\frac{\partial \vec{v}_1}{\partial t} + \vec{v}_1 \cdot \nabla \vec{v}_1) = -\nabla p_1 - \rho_1 g \nabla z \qquad (11)$$

$$\frac{\partial \rho_1}{\partial t} + \vec{v}_1 \cdot \nabla \rho_1 + (\rho_o + \rho_1)\ \nabla \cdot \vec{v}_1 = 0 \qquad (12)$$

$$p_1 = \rho_1 c_o^2 \qquad (13)$$

Where we used Eq. 10 to eliminate p_o , and assumed ρ_o to be constant. The boundary conditions for the rigid-wall solution are that

$$p_o + p_1 = p_i(t) \quad \text{at the i'th free surface} \qquad (14)$$

and that

$$(v_1)_1 \equiv 0 \quad \text{at solid walls} \qquad (15)$$

The equations for the perturbation (2) due to wall flexure is obtained by substituting Eqs. 7-10 into Eqs. 1 and 2, and subtracting Eqs. 11 and 12, respectively. One obtains the equation of motion

$$(\rho_o + \rho_1 + \rho_2)(\frac{\partial \vec{v}_2}{\partial t} + \vec{v}_2 \cdot \nabla \vec{v}_1 + \vec{v}_1 \cdot \nabla \vec{v}_2 + \vec{v}_2 \cdot \nabla \vec{v}_2) =$$

$$= -\nabla p_2 - \rho_2 g \nabla z - \rho_2 (\frac{\partial \vec{v}_1}{\partial t} + \vec{v}_1 \cdot \nabla \vec{v}_1) \qquad (16)$$

and the mass conservation equation

$$\frac{\partial \rho_2}{\partial t} + \vec{v}_1 \cdot \nabla \rho_2 + \vec{v}_2 \cdot \nabla \rho_1 + \vec{v}_2 \cdot \nabla \rho_2 + \rho_2 \nabla \cdot \vec{v}_1$$

$$+ (\rho_0 + \rho_1 + \rho_2) \nabla \cdot \vec{v}_2 = 0 \quad , \qquad (17)$$

and the pressure-density relation ,

$$p_2 = \rho_2 c_o^2 \qquad (18)$$

Assuming that the wall flexure does not actually affect the gas pressure at the free surfaces, we can write the free-surface boundary condition as

$$p_2 = 0 \quad \text{at the i'th free surface} \qquad (19)$$

The boundary condition at the rigid walls is

$$(v_\perp)_2 = \frac{dx}{dt} \qquad (20)$$

where x(t) is given by Eq. 6.

Eqs. 16 and 17 can be simplified considerably under conditions which are often not very restrictive in practice. Let

p_1 = typical amplitude of p_1

p_2 = typical amplitude of p_2

L = characteristic length over which gradients in velocity and pressure occur during the transient

τ_2 = characteristic time of the oscillation caused by wall flexure

x = typical wall displacement during wall flexure

We assume that

$$\frac{p_1}{\rho_0 c_0^2} \ll 1 \tag{21}$$

$$\frac{p_2}{\rho_0 c_0^2} \ll 1 \tag{22}$$

$$\frac{gL}{c_0^2} \ll 1 \tag{23}$$

$$\frac{\tau_2}{L}\sqrt{\frac{p_1}{\rho_0}} \ll 1 \tag{24}$$

$$\frac{x_2}{L} \ll 1 \tag{25}$$

$$\frac{x_2}{L} \ll \frac{p_2}{p_1} \tag{26}$$

The implication of these assumptions becomes apparent when we analyze the orders of magnitude of the various terms in Eqs. 11 and 12 and Eqs. 16 and 17. We note the orders of magnitude (denoted by the symbol ~)

$$v_1 \sim \sqrt{\frac{p_1}{c_o}} \tag{27}$$

$$\nabla \sim \frac{1}{L} \tag{28}$$

$$v_2 \sim \frac{x}{\tau_2} \tag{29}$$

$$\frac{\partial v_2}{\partial t} \sim \frac{x}{\tau_2^2} \tag{30}$$

$$\frac{\partial \rho_2}{\partial t} \sim \frac{\rho_2}{\tau_2} \tag{31}$$

and that ρ_1 and ρ_2 are given in terms of p_1 and p_2 by Eqs. 13 and 18, respectively.

Eqs. 21 and 22 imply that ρ_1 and ρ_2 are small compared with ρ_o. Eq. 21 furthermore implies that, in Eq. 11, the gravitational term on the right is negligible compared with the pressure gradient term and that in Eq. 12, the second term is small compared with the third. Hence, the equation for the rigid-wall flow reduce in good approximation to

$$\rho_o \left(\frac{\partial \vec{v}_1}{\partial t} + \vec{v}_1 \cdot \nabla \vec{v}_1\right) = -\nabla p, \tag{32}$$

$$\frac{\partial \rho_1}{\partial t} + \rho_o \nabla \cdot \vec{v}_1 = 0 \tag{33}$$

$$p_1 = \rho_1 c_o^2 \tag{34}$$

The boundary conditions are given by Eqs. 14 and 15. On the left-hand side of Eq. 16, the second and third velocity terms are negligible compared with the time-derivative term when Eq. 24 applies, and the fourth term is negligible when Eq. 25 applies. On the right-hand side of the same equation, the pressure-gradient term is large compared with the terms involving $\vec{v}_1$ when Eq. 21 applies, and also large compared with the gravitational term if Eq. 23 applies. Thus, the equations for the perturbation caused by wall flexure reduce to

$$\rho_o \frac{\partial \vec{v}_2}{\partial t} = -\nabla p_2 \tag{35}$$

$$\frac{\partial \rho}{\partial t_2} + \rho_o \nabla \cdot \vec{v}_2 = 0 \tag{36}$$

$$p_2 = c_o^2 \rho_2 \tag{37}$$

The boundary conditions for the wall flexure perturbation are Eqs. 19 and 20, with x(t) governed by Eq. 6,

$$m \frac{d^2x}{dt} = p_1 + p_2 - \sigma(x, \frac{dx}{dt}, \frac{d^2x}{dt^2}, \ldots, t) \tag{38}$$

The equations 35-37 for the perturbation flow field do not explicity involve the rigid-wall solution. The wall perturbation solution is coupled

to the rigid-wall flow field only through the pressure p_1 in the boundary condition at the wall, Eq. 38, and through the instantaneous locations and shapes of the free surfaces (governed by the rigid-wall solution), where the boundary condition Eq. 19 must be applied. It is as if the rigid-wall pressure $P_1(t)$ appears as an externally applied transient pressure on the wall, and drives the wall (and fluid) oscillation calculated by the perturbation (2). Thus, if one has obtained, analytically or experimentally, the rigid-wall pressure distribution history p_1 at the walls and the time-dependent shapes of the free surfaces, one can apply it as a boundary conditions on the solution 2 and calculate the perturbations in velocity and pressure, throughout the fluid, caused by wall flexibility.

Eqs. 35-37 are the linearized acoustic equations for the liquid, and can be solved for example by the usual linear method of characteristics with the sound speed c_o taken as a constant. The liquid is, as it were, regarded somewhat as a "gel" with its free surface boundaries prescribed as a function of time by the rigid-wall flow field. In the particular case where the period τ_2 of the wall oscillations is much longer than the acoustic transit time L/c_o across the system, that is,

$$\frac{L}{\tau_2 c_o} \ll 1, \tag{39}$$

Eqs. 35-37 reduce to the simple, linearized incompressible flow form

$$\rho_o \frac{\partial \vec{v}_2}{\partial t} = -\nabla p_2 \tag{40}$$

$$\nabla \cdot \vec{v}_2 = 0 \tag{41}$$

This constitutes a particularly simple case, since the pressure p_2 now satisfies Laplace's equation.

3. DISCUSSION OF APPLICATIONS

The analysis outlined here has an important application in the design of large vessels, such as the pressure-suppression containment systems of boiling-water reactors, where transient liquid flows are induced and wall flexibility effects must be accounted for. In many such cases the basic transient flow phenomena are very complex and can be quantified only by means of small-scale experimental simulation [4, 5]. Often it is impracticable to model both the effects of wall flexibility and the hydrodynamics on a small scale. The question then arises whether one can use the hydrodynamic data derived from small-scale tests with rigid walls, and derive from that the strains in the walls of a real, full-scale system where wall flexure may occur.

The present analysis gives a rigorous basis for such a procedure. Consider the situation in Fig. 1 as an example. Let us say we have available, from an experimental simulation with rigid walls, the pressure history $p_1(t)$ at every point on the walls and the locations of the free surfaces as a function of time. One can then obtain a numerical solution of the relatively simple, linear fluid equations, Eqs. 35-37 (or, if Eq. 39 applies, Eqs. 40-41) for the perturbations caused by wall flexiblity. The rigid-wall pressure $p_1(t)$ appears as a driving force in the wall boundary condition for the perturbation, Eqs. 20 and 38, and the specified free surface locations define where the free surface boundary condition, Eq. 19, is to be applied.

The method is valid as long as the inequalities expressed in Eqs. 21-26 apply. These inequalities can be shown to apply under a broad range of practical conditions.

REFERENCES

1. Belytschko, T., Nuclear Eng. and Des., 42, 41-52, 1977.

2. Blevins, R. D., Flow-Induced Vibration, Van Nostrand Reihold Co., New York, 1977.

3. Bedrosian, B., private communication, 1978.

4. Sonin, A. A., and Huber, P. W., J. Heat Transfer, 100, 601-604, 1978.

5. Anderson, W. G., Huber, P. W., and Sonin, A. A., J. Heat Transfer, 100, 605-612, 1978.

SYMBOLS

c	speed of sound in liquid
g	gravitational acceleration
L	characteristic length associated with gradients in velocity, density and pressure
m	wall mass per unit area
p	pressure
t	time
$\vec{v}$	velocity
v_1	component of velocity directed perpendicularly into wall
x	displacement of wall from equilibrium position, in perpendicular direction away from fluid
z	direction measured vertically upward, against gravity
ρ	liquid density
τ_2	characteristic time associated with the wall flexure (e.g. period of wall vibration).

Subscripts:

0	value corresponding to the initial conditions in the static fluid.
1	perturbation which would be caused if the event occurred in a rigid-wall system.
2	remainder of the quantity, i.e. additional perturbation caused by wall flexibility.

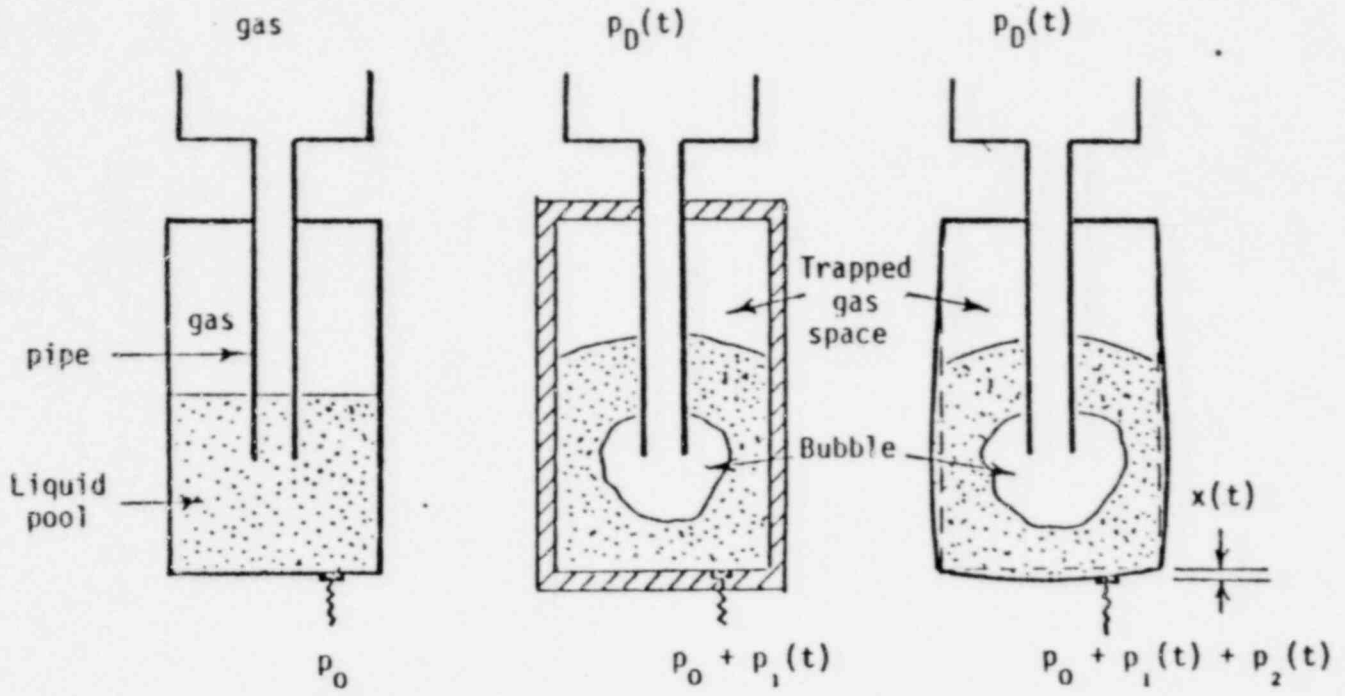

Figure 1: Example of flow transient. (a) Initial condition. (b) Time t in system with rigid walls. (c) Time t in system with flexible walls.

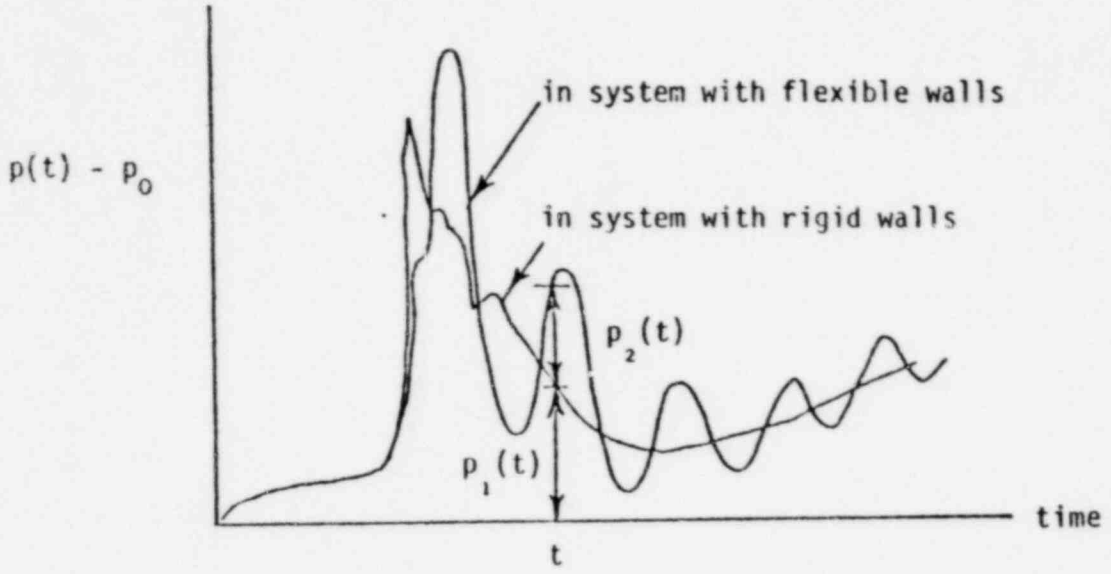

Figure 2: Sketch of pressure histories in rigid-wall and in flexible-wall systems.